



TECHNISCHE  
UNIVERSITÄT  
WIEN

Vienna University of Technology

DIPLOMARBEIT

# First-Principles Studies of Zirconia and its Interface to Platinum-Zirconium Alloys

Ausgeführt am  
Institut für Allgemeine Physik  
der Technischen Universität Wien

unter Anleitung von  
ao. Univ. Prof. Dr. Josef Redinger  
und  
Dr. Florian Mittendorfer

durch

Wernfried Mayr-Schmölzer  
Rudolfsplatz 4/27  
A-1010 Wien

25. Juli 2012

## Abstract

In this thesis a comprehensive study of the most important bulk phases of Zirconia ( $\text{ZrO}_2$ ) and its interface to a Platinum-Zirconium alloy is presented. The  $\text{ZrO}_2$  bulk is stable at ambient pressure and room temperature in a monoclinic  $P2_1/c$  structure, while at higher temperature the  $\text{ZrO}_2$  bulk shows phase transitions first into a tetragonal  $P4_2/nmc$  and then into a cubic  $Fm\bar{3}m$  structure. Furthermore orthorhombic phases ( $Pbca$  and  $Pnma$  structures) are stabilized by applying high pressures.

Using the *ab-initio* DFT code VASP the stability of each phase was calculated using both local and non-local functionals and compared to experimental data. The four different functionals used included the Local Density Approximation (LDA), the PBE and PBEsol functionals employing the General Gradient Approximation, and hybrid functionals where part of the exchange energy is taken from the Hartree-Fock approach (HSE). Equilibrium structural parameters were calculated, including lattice constants, volumes, cell shapes, bulk moduli and the internal positional parameters. It could be shown that the PBEsol functional gives the best agreement with the experiments concerning the structural parameters and transition pressures. The densities of states were also obtained using the different functionals, with the non-local hybrid functionals giving the best results with respect to the band gaps.

Experimental data have shown that the creation of thin Zirconia films is possible by oxidation of a suitable metal, for example  $\text{Pt}_3\text{Zr}$ . Again using the *ab-initio* VASP DFT code both the  $\text{Pt}_3\text{Zr}$  substrate and the interface between an ultra-thin film of  $\text{ZrO}_2$  were studied. The  $\text{Pt}_3\text{Zr}$  crystal has a hexagonal lattice similar to  $\text{Ni}_3\text{Ti}$  and is built up of stacks of mixed zirconium-platinum layers. These layers are arranged in the bulk in an ABAC stacking. Experiments have shown that steps in the surface of the  $\text{Pt}_3\text{Zr}$  substrate have a height of two atomic layers and that the surface is devoid of zirconium atoms due to oxidation. The present DFT calculations allowed to determine the correct surface termination to be of A type.

STM images of the  $\text{ZrO}_2$  film which is a O-Zr-O trilayer show a  $(\sqrt{19} \times \sqrt{19})R23^\circ$  cell with respect to the (111) surface plane of the  $\text{Pt}_3\text{Zr}$  substrate. To reduce the computation time two different models were used to study the  $\text{ZrO}_2$ - $\text{Pt}_3\text{Zr}$  interface. Results obtained with the PBE functional which shows only very weak bonding were compared to calculations using functionals including approximations to the non-local van der Waals contributions (vdW-DF). These results have confirmed that the van der Waals interaction needs to be accounted for to yield results in agreement with the experiment. By simulation of STM images the bright spots in the experimental STM images were attributed to the zirconium atoms.

## Zusammenfassung

In dieser Diplomarbeit wurden die wichtigsten Phasen von Zirkonoxid ( $\text{ZrO}_2$ ) und dessen Grenzfläche mit einem Platin-Zirkon Metall untersucht. Der  $\text{ZrO}_2$  Festkörper ist bei Raumtemperatur und Normaldruck in einer monoklinen  $P2_1/c$  Phase stabil, während es bei höheren Temperaturen zwei Phasenübergänge zu einer tetragonalen  $P4_2/nmc$  Phase und zu einer kubischen  $Fm\bar{3}m$  Phase gibt. Unter erhöhtem Druck sind orthorhombische Phasen ( $Pbca$  und  $Pnma$ ) stabil.

Die Stabilität dieser Phasen wurde mit dem Dichtefunktionalprogramm VASP sowohl mit lokalen als auch mit nichtlokalen Funktionalen untersucht. Vier verschiedene Funktionale wurden verwendet: die lokale Dichtenäherung (LDA), die PBE und PBEsol Funktionale, die beide eine Form der Gradientennäherung (GGA) verwenden, und ein Hybridfunktional (HSE) bei dem ein Teil der Austauschenergie mit der Hartree-Fock-Methode berechnet wird. Mit diesen Funktionalen wurden für die jeweiligen Strukturen die strukturellen Parameter im energetischen Minimum berechnet, das sind Gitterkonstanten, Zellformen und -volumen, Kompressionsmodul und die internen Positionsparameter der Atome. Das PBEsol Funktional zeigt im Vergleich mit dem Experiment die beste Übereinstimmung dieser Parameter und der Übergangsdrücke. Weiters wurden die elektronischen Zustandsdichten der Phasen mit den vier Funktionalen berechnet und mit experimentellen Daten verglichen. Für die Bandlücke ergibt das Hybridfunktional die beste Übereinstimmung.

Um dünne Zirkonoxid Schichten herzustellen kann eine geeignete Legierung oxidiert werden, zum Beispiel  $\text{Pt}_3\text{Zr}$ . Mit Hilfe von VASP wurde das  $\text{Pt}_3\text{Zr}$  Substrat und die Grenzfläche zwischen diesem und einer dünnen Zirkonoxid Schicht untersucht. Der  $\text{Pt}_3\text{Zr}$  Kristall besteht aus einem der  $\text{Ni}_3\text{Ti}$  Struktur ähnlichen hexagonalen Gitter und ist aus gemischten Schichten von Platin- und Zirkonatomen in ABAC-Reihenfolge aufgebaut. Die experimentell bestimmten Daten zeigen dass die Oberfläche des Substrates keine Zirkonatome mehr enthält, und dass Stufen in der Oberfläche des  $\text{Pt}_3\text{Zr}$  Substrates zwei Atomlagen hoch sind. Die hier präsentierten DFT Rechnungen konnten eindeutig zeigen dass die bevorzugte Oberflächenschicht vom Typ A ist.

STM Bilder der  $\text{ZrO}_2$  Schicht zeigen eine O–Zr–O Trilage in einer  $(\sqrt{19} \times \sqrt{19})R23^\circ$  Superzelle auf einer (111) orientierten Oberfläche des Substrates. Um die Rechenzeit zu verringern wurden zwei verschiedene Modelle für die  $\text{ZrO}_2$ – $\text{Pt}_3\text{Zr}$  Grenzfläche erstellt und mit dem Experiment verglichen. DFT Rechnungen die mit dem PBE Funktional durchgeführt wurden zeigten nur sehr schwache Bindung zum Substrat. Im Vergleich mit einem Funktional, bei dem Näherungen zur nichtlokalen van der Waals Wechselwirkung hinzugefügt wurden (vdW-DF), zeigen diese dass die van der Waals Beiträge für eine Übereinstimmung mit dem Experiment essentiell sind. Durch Simulation von STM Bildern konnten die hellen Punkte in den STM Bildern als Zirkonatome identifiziert werden.

# Contents

|   |           |
|---|-----------|
| <b>1. Introduction</b>  | <b>9</b>  |
| <b>2. Crystal Phases and Phase Transitions</b>                  | <b>10</b> |
| 2.1. Definition of a Phase . . . . .                            | 10        |
| 2.1.1. Critical exponents . . . . .                             | 11        |
| 2.2. Models . . . . .   | 11        |
| 2.3. Mean-field theories . . . . .                              | 13        |
| 2.3.1. Mean-Field Critical Exponents . . . . .                  | 14        |
| 2.4. Equations of State . . . . .                               | 15        |
| <b>3. Computational Methods</b>                                 | <b>16</b> |
| 3.1. Density Functional Theory . . . . .                        | 16        |
| 3.2. Local Density Approximation (LDA) . . . . .                | 18        |
| 3.3. Generalized Gradient Approximation (GGA) . . . . .         | 18        |
| 3.4. Non-local Contributions . . . . .                          | 19        |
| 3.4.1. Hybrid Functionals . . . . .                             | 19        |
| 3.4.2. Van der Waals-DFT . . . . .                              | 20        |
| 3.5. Vienna Ab-initio Simulation Package (VASP) . . . . .       | 20        |
| <b>4. The <math>\text{ZrO}_2</math> Bulk</b>                    | <b>22</b> |
| 4.1. $\text{ZrO}_2$ Bulk Phases . . . . .                       | 22        |
| 4.1.1. Monoclinic Phase . . . . .                               | 22        |
| 4.1.2. Tetragonal Phase . . . . .                               | 22        |
| 4.1.3. Cubic Phase . . . . .                                    | 24        |
| 4.1.4. Orthorhombic Phases . . . . .                            | 24        |
| 4.2. Calculations . . . . .                                     | 25        |
| 4.3. Results . . . . .  | 27        |
| 4.3.1. Equation of State . . . . .                              | 27        |
| 4.3.2. Lattice Parameters . . . . .                             | 28        |
| 4.3.3. Bulk Moduli and Transition Pressures . . . . .           | 36        |
| 4.3.4. Electronic structures . . . . .                          | 37        |
| 4.4. Conclusion . . . . .                                       | 39        |
| <b>5. The <math>\text{Pt}_3\text{Zr-ZrO}_2</math> Interface</b> | <b>40</b> |
| 5.1. Introduction . . . . .                                     | 40        |
| 5.2. Experiment . . . . .                                       | 40        |



|   |           |
|---|-----------|
| 5.3. The Pt <sub>3</sub> Zr Substrate . . . . .               | 40        |
| 5.3.1. Bulk Structure . . . . .                               | 40        |
| 5.3.2. Surface Termination . . . . .                          | 42        |
| 5.4. The ZrO <sub>2</sub> film . . . . .                      | 45        |
| 5.5. Pt <sub>3</sub> Zr-ZrO <sub>2</sub> -Interface . . . . . | 48        |
| 5.5.1. The Model . . . . .                                    | 48        |
| 5.5.2. Calculations . . . . .                                 | 51        |
| 5.6. Conclusion . . . . .                                     | 63        |
| 5.7. Outlook . . . . .  | 63        |
| <b>6. Acknowledgements</b>                                    | <b>64</b> |
| <b>A. The INCAR File</b>                                      | <b>65</b> |
| <b>B. CONTCARS</b>  | <b>67</b> |
| B.1. Pt <sub>3</sub> Zr-ZrO <sub>2</sub> -Interface . . . . . | 67        |
| <b>C. Additional Tables</b>                                   | <b>71</b> |
| <b>D. Bibliography</b>  | <b>77</b> |

# List of Figures

|  |    |
|--|----|
| 4.1. Monoclinic $\text{ZrO}_2$   | 23 |
| 4.2. Tetragonal $\text{ZrO}_2$   | 23 |
| 4.3. Cubic $\text{ZrO}_2$  | 24 |
| 4.4. Orthorhombic $Pbca$ (Ortho-I)   | 25 |
| 4.5. Orthorhombic $Pbca$ (Ortho-I)   | 26 |
| 4.6. Energy versus volume, LDA and PBE   | 29 |
| 4.7. Energy versus volume, PBEsol and HSE  | 30 |
| 4.8. $\text{ZrO}_2$ densities of states  | 38 |
| 5.1. $\text{Pt}_3\text{Zr}$ crystal structure  | 41 |
| 5.2. 3-layered $\text{Pt}_3\text{Zr}$ slabs  | 43 |
| 5.3. 5-layered $\text{Pt}_3\text{Zr}$ slabs  | 44 |
| 5.4. 5-layered Pt terminated $\text{Pt}_3\text{Zr}$ slabs                                      | 46 |
| 5.5. $\text{ZrO}_2$ trilayer   | 47 |
| 5.6. Total energies, $\text{ZrO}_2$ trilayer   | 48 |
| 5.7. Modeling the $\text{ZrO}_2$ film  | 49 |
| 5.8. $\text{Pt}_3\text{Zr}$ - $\text{ZrO}_2$ -interface models                                 | 50 |
| 5.9. Distance of the terminating Pt layer to the lower oxygen layer of the $\text{ZrO}_2$ film | 52 |
| 5.10. Fully relaxed $\text{Pt}_3\text{Zr}$ - $\text{ZrO}_2$ structure, PBE                     | 55 |
| 5.11. Fully relaxed $\text{Pt}_3\text{Zr}$ - $\text{ZrO}_2$ structure, vdW-DF                  | 56 |
| 5.12. $\text{Pt}_3\text{Zr}$ - $\text{ZrO}_2$ interface, charge distribution                   | 58 |
| 5.13. $\text{Pt}_3\text{Zr}$ - $\text{ZrO}_2$ interface, densities of states                   | 60 |
| 5.14. $\text{Pt}_3\text{Zr}$ - $\text{ZrO}_2$ interface, STM simulation                        | 61 |
| 5.15. $\text{Pt}_3\text{Zr}$ - $\text{ZrO}_2$ interface, STM simulation, cropped PDOS          | 62 |

# List of Tables

|  |    |
|--|----|
| 4.1. $K$ -point meshes used for the $\text{ZrO}_2$ bulk calculations using local functionals.                                    | 27 |
| 4.2. $K$ -point meshes used for the $\text{ZrO}_2$ bulk calculations using the HSE functional. . . . .                           | 27 |
| 4.3. Energy difference per formula unit at the equilibrium volume compared to the monoclinic phase. . . . .                      | 28 |
| 4.4. Monoclinic $P2_1/c$ lattice parameters. . . . .   | 31 |
| 4.5. Monoclinic $P2_1/c$ internal parameters. . . . .  | 32 |
| 4.6. Tetragonal $P4_2/nmc$ lattice parameters. . . . .   | 33 |
| 4.7. Cubic $Fm\bar{3}m$ lattice parameters. . . . .  | 33 |
| 4.8. Orthorhombic $Pbca$ (Ortho-I) lattice parameters. . . . .   | 34 |
| 4.9. Orthorhombic $Pbca$ (Ortho-I) internal parameters. . . . .  | 34 |
| 4.10. Orthorhombic $Pnma$ (Ortho-II) lattice parameters. . . . .   | 35 |
| 4.11. Orthorhombic $Pnma$ (Ortho-II) internal parameters. . . . .  | 35 |
| 4.12. Calculated bulk moduli for all functionals and structures. . . . .   | 36 |
| 4.13. Transition pressures . . . . .   | 37 |
| 4.14. Calculated and measured band gaps. . . . .   | 37 |
| 5.1. Lattice parameters and equilibrium volume for bulk $\text{Pt}_3\text{Zr}$ . . . . .   | 42 |
| 5.2. Calculated total and surface energies for the $\text{Pt}_3\text{Zr}$ slab configurations. . .                               | 44 |
| 5.3. Calculated total energies of the Pt-terminated $\text{Pt}_3\text{Zr}$ slab configurations. .                                | 45 |
| 5.4. Distances of the terminating platinum layer of the substrate to the lower oxygen layer of the $\text{ZrO}_2$ film . . . . . | 51 |
| 5.5. Initial substrate- $\text{ZrO}_2$ film distances . . . . .  | 52 |
| 5.6. Interlayer distances, buckling and adsorption energies . . . . .  | 54 |
| 5.7. Work function $\Phi$ . . . . .  | 57 |
| C.1. Calculated energies, LDA. . . . .   | 71 |
| C.2. Calculated energies, PBE. . . . .   | 72 |
| C.3. Calculated energies, PBEsol. . . . .  | 73 |
| C.4. Calculated energies, HSE. . . . .   | 74 |
| C.5. Parameters of the Birch-Murnaghan equations, LDA. . . . .   | 74 |
| C.6. Parameters of the Birch-Murnaghan equations, PBE. . . . .   | 75 |
| C.7. Parameters of the Birch-Murnaghan equations, PBEsol. . . . .  | 75 |
| C.8. Parameters of the Birch-Murnaghan equations, HSE. . . . .   | 75 |
| C.9. PAW potentials bundled with VASP used for all calculations. . . . .   | 76 |

# Listings

|  |    |
|--|----|
| A.1. Sample INCAR file. . . . .          | 66 |
| B.1. Zr/Pt PBE . . . . .                 | 67 |
| B.2. O <sub>1</sub> /Pt PBE . . . . .    | 68 |
| B.3. Zr/Pt vdW-DF . . . . .              | 69 |
| B.4. O <sub>1</sub> /Pt vdW-DF . . . . . | 69 |

# 1. Introduction

Zirconia ( $\text{ZrO}_2$ ) is an interesting material with various applications, both in pure and in doped forms. It is one of the most corrosion-resistant and refractive materials known, and its applications range from the use as thermal barrier coating in engines, to artificial diamonds, oxygen sensors and fuel cell membranes due to its ability to allow free movement of oxygen ions through the crystal structure. It also has a large band gap of 5 eV to 7 eV depending on the studied phase and is therefore a good isolator.

At room temperature  $\text{ZrO}_2$  is stable in a monoclinic  $P2_1/c$  phase, while at higher temperatures it shows phase transitions first to a tetragonal  $P4_2/nmc$  phase at about 1440 K and then to a cubic  $Fm\bar{3}m$  phase at about 2650 K. Under high pressure  $\text{ZrO}_2$  exists in different orthorhombic phases, first transitioning to an orthorhombic  $Pbca$  phase at 8 GPa to 11 GPa and later to an orthorhombic  $Pnma$  phase at 21 GPa to 27 GPa. Stabilization of the cubic phase can be achieved by doping the  $\text{ZrO}_2$  crystal with Yttrium or by creating thin  $\text{ZrO}_2$  films on a suitable metal.

The direct application of electron based analysis methods like scanning tunneling microscopy (STM) to zirconia is difficult due to the large band gap. It is therefore useful to examine ultra thin zirconia films which have been deposited on a suitable substrate. One example of this technique is deposition and oxidation of zirconia on a  $\text{Pt}_3\text{Zr}(111)$  substrate. The research presented in this thesis covers ultra thin  $\text{ZrO}_2$  films grown on a  $\text{Pt}(111)$  substrate, resulting in  $\text{ZrO}_2$  films which are (111)-oriented with respect to the cubic fluorite  $\text{ZrO}_2$  bulk structure[1–3].

As the interest in solid oxide fuel cells has recently risen, using density functional theory is a promising method to understand the structural and electronic properties of the  $\text{ZrO}_2$  bulk phases and its interface to various metals.

In chapter 2 a short introduction to the physics of phases and phase transformations is given, followed by an introduction to density functional theory in chapter 3 where its advantages and caveats are explained. Then, in chapter 4, a comprehensive *ab-initio* study of the most important phases of Zirconia is presented, covering both high temperature and high pressure phases. Both the structural and electronic parameters of the various phases were studied. This is followed by an investigation of the interface of a platinum terminated  $\text{Pt}_3\text{Zr}$  substrate and a  $\text{ZrO}_2$  monolayer in chapter 5 where the different tools offered by density functional theory were used to complement experimental measurements[4].

## 2. Crystal Phases and Phase Transitions

### 2.1. Definition of a Phase

A phase is defined as a region of space with uniform physical properties. These properties can be the density, magnetization or chemical composition of a material, but also the structural order of a crystal. A transformation between different phases is called a phase transition. During this transition one of the aforementioned properties changes as a result of an external condition. Especially, transitions between different crystal phases can occur when a crystal is heated or put under pressure.

A phase transition is marked by a singularity in a thermodynamic potential. One has to differentiate between phase transitions of first and second order. In the first-order phase transitions a discontinuous transition occurs, meaning that one or more of the first derivatives of the appropriate thermodynamic potential has a finite discontinuity. If the first derivatives are continuous but second order derivatives discontinuous, the phase transition is called continuous or critical.

For the description of a crystal phase one appropriate potential is the Enthalpy  $H$ . It includes the internal energy required to create a system and the energy required to establish its volume and pressure according to

$$H = U + pV \quad (2.1)$$

with  $U$  being the internal energy,  $p$  the pressure and  $V$  the volume of the crystal.

Another important thermodynamic potential is the Gibbs free energy  $G$ , given by

$$G = U + pV - ST \quad (2.2)$$

with  $S$  being the entropy and  $T$  the temperature. As DFT calculations essentially occur at  $T = 0$  the Gibbs free energy is equal to the Enthalpy.

#### Diffusionless Transformations

One important type of phase transition is a diffusionless phase transition. It is a phase change where cooperative, homogenous movement of atoms results in a change of the crystal structure. The crystal lattice can be distorted by dilation or shearing while keeping the relative positions of the atoms more or less in place, transforming one Bravais lattice into another. A special case of first-order diffusionless transformations is the Martensitic transformation where the strain energy plays a significant role. Here the product phase inherits the same atomic order and composition as the parent phase. Originally found by quenching the steel structure Austenite to the eponymous Martensite

phase transformations of this kind have been observed in various metal transformations such as the cubic to tetragonal transition of Zirconia studied in section 4.1.2.

### 2.1.1. Critical exponents

A critical point is marked by a divergence in an extensive property of a thermodynamic system. Critical exponents help to understand the form of these divergences and the singular behavior of other thermodynamic functions near the critical point by describing them in terms of a power law around the critical temperature  $T_c$ .

A measure of the deviation in temperature from the critical temperature  $T_c$  is the reduced temperature

$$t = (T - T_c)/T_c. \quad (2.3)$$

The critical exponent associated with a function  $F(t)$  is, assuming that the limit  $t \rightarrow 0$  exists, defined as

$$\lambda = \lim_{t \rightarrow 0} \frac{\ln |F(t)|}{\ln |t|}. \quad (2.4)$$

Equation (2.4) can also be written as

$$F(t) \sim |t|^\lambda \quad (2.5)$$

with  $\sim$  signifying that this equation only describes the asymptotic behavior in the limit  $t \rightarrow 0$ . Comparing eq. (2.5) to the leading behavior of the singularities in the thermodynamic function one arrives at various critical exponents for different systems. Some of the most commonly used critical exponents for example for a fluid system include the correlation length  $\xi \sim |t|^{-\nu}$  or the isothermal compressibility  $\kappa_T \sim |t|^{-\gamma}$ . Critical exponents are to a large degree universal depending on only a few fundamental parameters, while the critical temperature  $T_c$  is very sensitive to details of the interatomic interactions.

## 2.2. Models

To describe a physical system it is useful to build mathematical models which describe the cooperative behavior. While it is possible to create a very realistic model which includes all many-body interactions, solving the corresponding Schrödinger equation numerically often cannot be done in a sensible timeframe. Another approach is therefore to build the simplest possible model which includes all essential physics and hope it is still accurate enough to give a good approximation of the numerical solution. In the following section a short introduction to some statistical mechanical model will be given. For more information a standard textbook on statistical mechanics like *Thermodynamik - Von der Mikrophysik zur Makrophysik* by Stierstadt [5] or *Statistical Mechanics of Phase Transitions* by Yeomans [6] should be consulted.

### Spin-1/2 Ising model

One very successful model for an interacting system is the spin-1/2 Ising model. It describes the interaction of classical spin variables  $s_i$  which can take the values  $\pm 1$  and are placed at the lattice sites of the system. These spins interact pairwise according to a Hamiltonian

$$\mathcal{H} = -J \sum_{\langle ij \rangle} s_i s_j - H \sum_i s_i. \quad (2.6)$$

The first term in eq. (2.6) describes the interaction between the spins  $s_i$  and the possibility of a phase transition.  $J$  corresponds to the exchange energy, and  $\langle ij \rangle$  stands for a sum over the nearest-neighbor spins. The Hamiltonian can of course be expanded by adding terms describing interactions between further-neighbor spins.

An example for a system which can be described with the spin-1/2 Ising model is beta brass, a binary alloy. Beta brass consists of copper and zinc atoms which form a body-centered lattice. At high temperature the lattice sites are occupied at random by either copper or zinc. At a temperature below  $T_c = 733 \text{ K}$  a phase transition occurs to an ordered state where each species prefers to occupy one of the two sub-lattices of the bcc lattice.

As each site can be occupied by either copper or zinc the system can be described by a spin-1/2 Ising model. A value of the spin-variable  $s_i = 1$  corresponds to an occupation of position  $i$  by copper, and  $s_i = -1$  by an occupation of position  $i$  by zinc. With  $J_{CuCu}$ ,  $J_{ZnZn}$  and  $J_{CuZn}$  describing the interaction between two copper atoms, two zinc atoms and a copper and a zinc atom respectively the Hamiltonian can be written as

$$\begin{aligned} \mathcal{H} = & \frac{1}{4} \sum_{\langle ij \rangle} J_{CuCu} (1 + s_i)(1 + s_j) + \frac{1}{4} \sum_{\langle ij \rangle} J_{ZnZn} (1 - s_i)(1 - s_j) + \\ & + \frac{1}{4} \sum_{\langle ij \rangle} J_{CuZn} \{ (1 + s_i)(1 - s_j) + (1 - s_i)(1 + s_j) \}. \end{aligned} \quad (2.7)$$

Equation (2.7) can also be written as

$$\mathcal{H} = -J \sum_{\langle ij \rangle} s_i s_j - H \sum_i s_i + C \quad (2.8)$$

with  $J = \frac{1}{4}(J_{CuCu} + J_{ZnZn} - 2J_{CuZn})$  and  $C$  being a spin-independent variable.

Because each lattice site is always occupied by either a copper or a zinc atom and no impurities or vacancies are presumed to exist the use of an Ising variable is not an approximation. Nevertheless, to reproduce the thermodynamic functions of this system correctly more variables have to be taken into account, like long-range interactions and multi-spin terms (interaction between more than two spins, e.g.  $s_i s_j s_k$ ).



### Spin-1 Ising Model

For the description of systems with more than two states the spin-1/2 Ising model needs to be expanded, leading to the general Hamiltonian

$$\begin{aligned}\mathcal{H} = & -J \sum_{\langle ij \rangle} s_i s_j - K \sum_{\langle ij \rangle} s_i^2 s_j^2 - D \sum_i s_i^2 \\ & - L \sum_{\langle ij \rangle} (s_i^2 s_j + s_i s_j^2) - H \sum_i s_i, \quad s_i = \pm 1, 0.\end{aligned}\quad (2.9)$$

In this model all possible terms  $s_i^\alpha s_j^\beta$  with  $\alpha, \beta = 0, 1, 2$  are allowed, and higher powers of the spins do not have to be taken into account because  $s_i^3 = s_i$ . It can describe a much higher variety of critical behavior due to its enlarged parameter space than the spin-1/2 Ising model.

### 2.3. Mean-field theories

As it is very hard to solve the spin-1/2 Ising system in three dimensions various approximation techniques were introduced. One of the most widely used is the mean-field theory. Here the n-body system is replaced by a 1-body system interacting with a chosen external field which replaces the interactions between an arbitrary particle and all other particles. This field is also called *molecular field*. The problem is though that it ignores spin fluctuations and can therefore only be valid when those fluctuations can be disregarded.

To derive the mean-field theory one starts with the Bogolyubov inequality

$$\mathcal{F} \leq \Phi = \mathcal{F}_0 + \langle \mathcal{H} - \mathcal{H}_0 \rangle_0 \quad (2.10)$$

where  $\mathcal{H}_0$  is a trial Hamiltonian with the parameter  $H_0$ ,  $\mathcal{F}_0$  the corresponding free energy,  $\mathcal{F}$  the true free energy of the system and the brackets stand for the average taken in the ensemble defined in  $\mathcal{H}_0$ . Minimizing  $\Phi$  with respect to  $H_0$  leads to the mean-field free energy

$$\mathcal{F}_{mf} = \min_{H_0} \{\Phi\}. \quad (2.11)$$

The inequality in eq. (2.10) ensures that the mean-field free energy cannot fall below the true free energy, so eq. (2.11) gives the best possible approximation.

An example for the use of the mean-field theory is the nearest neighbor Ising model in zero field. It is defined by the Hamiltonian in eq. (2.6) with  $H = 0$  on a lattice with  $z$  nearest neighbors for each site. For a simple cubic lattice  $z = 6$ .

The trial Hamiltonian is therefore

$$\mathcal{H}_0 = -H_0 \sum_i s_i \quad (2.12)$$

which is the Hamiltonian of a paramagnet. The free energy  $\mathcal{F}_0$  corresponding to the trial Hamiltonian is now

$$\mathcal{F}_0 = -NkT \ln(2 \cosh \beta H_0) \quad (2.13)$$

and the mean value of the spins

$$\langle s \rangle_0 = \tanh \beta H_0. \quad (2.14)$$

As  $\mathcal{H}_0$  only contains single-site terms one can write

$$\begin{aligned} \langle \mathcal{H} - \mathcal{H}_0 \rangle_0 &= \frac{\sum_{\{s\}} (-J \sum_{\langle ij \rangle} s_i s_j + H_0 \sum_i s_i) \exp[\beta H_0 \sum_i s_i]}{\sum_{\{s\}} \exp[\beta H_0 \sum_i s_i]} \\ &= -J \sum_{\langle ij \rangle} \langle s_i \rangle_0 \langle s_j \rangle_0 + H_0 \sum_i \langle s_i \rangle_0 \end{aligned} \quad (2.15)$$

For a translationally invariant system  $\langle s_i \rangle_0 = \langle s_j \rangle_0 \equiv \langle s \rangle_0$  and eq. (2.15) can now be written as

$$\langle \mathcal{H} - \mathcal{H}_0 \rangle_0 = -JzN \langle s \rangle_0^2 / 2 + NH_0 \langle s \rangle_0. \quad (2.16)$$

with  $zN/2$  being the number of bonds in the lattice. Finally, using eqs. (2.10), (2.13), (2.14) and (2.16) one arrives at

$$\Phi = -NkT \ln(2 \cosh \beta H_0) - \frac{JzN}{2} \tanh^2 \beta H_0 + NH_0 \tanh \beta H_0. \quad (2.17)$$

A minimization of this expression leads to a self-consistent formula for the mean field

$$\mathcal{H}_0 = Jz \tanh \beta H_0. \quad (2.18)$$

The mean-field free energy is now

$$\mathcal{F}_{mf} = -NkT \ln(2 \cosh \beta Jz \langle s \rangle_0) + NJz \langle s \rangle_0^2 / 2 \quad (2.19)$$

as can be seen by substituting eq. (2.18) into eq. (2.17).

### 2.3.1. Mean-Field Critical Exponents

Similar to section 2.1.1 critical exponents can be calculated for the mean-field Ising model. For example to obtain the exponent  $\alpha$  which describes the temperature dependence of the specific heat one differentiates the free energy twice. This leads to

$$C = \frac{3}{2}Nk + O(t) \quad T < T_c \quad (2.20)$$

$$C = 0 \quad T > T_c \quad (2.21)$$

and a discontinuity in the specific heat so that  $\alpha_{mf} = 0$ .

## 2.4. Equations of State

An equation of state describes the state of a matter under certain physical conditions. It formulates the mathematical correlation of multiple state functions of a material, for example its temperature, pressure, volume or internal energy. Historically these equations are used to describe the correlation of the temperature and pressure of a liquid to the density of its gas with the ideal gas law  $pV = R(T_C + 273.15)$  being one of the oldest, but also solid crystals can be modeled by such an equation of state. Murnaghan [7] derived formulae to calculate the stress in an elastic medium for a known strain and a known elastic energy density. While Hooke's law in its general form can predict the virtual work of all forces acting upon the medium in the infinitesimal theory this does not hold for finite matter. There the virtual work must be obtained by integrating over the scalar product of the stress tensor by the space-derivative of the virtual displacement vector. Murnaghan derived a formula for an isotropic elastic solid under hydrostatic pressure which describes its pressure using only two elastic constants  $\lambda$  and  $\mu$ :

$$p(V) = a(f(V) + 5f(V)^2), \quad f(V) = \frac{1}{2} \left\{ \left( \frac{V_0}{V} \right)^{\frac{2}{3}} - 1 \right\}, \quad a = 3\lambda + 2\mu. \quad (2.22)$$

Francis Birch [8] further developed this theory for a cubic symmetric medium under both hydrostatic compression of any amount, and a homogenous infinitesimal strain of general type. This led to the more elaborate formula for the pressure as a function of the volume shown in eq. (2.23) with the equilibrium volume  $V_0$ , the bulk modulus  $B_0$  and the pressure derivative of the bulk modulus  $B'_0$  being the state variables of the solid. It should be noted that experimentally  $B'_0$  is found to change little with pressure and is considered constant in these equations.

$$p(V) = \frac{3B_0}{2} \left[ \left( \frac{V_0}{V} \right)^{\frac{7}{3}} - \left( \frac{V_0}{V} \right)^{\frac{5}{3}} \right] \left\{ 1 + \frac{3}{4} (B'_0 - 4) \left[ \left( \frac{V_0}{V} \right)^{\frac{2}{3}} - 1 \right] \right\} \quad (2.23)$$

Integrating eq. (2.23) for the pressure according to the thermodynamic equation  $p = -(\partial E / \partial V)_S$  gives an equation for the energy:

$$E(V) = E_0 + \frac{9V_0B_0}{16} \left\{ \left[ \left( \frac{V_0}{V} \right)^{\frac{2}{3}} - 1 \right]^3 B'_0 + \left[ \left( \frac{V_0}{V} \right)^{\frac{2}{3}} - 1 \right]^2 \left[ 6 - 4 \left( \frac{V_0}{V} \right)^{\frac{2}{3}} \right] \right\}. \quad (2.24)$$

Using this formula for the total energy of a crystal system the enthalpy can be calculated according to eq. (2.25):

$$H = E + pV. \quad (2.25)$$

A point in a H over p diagram where the enthalpy for two phases is equal corresponds to the transition pressure between the two phases. This transition pressure can also be determined by using a common tangent construction in the plots of the total energy  $E(V)$  as shown in section 4.3.3.

## 3. Computational Methods

### 3.1. Density Functional Theory

The description of the structure and dynamics of many-electron systems is one of the fundamental problems in chemistry and theoretical physics. One important property of such systems is the structure of the electronic shell or, in the case of crystals, the electronic band structure. The stability of a system is directly determined by the electronic structure, and it is also an important parameter for electric and magnetic moments or in transport properties like the electrical conductivity.

Two different approaches can be used to study these properties:

1. Here the fundamental, true Hamiltonian of the system serves as the foundation of the approach, also called *first principles* or *ab-initio* approach. To facilitate this approach many technical approximations have to be used to solve the resulting many-body Schrödinger equation, an example being the representation of its single-particle ingredients in terms of a finite basis set. As with all approximations, important features can be missed depending on the system or the studied property when no due diligence is performed with regard to the approximations. The major advantage of the *ab-initio* approach is that no additional adjustable physical parameters are introduced.
2. For the second approach a suitable model Hamiltonian is introduced. Available data, often from experiments, is used to derive the model Hamiltonian. The advantage compared to the first approach is that the resulting many-body problem is much simpler than the *ab-initio* problem, but on the other hand important features may be ignored during the construction of the model.

The density functional theory approach used in this work uses the *ab-initio* approach introduced by Hohenberg and Kohn [9]. The Hohenberg-Kohn (HK) theorem represents a basic theorem which ensures that stationary many-body systems can be fully characterized by the ground state charge density. Knowledge of the ground state is therefore sufficient to determine all ground state observables, and the ground state energy functional  $E[n]$  can be used to determine the ground state density using a variational equation. As the exact form of the energy functional is not given by the HK-theorem, the Kohn-Sham (KS) scheme [10] was introduced to map an interactive N-particle problem to a suitable noninteracting system.

The energy functional can now be written as a functional of the electron density  $n(\mathbf{r})$ ,

$$E[n(\mathbf{r})] = T[n(\mathbf{r})] + V_{ee}[n(\mathbf{r})] + V_{ext}[n(\mathbf{r})], \quad (3.1)$$

with

$$V_{ext}[n(\mathbf{r})] = \int d\mathbf{r} n(\mathbf{r}) V_{ext}(\mathbf{r}). \quad (3.2)$$

The functional  $T[n(\mathbf{r})]$  corresponds to the kinetic energy of the electrons,  $V_{ee}[n(\mathbf{r})]$  represents the Coulomb interaction between the  $N$  electrons of the system, while  $V_{ext}[n(\mathbf{r})]$  represents the interaction between the electrons and the nuclei.

Equation (3.1) can now be written in terms of  $T_s[n(\mathbf{r})]$  which represents the kinetic energy of a virtual system of non-interacting electrons yielding the same density as the original interacting one, and in terms of the Hartree energy  $U[n(\mathbf{r})]$  which represents the electronic interaction of one electron with all other electrons:

$$U[n(\mathbf{r})] = \frac{1}{2} \int d\mathbf{r} \int d\mathbf{r}' \frac{n(\mathbf{r})n(\mathbf{r}')}{|\mathbf{r} - \mathbf{r}'|} \quad (3.3)$$

$$T_s[n(\mathbf{r})] = -\frac{1}{2} \sum_{i=1}^N \int d\mathbf{r} \phi_i^*(\mathbf{r}) \nabla^2 \phi_i(\mathbf{r}) \quad (3.4)$$

Also, another term is introduced, the exchange-correlation energy  $E_{xc}[n(\mathbf{r})]$ . It accounts for both the deviation of the Hartree energy from  $V_{ee}[n(\mathbf{r})]$  and of  $T_s[n(\mathbf{r})]$  from the real kinetic energy  $T[n(\mathbf{r})]$ :

$$E_{xc}[n(\mathbf{r})] = (T[n(\mathbf{r})] - T_s[n(\mathbf{r})]) + (V_{ee}[n(\mathbf{r})] - U[n(\mathbf{r})]), \quad (3.5)$$

leading to

$$E[n(\mathbf{r})] = T_s[n(\mathbf{r})] + U[n(\mathbf{r})] + V_{ext}[n(\mathbf{r})] + E_{xc}[n(\mathbf{r})]. \quad (3.6)$$

Equation (3.6) can now be minimized with respect to the electron density  $n(\mathbf{r})$  according to

$$0 = \frac{\delta T_s}{\delta \phi_i^*} + \frac{\delta}{\delta n(\mathbf{r})} \left\{ U[n(\mathbf{r})] + V_{ext}[n(\mathbf{r})] + E_{xc}[n(\mathbf{r})] \right\} \frac{\delta n(\mathbf{r})}{\delta \phi_i^*} \quad (3.7)$$

with  $\phi_i$  being one-electron wave functions. This finally leads to the Kohn-Sham equations[10]

$$\left\{ -\frac{1}{2} \nabla_i^2 + V_{eff}(\mathbf{r}) \right\} \phi_i(\mathbf{r}) = \epsilon_i \phi_i(\mathbf{r}) \quad (3.8)$$

with  $i = 1, \dots, N$  and

$$n(\mathbf{r}) = \sum_{i=1}^N |\phi_i(\mathbf{r})|^2, \quad (3.9)$$

$$V_{eff}(\mathbf{r}) = V_{ext}(\mathbf{r}) + \int \frac{n(\mathbf{r}')}{|\mathbf{r} - \mathbf{r}'|} d\mathbf{r}' + \frac{\delta E_{xc}(\mathbf{r})}{\delta n(\mathbf{r})}. \quad (3.10)$$

As can be seen in eq. (3.8) the problem is now reduced to  $N$  coupled Schrödinger equations of non-interacting particles. These equations can now be solved iteratively, starting from an initial guess  $n^0(\mathbf{r})$  for the charge density. After inserting  $n^0(\mathbf{r})$  into

$V_{eff}(\mathbf{r})$  the Kohn-Sham equations (eq. (3.8)) are solved and the resulting charge density is compared to the initial values. If the difference between the two charge densities is greater than a predefined threshold the calculated charge density is again inserted into eq. (3.8) and new results are calculated. A more comprehensive derivation of the Kohn-Sham equations can be found in *Density Functional Theory - An Advanced Course* by Dreizler and Engel [11].

Until now the exact form  $E_{xc}$  term is still unknown and needs to be determined by one of the various approximations described in the following sections.

## 3.2. Local Density Approximation (LDA)

In the LDA approach to approximate the exchange correlation energy term only local contributions of the electron density are accounted for, leading to the following functional for the exchange energy:

$$E_{xc}^{LDA}[n(\mathbf{r})] = \int d\mathbf{r} \epsilon_{xc}(n(\mathbf{r}))n(\mathbf{r}). \quad (3.11)$$

The term  $\epsilon_{xc}(n(\mathbf{r}))$  represents the exchange-correlation energy density for a homogenous electron gas. Advanced many-body techniques like quantum Monte-Carlo simulations can then be used to produce accurate results for the correlation energy density[12], and the resulting functional for the exchange correlation energy can then be used to solve eq. (3.8) iteratively.

As the coefficients used to describe the exchange energy density  $\epsilon_{xc}(n(\mathbf{r}))$  are completely determined by the properties of the homogenous electron gas the LDA is fully consistent with the *ab-initio* concept of the density functional theory. One deficiency of the LDA is that it predicts atomic negative ions to be unbound which results from the exponential decay of the LDA exchange potential. When used to investigate the lattice parameters of crystals it tends to over-bind and therefore leads to underestimated lattice constants. Nevertheless the LDA has been used for decades with surprisingly good results for numerous inhomogeneous systems.

## 3.3. Generalized Gradient Approximation (GGA)

To improve the results from the LDA many modifications of the energy correlation functional were introduced. An important expansion of the LDA regime is the generalized gradient approximation (GGA) which includes the gradient of the energy density in the exchange energy density function. This leads to a functional for the exchange energy

$$E_{xc}^{GGA}[n_{\uparrow}, n_{\downarrow}] = \int d\mathbf{r} \epsilon_{xc}(n_{\uparrow}, n_{\downarrow}, \nabla n_{\uparrow}, \nabla n_{\downarrow})n(\mathbf{r}). \quad (3.12)$$

with  $n = n_{\uparrow} + n_{\downarrow}$  and the electron spin densities  $n_{\uparrow}(\mathbf{r})$  and  $n_{\downarrow}(\mathbf{r})$ .

As the accuracy of the exchange energies is directly transferred to the total ground state energies the GGA can produce much better results for the crystal lattice parameters.

Perdew et al. [13] have for example shown that the total energies of various atoms and molecules can be calculated at much higher accuracy compared to the LDA. The GGA also tends to give better results for crystal lattice parameters and bond lengths making it the de-facto standard approximation in present-day DFT. It should be noted though that while reducing the error compared to LDA calculations the GGA has its deficiencies too, for example overestimating crystal lattice parameters and bond lengths. As both the LDA and the GGA are closely related to the homogenous electron gas the calculated value for the band gap can get underestimated drastically, as can be seen in section 4.3.4.

One of the most widely used functionals using the GGA is the PBE functional introduced by Perdew, Burke and Ernzerhof (PBE)[14] which is an analytical fit to the numerical GGA in which all parameters are fundamental constants. This marks an improvement to older functionals like the semi-empirical B88[15] or PW91[16]. To further improve the results for lattice properties and bulk exchange energies of metals the PBE functional was modified by recovering the gradient expansion for exchange over a wide range of density gradients. This approach resulted in the PBEsol[17] functional which is specially tailored for calculations of solids.

### 3.4. Non-local Contributions

To further increase the accuracy of DFT calculations functionals were introduced which include non-local interaction energies in the exchange-correlation term. In this work functionals using two different approaches were used: hybrid functionals using part of the exact Hartree-Fock in the exchange energy term and van der Waals DFT.

#### 3.4.1. Hybrid Functionals

In the approach used to construct the hybrid functionals the term for the exchange correlation energy  $E_{xc}$  is modified by adding part of the exact Hartree-Fock exchange energy to the usual GGA term. The correlation term is usually the same as for the GGA exchange functional. This results in a term for the exchange energy

$$E_{xc}^{hyb} = aE_x^{HF} + (1 - a)E_x^{GGA} + E_c^{GGA} \quad (3.13)$$

with the mixing parameter  $a$  which has to be determined by advanced many-body methods. One problem with this method is that the calculation of the exact Fock-exchange energy in solids with periodic boundary conditions is computationally very expensive due to the  $\frac{1}{r}$  decay of the energy. To mitigate this issue screened hybrid functionals have been introduced, where the Coulomb interaction term is decomposed into a short-range and a long-range part. The hybrid functional used in this work was proposed by Heyd, Scuseria and Ernzerhof (HSE06)[18] and replaces the long-range part of the exact exchange energy by the PBE exchange energy, resulting in the following term for the exchange energy:

$$E_{xc}^{HSE} = \frac{1}{4}E_x^{HF,sr} + \frac{3}{4}E_x^{PBE,sr} + E_x^{PBE,lr} + E_c^{PBE} \quad (3.14)$$

The HSE06 (just called HSE in this work) functional produces good results for the crystal lattice parameters, mitigating some of the deficiencies of the LDA and GGA approaches. As it simulates the electronic structure more accurately the results for the calculated band gap are much closer to experimental values, as can be seen in chapter 4.

### 3.4.2. Van der Waals-DFT

As the LDA and GGA functionals do not include non-local dispersive forces, they do not produce accurate results for weakly bonded systems. Of the many approaches to account for the non-local dispersion in DFT the non-local van der Waals density functional proposed by Langreth and Lundqvist[19] (vdW-DF) shows the most promising results. Here the exchange correlation energy term can be written as

$$E_{xc} = E_x^{GGA} + E_c^{LDA} + E_c^{nl} \quad (3.15)$$

with  $E_c^{nl}$  denoting the non-local correlation energy. In its simplest form it can be written as

$$E_c^{nl} = \frac{1}{2} \int d\mathbf{r} d\mathbf{r}' n(\mathbf{r}) \phi(\mathbf{r}, \mathbf{r}') n(\mathbf{r}') \quad (3.16)$$

where  $\phi(\mathbf{r}, \mathbf{r}')$  is a given, general function depending on  $\mathbf{r} - \mathbf{r}'$  and the densities  $n$  in the vicinity of  $\mathbf{r}$  and  $\mathbf{r}'$ .

$E_c^{nl}$  can now be calculated via a model response function for electron densities. As the exchange functional affects the interaction energy obtained with vdW-DF the choice which functional is used is important for the accuracy of the calculated interaction energies. Klimeš et al. [20] have shown that using a modified Becke88 (B88)[15] functional yields the best results for the S22 benchmark data set of weakly bonded dimers. This functional was named optB88 and got implemented in summer 2011 in the VASP DFT code[21].

## 3.5. Vienna Ab-initio Simulation Package (VASP)

All calculations presented in this work have been done with the VASP code, short for Vienna Ab-initio Simulation Package. It has mainly been developed by Kresse et al [22–25] at the Institute of Computational Physics of the University of Vienna. VASP uses a plane wave basis set and PAW potentials[26, 27] to treat the electronic exchange and correlation effects. The projector augmented wave method (PAW) is used to reduce the number of wave functions to be calculated and to build the PAW potentials with which the collective system of nuclei and core electrons are described. VASP can also calculate the full stress tensor for structure relaxation processes, and all the different functionals mentioned in the sections above are implemented in the VASP code.

VASP uses plain text files to control the input parameters and to write results to the hard drive. Important files are the INCAR, POSCAR, CONTCAR, POTCAR, KPOINTS, OUTCAR, CHGCAR and DOSCAR files.



- The INCAR file controls the settings for the calculation. Here VASP can be told for example which functional to use, whether to do ionic relaxations and at which accuracy, or the desired energy cutoff to be used in the calculations. A more comprehensive list of parameters used in this work is given in appendix A.
- The POSCAR file holds the lattice geometry and the positions of all atoms in the cell. It also includes the number of each element in the atomic cell. The coordinates can be given either in direct or cartesian coordinates. This file can also be used to switch on selective dynamics, which enables the fixation of atoms in a certain direction during the ionic relaxation, for example keeping one atom in place in the x-coordinate while letting relax in the y- and z-coordinate. The CONTCAR file has the same format as the POSCAR file and contains the positions of the atoms after each ionic relaxation step. Should the relaxation not converge in one run the content of the CONTCAR file can just be copied to the POSCAR file and the relaxation process can be restarted.
- As mentioned above VASP uses PAW potentials to account for the exchange correlation interaction, and these can be found in the POTCAR file. For each atomic species there exists a pre-calculated POTCAR file which contains the elements fundamental constants and the pseudo-potential. Since VASP version 5.2 the POTCAR files also include default values for the energy cutoff. If the studied cell contains multiple atomic species the POTCAR files of the corresponding elements need to be joined together in the same order as the atoms in the POSCAR file.
- The KPOINTS file contains information on how to create the  $k$ -point grid. VASP can automatically create even spaced grids of  $k$ -points by using the scheme of Monkhorst and Pack [28], either centered at the  $\Gamma$ -point or with even subdivisions shifted off the  $\Gamma$  point. Alternatively the  $k$ -points can be entered manually to generate strings of  $k$ -points connecting specific points in the Brillouin zone. This mode is particularly useful for band structure calculations.
- The OUTCAR file contains almost all relevant output from the calculations, for example the calculated energies, magnetic moments, the charge distribution, band structure and the stress tensor. Additionally it contains the coordinates of all  $k$ -points and the input settings read from the INCAR and POTCAR files. As this file is usually several thousands lines long it can be cumbersome to read, so to quickly get information on calculated energy of the current electronic or ionic step the OSZICAR file can be used.
- The CHGCAR file holds the same information on the lattice parameters as the CONTCAR file, but it also includes the total charge density multiplied by the cell volume on the fine FFT grid and the PAW one-center occupancies. It can be used to restart VASP from an existing charge density and to visualize the charge density of the cell.
- The densities of states and the integrated DOS are contained in the DOSCAR file. If site-projected DOS calculations are desired, a dataset for each ion is also included in this file.

## 4. The ZrO<sub>2</sub> Bulk

Experimentally, many different distinct phases of ZrO<sub>2</sub> have been observed, although some may be misinterpreted due to the difficulty to determine the exact structure. This is especially true for high pressure phases. In this chapter a thorough study of a number of ZrO<sub>2</sub> phases is presented, covering both high temperature and high pressure phases.

### 4.1. ZrO<sub>2</sub> Bulk Phases

#### 4.1.1. Monoclinic Phase

At ambient pressure all the different phases ZrO<sub>2</sub> assumes are well understood: at room temperature, ZrO<sub>2</sub> assumes a monoclinic ( $C_{2h}^5$ ,  $P2_1/c$ , Space-group 14) unit cell containing four ZrO<sub>2</sub> molecules ( $Z=4$ ), see fig. 4.1. This structure is also called *baddeleyite* and has first been described by McCullough and Trueblood [29]. The monoclinic phase is a heavily distorted fluorite (CaF<sub>2</sub>) structure with the Zr atom on 7 coordination, which means it has 7 oxygen atoms as nearest neighbors. The basis vectors of the primitive cell are

$$\begin{aligned} \mathbf{A}_1 &= a \mathbf{X} \\ \mathbf{A}_2 &= b \mathbf{Y} \\ \mathbf{A}_3 &= c \cos(\beta) \mathbf{X} + c \sin(\beta) \mathbf{Z} \end{aligned}$$

with  $\mathbf{X} = (X, Y, Z)$  representing a vector in cartesian coordinates. For the description of the fractional coordinates the Wyckoff notation[30] is used: zirconium and oxygen atoms occupy the Wyckoff positions 4e at  $\pm(x, y, z)$  and  $\pm(-x, y + 1/2, 1/2 - z)$ .

#### 4.1.2. Tetragonal Phase

At about 1440 K a martensitic phase transition from the monoclinic to a tetragonal ( $D_{4h}^{15}$ ,  $P4_2/nmc$ , Space-group 137) phase is observed. The zirconium atoms are 8-fold coordinated. According to Teufer [31] it represents a slightly distorted cubic CaF<sub>2</sub> structure where the oxygen atoms are displaced from their ideal cubic positions: alternating columns of oxygen atoms are shifted up and downwards in  $z$  direction. To make this displacement visible and to make it comparable to the cubic cell the structure is represented by a distorted body-centered cubic cell composed of two ZrO<sub>2</sub> formula units ( $Z=2$ ). The zirconium atoms can be found at  $(0, 0, 0)$  and  $(1/2, 1/2, 1/2)$  while the oxygen atoms occupy the positions at  $(1/2, 0, 1/2 - d_z)$ ,  $(1/2, 0, -1/2 + d_z)$ ,  $(0, 1/2, 1/2 + d_z)$

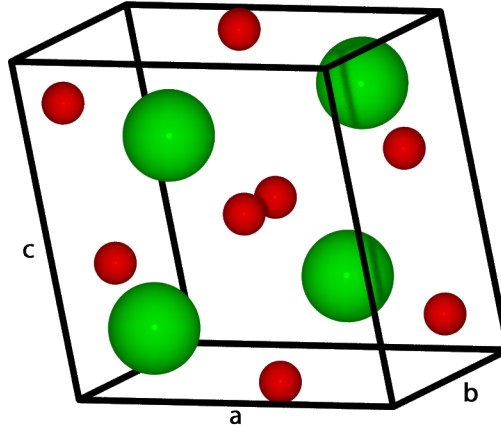


Figure 4.1.: Monoclinic  $\text{ZrO}_2$ . Green spheres correspond to zirconium, red to oxygen atoms.

and  $(0, 1/2, -1/2 - d_z)$ . The internal coordinate  $d_z$  is defined to represent the difference between the cubic and the tetragonal position of the oxygen atoms (see fig. 4.2). The basis vectors of the primitive cell are

$$\begin{aligned} \mathbf{A}_1 &= a \mathbf{X} \\ \mathbf{A}_2 &= a \mathbf{Y} \\ \mathbf{A}_3 &= c \mathbf{Z} \end{aligned}$$

with a  $c/a$  ratio of  $\approx 1.45$ .

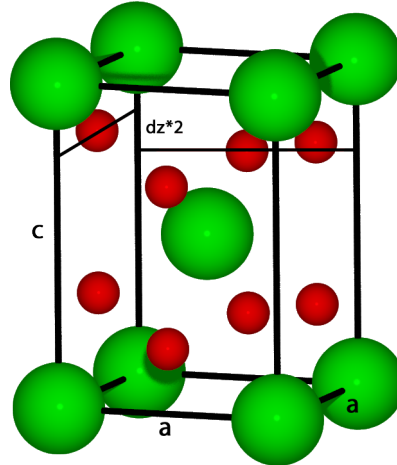


Figure 4.2.: Tetragonal  $\text{ZrO}_2$ . Green spheres correspond to zirconium, red to oxygen atoms.

### 4.1.3. Cubic Phase

Another phase transition takes place at a temperature of about 2650 K from the tetragonal to the cubic fluorite phase ( $O_h^5$ ,  $Fm\bar{3}m$ , Space-group 225). This structure is isostructural to  $\text{CaF}_2$  and the Zr atoms are in 8-fold coordination. The unit cell can be considered a special case of the tetragonal phase with a  $c/a$  ratio of  $\sqrt{2}$  and the oxygen atoms shifted along the  $z$  coordinate into central positions in the unit cell. There are multiple alternatives as to how the structure can be constructed, for better comparability a body centered cell similar to the tetragonal cell consisting of two  $\text{ZrO}_2$  formula units ( $Z=2$ ) was used. The atoms can be found at the same positions as with the tetragonal phase with the internal parameter  $d_z = 0$ . The basis vectors spanning the cubic fluorite cell are similar to the tetragonal cell mentioned before with a  $c/a$  ratio of  $\sqrt{2}$ .

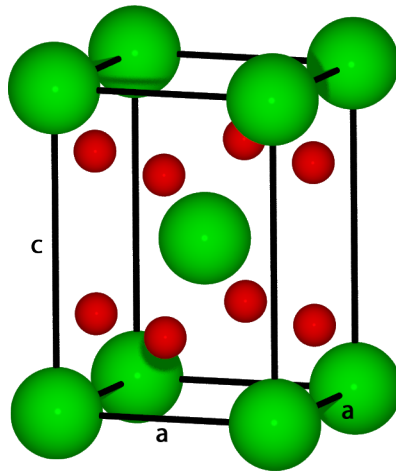


Figure 4.3.: Cubic  $\text{ZrO}_2$ . Green spheres correspond to zirconium, red to oxygen atoms.

### 4.1.4. Orthorhombic Phases

The structures of high pressure phases are not as well understood as the high temperature phases, but it is known that  $\text{ZrO}_2$  shows several orthorhombic phases at high pressure. Between 8 and 11 GPa a phase transition can be observed (see Leger et al. [32], Al-Khatatbeh et al. [33]) to an orthorhombic structure. While first studies using *in situ* X-ray diffraction identified this structure to be of  $Pbcm$  type (Kudoh et al. [34], Heuer et al. [35]), newer data gained from neutron powder experiments have indicated that the space group of this structure is  $Pbca$  (Howard et al. [36], Ohtaka et al. [37]). This structure consists of 8  $\text{ZrO}_2$  formula units in the primitive cell and the zirconium atom shows 7-fold coordination. One set of zirconium and two sets of oxygen atoms occupy the Wyckoff positions 8d:  $(x, y, z)$ ,  $(-x + 1/2, -y, z + 1/2)$ ,  $(-x, y + 1/2, -z + 1/2)$ ,  $(x + 1/2, -y + 1/2, -z)$ ,  $(-x, -y, -z)$ ,  $(x + 1/2, y, -z + 1/2)$ ,  $(x, -y + 1/2, z + 1/2)$  and  $(-x + 1/2, y + 1/2, z)$ .

At even higher pressures of 21–27 GPa [32, 33] another phase transition occurs. This

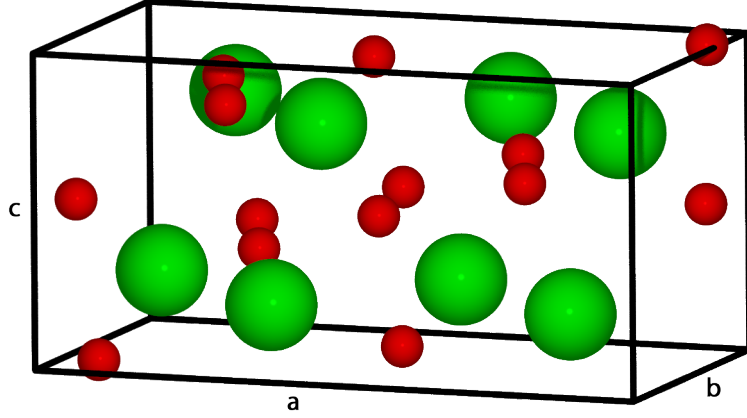


Figure 4.4.: Orthorhombic  $Pbca$  (Ortho-I). Green spheres correspond to zirconium, red to oxygen atoms.

structure has been identified by X-ray diffraction as an orthorhombic  $Pnma$  structure (Space-group 62) which is isostructural to cotunnite  $PbCl_2$ . Compared to the fluorite prototype this structure is the most heavily deformed. The zirconium atoms show a 9-fold coordination with the positions of the atoms at  $\pm(u, v, 1/4)$  and  $\pm(1/2 - u, v + 1/2, 1/4)$  in Wyckoff notation (position 4c) and the fractional parameters  $u$  and  $v$ .

The lattice of both orthorhombic structures is parametrized by the three lattice parameters  $a, b, c$ :

$$\begin{aligned} \mathbf{A}_1 &= a \mathbf{X} \\ \mathbf{A}_2 &= b \mathbf{Y} \\ \mathbf{A}_3 &= c \mathbf{Z} \end{aligned}$$

The orthorhombic  $Pbca$  phase will subsequently be called Ortho-I, while the orthorhombic  $Pnma$  phase will be denoted as Ortho-II.

It is not easy to get good results for the bulk properties like lattice parameters and compressibility from experimental measurements due to the high pressures at which these phases stabilize. Powdered  $ZrO_2$  which is used for these measurements does not provide direct information about the symmetry of the crystal, and due to the use of dopants like graphite to facilitate heating a comparison to data gained from pure zirconia is very difficult. Another issue with these experiments is that quenched samples are not in a thermodynamic equilibrium which can result in incorrect interpretation of the data due to lack of knowledge of the complete history of the sample.

## 4.2. Calculations

To compare the different functionals mentioned in chapter 3 a variety of functionals were used to treat the electronic exchange and correlation effects: LDA, PBE[14], PBEsol[17]

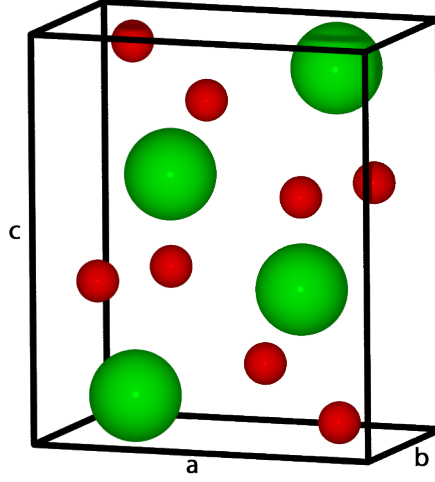


Figure 4.5.: Orthorhombic  $Pnma$  (Ortho-II). Green spheres correspond to zirconium, red to oxygen atoms.

and the HSE hybrid functionals proposed by Heyd, Scuseria and Ernzerhof[18].

To facilitate the comparison with results from other researchers the pre-generated potentials[27] distributed with VASP were used. The exact versions of the potentials can be found in table C.9. An energy cutoff of 400 eV was used, and the  $k$ -point meshes were automatically generated  $\Gamma$ -centered grids using the algorithm introduced by Monkhorst and Pack [28].

For the calculations both the internal coordinates and the cell shape were relaxed while keeping the volume of the cell constant<sup>1</sup> until the difference in the total energy between two ionic steps was smaller than  $10^{-4}$  eV. For the calculations using the HSE functional the structures were pre-relaxed with the PBE functional and then only 10 ionic steps were done with the HSE functional due to its high computational cost. The setting of the partial occupancies for the orbitals was done with the tetrahedron method with Blöchl corrections[38]<sup>2</sup> which the VASP authors recommended<sup>3</sup> for insulators.

To determine the appropriate density of the  $k$ -point mesh test calculations for each  $\text{ZrO}_2$  phase were done. The total energy with lattice parameters taken from the experiments were calculated at increasing numbers of  $k$ -points. The energies were then compared and the highest value where the difference in the energy for that phase was lower than 0.01% was then taken for the  $k$ -point mesh. The  $k$ -point meshes used for calculations with local functionals are noted in table 4.1.

For the calculations using the non-local HSE functionals different  $k$ -point meshes were used. To reduce the computing time the exact Hartree-Fock exchange energy was not calculated in the whole Brillouin zone but only for a sub-grid in close proximity to the

<sup>1</sup>VASP parameter: ISIF = 4

<sup>2</sup>VASP parameter: ISMEAR = -5

<sup>3</sup>see [http://cms.mpi.univie.ac.at/vasp/vasp/ISMEAR\\_SIGMA\\_FERWE\\_FERDO\\_SMEARINGS\\_tag.html](http://cms.mpi.univie.ac.at/vasp/vasp/ISMEAR_SIGMA_FERWE_FERDO_SMEARINGS_tag.html)

| Phase           | $k$ -point mesh          | irreducible $k$ -points |
|-----------------|--------------------------|-------------------------|
| Monoclinic      | $4 \times 4 \times 4$    | 30                      |
| Tetragonal      | $7 \times 7 \times 7$    | 64                      |
| Cubic           | $10 \times 10 \times 10$ | 10                      |
| Orthorhombic-I  | $8 \times 8 \times 8$    | 125                     |
| Orthorhombic-II | $4 \times 4 \times 4$    | 27                      |

Table 4.1.:  $K$ -point meshes used for the  $\text{ZrO}_2$  bulk calculations using local functionals.

primitive cell, and for the rest of the supercell the PBE exchange energy was added<sup>4</sup>. For this to work the  $k$ -point grid needs to be constructed of a grid of even numbers of  $k$ -points, resulting in the meshes shown in table 4.2.

| Phase           | $k$ -point mesh          | irreducible $k$ -points |
|-----------------|--------------------------|-------------------------|
| Monoclinic      | $6 \times 6 \times 6$    | 80                      |
| Tetragonal      | $10 \times 10 \times 10$ | 216                     |
| Cubic           | $10 \times 10 \times 10$ | 126                     |
| Orthorhombic-I  | $6 \times 6 \times 4$    | 48                      |
| Orthorhombic-II | $6 \times 6 \times 6$    | 64                      |

Table 4.2.:  $K$ -point meshes used for the  $\text{ZrO}_2$  bulk calculations using the HSE functional.

To determine the equilibrium volume the total energy was calculated at different cell volumes in the vicinity of the cell volume given by experiments, and the results were then fit to a third order Birch-Murnaghan equation of state as mentioned in section 2.4. To further improve the results for the lattice parameters another relaxation process was done at the equilibrium volume determined by the fit.

## 4.3. Results

### 4.3.1. Equation of State

To compare the energies of the different phases both the volume and the calculated total energy was divided by the number of formula units in the cell. Plotting the equations of state for the different  $\text{ZrO}_2$  phases show that all functionals correctly predict the order of stability of the different phases. According to the calculations the most stable phase is the monoclinic  $P2_1/c$  phase where the equilibrium volume is at the lowest energy. At higher energies all functionals predict the tetragonal ( $P4_2/nmc$ ) and the cubic ( $Fm\bar{3}m$ ) phase, in that order. The least stable  $\text{ZrO}_2$  phase according to the DFT calculations is

<sup>4</sup>VASP parameter: NKRED = 2

the orthorhombic  $Pnma$  phase for all but the LDA functional where the calculated total energy at a cell volume of  $120 \text{ \AA}^3$  of the orthorhombic phase has a lower energy than all volumes of the cubic phase. Calculating the total energy at the equilibrium volume gained by the fit the total energy per formula unit is again lower for the orthorhombic phase than for the cubic one by 5 meV. This is comparable to the results of both Dewhurst and Lowther [39] and Christensen and Carter [40] who found the orthorhombic phase at even lower energy than the monoclinic phase using a LDA functional and Troullier-Martins[41] PAW potentials respectively.

As can be seen in table 4.3 the energy difference at equilibrium volume differs for each functional, with the largest value given by the PBE functional and the lowest value by the LDA functional. This is also visible in the difference of the height of the equation of state plots in figs. 4.6a, 4.6b, 4.7a and 4.7b.

| $\Delta E/\text{meV}$ | Mono | Tetra | Cubic | Ortho-II |
|-----------------------|------|-------|-------|----------|
| LDA                   | 0    | 57    | 93    | 108      |
| PBE                   | 0    | 97    | 199   | 310      |
| PBEsol                | 0    | 79    | 144   | 179      |
| HSE                   | 0    | 97    | 166   | 294      |

Table 4.3.: Energy difference per formula unit at the equilibrium volume compared to the monoclinic phase.

The monoclinic phase shows an anomaly beginning at a cell volume of about  $140 \text{ \AA}^3$  ( $\approx 30\%$  more than the equilibrium volume depending on the functional) where another phase transition seems to occur. Analyzing the lattice parameters has not led to a definitive answer as to which final phase is involved. One would rather need calculations of these phonon eigenvectors to gain some knowledge about presumed soft modes and frequencies. Figures 4.6 and 4.7 show the calculated energies and the fit to the Birch-Murnaghan equation of state for each  $\text{ZrO}_2$  phase. For better comparability the x axis only shows the volume per formula unit between  $25 \text{ \AA}^3$  and  $45 \text{ \AA}^3$ , and the energy range shown on the y axis is 0.8 eV in all plots.

All calculated energies can be found in tables C.1 to C.4 and the fit parameters for the Birch-Murnaghan equation in tables C.5 to C.8.

### 4.3.2. Lattice Parameters

The comparison of the lattice parameters of the different phases at the respective equilibrium volume shows that the different functionals give results with different accuracy. For good comparability all volumes are given as volume per formula unit. As the LDA functional tends to over-bind the calculated cell volume is smaller compared to the experimental data by between 1.4% for the monoclinic phase and 1.9% for the orthorhombic phase. The PBE calculations on the other hand show that the generalized gradient approximation overestimates the lattice parameters. The different  $\text{ZrO}_2$  phases show an



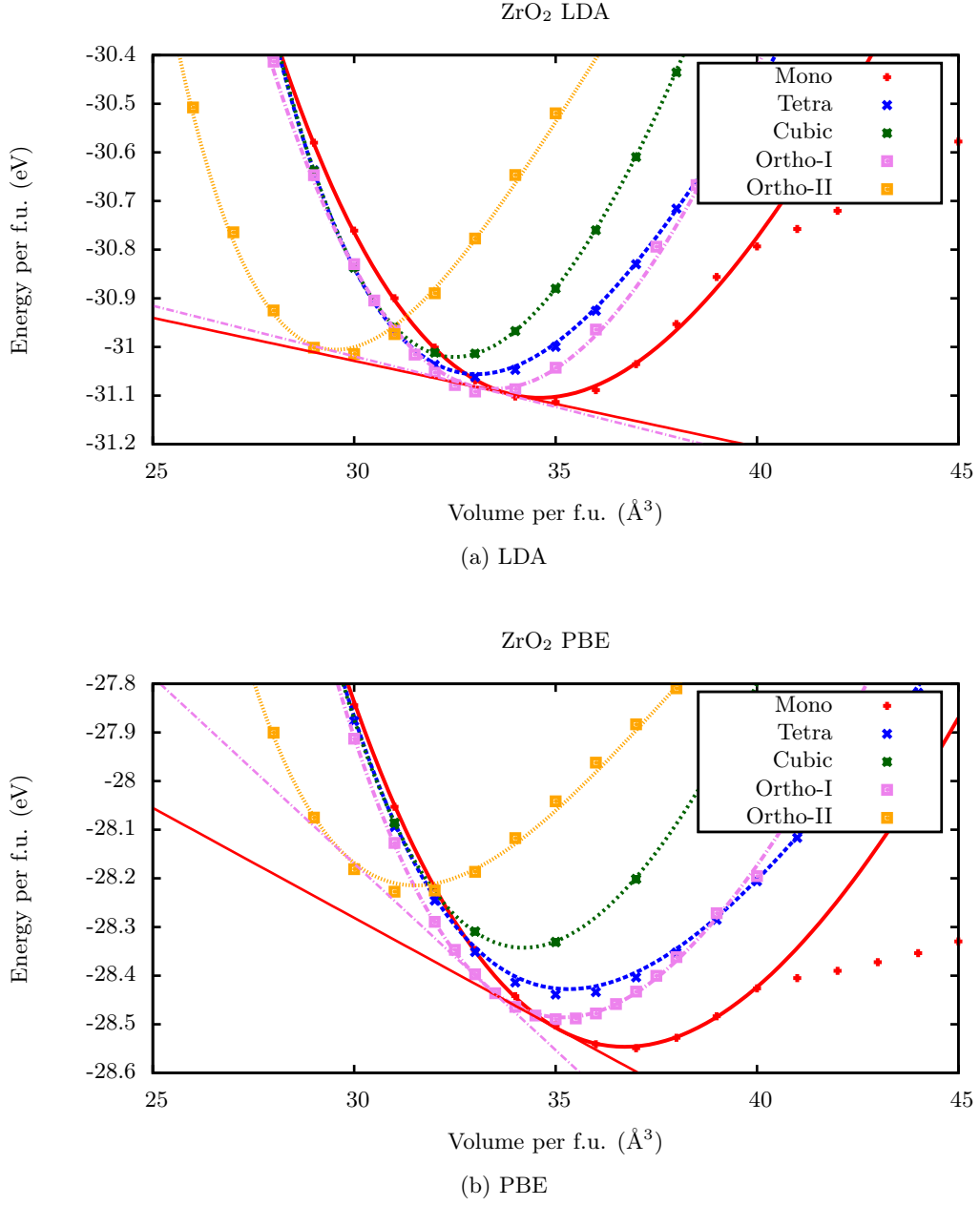


Figure 4.6.: Calculated total energy versus volume per formula unit (f.u.) of all five ZrO<sub>2</sub> phases with the LDA and the PBE functional. Points denote calculated energies, lines the fit to the Birch-Murnaghan equation of state. Tangents denote the transition pressures between the mono-ortho-I (red solid line) and the ortho-I-ortho-II phase (violet dashed line), also see section 4.3.3.

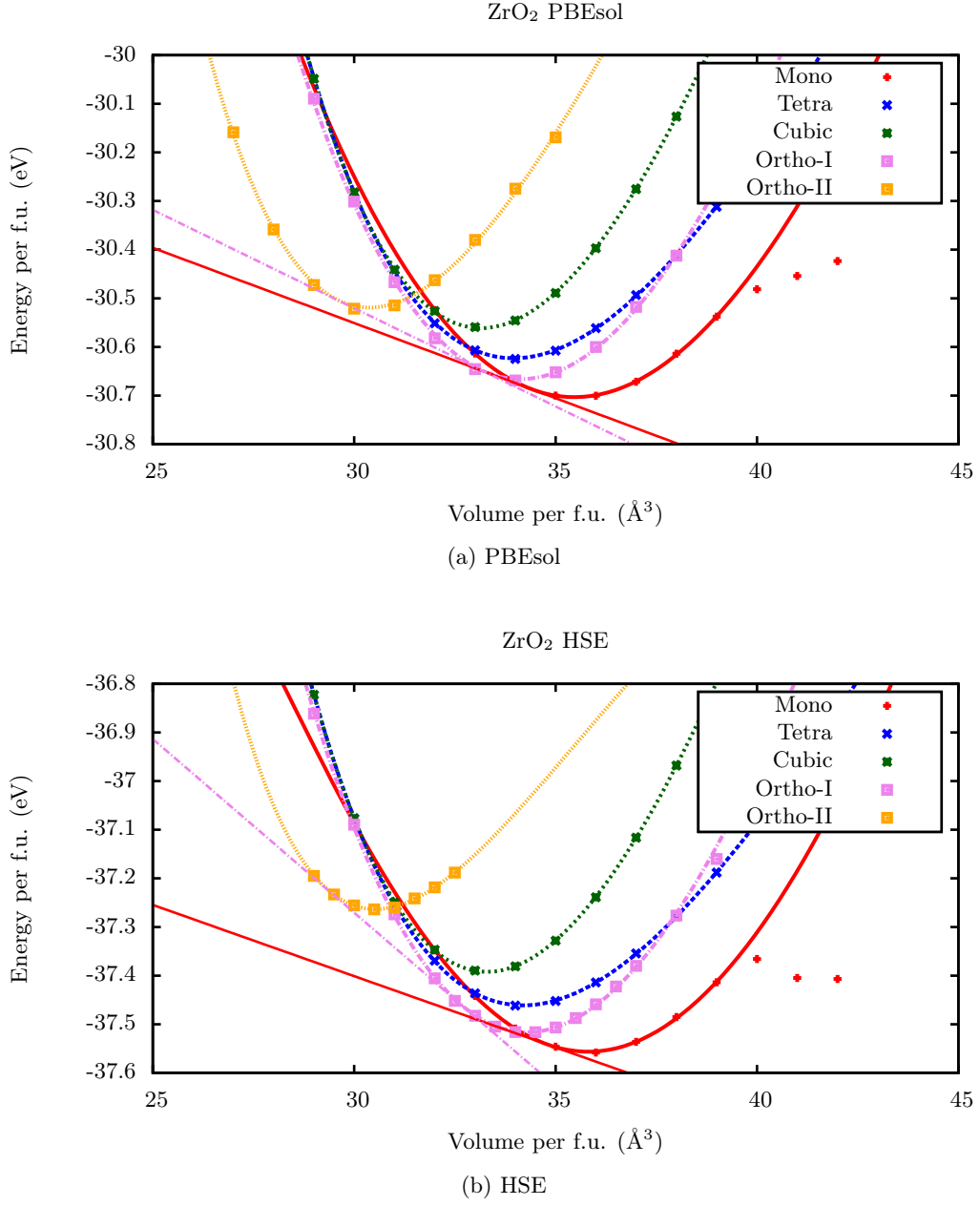


Figure 4.7.: Calculated total energy versus volume per formula unit (f.u.) of all five ZrO<sub>2</sub> phases with the PBEsol and the HSE functional. Points denote calculated energies, lines the fit to the Birch-Murnaghan equation of state. Tangents denote the transition pressures between the mono-ortho-I (red solid line) and the ortho-I-ortho-II phase (violet dashed line), also see section 4.3.3.

overestimation of the cell volume by 3 – 6%. The hybrid functionals improve the PBE result to an overestimation of only 1.2 – 2%, but only by using the PBEsol functional the prediction of the cell volume is improved to a deviation from experimental data of only  $\approx 1\%$ .

### Monoclinic

Compared to the experimental data by Howard et al. [42], the LDA functional underestimates the length of the cell vectors  $a$  and  $c$  by 0.44% and 0.49% respectively, while predicting the length of the  $b$  vector very accurately with a deviation of below 0.1%. This results in an underestimation of the cell volume of 0.97%. The predictions for the cell lengths calculated with the PBE functional show a different picture: all lattice parameters are elongated with respect to the experimental data by between 1.34% for the  $a$  vector to 1.54% and 1.59% for the  $b$  and  $c$  vector. This results in an expansion of the predicted cell volume of 4.59%. The HSE functional improves these results by reducing the overestimation of the cell edge lengths to 0.63%, 0.88% and 0.48% for the edges  $a$ ,  $b$ , and  $c$  respectively and of the cell volume to 1.93%. The best prediction of the lattice parameters is given by the PBEsol functional with a small overestimation of the volume by 0.83%, resulting from the elongation of the cell edges by 0.14%, 0.61% and 0.19% for the vectors  $a$ ,  $b$ , and  $c$  respectively. It should also be noted that the distortion of the cell represented by the angle  $\beta$  is larger for all functionals by up to  $0.48^\circ$  compared to the experimental data, with the best result given by the HSE functional at  $0.26^\circ$ . Compared to older research using LDA (Zhao and Vanderbilt [43], 2002) and GGA (Jaffe et al. [44], 2005) functionals where the cell volume is under- and overestimated by 2.46% and 2.74% respectively (see table 4.4) the results for all except the PBE functional presented in this work do fit the experimental data much better.

| Mono    | a/Å    | b/Å    | c/Å    | $\beta/^\circ$ | V/Å <sup>3</sup> |
|---------|--------|--------|--------|----------------|------------------|
| Exp[42] | 5.1505 | 5.2116 | 5.3173 | 99.23          | 35.68            |
| LDA     | 5.1277 | 5.2152 | 5.2915 | 99.62          | 34.88            |
| PBE     | 5.2196 | 5.2919 | 5.4017 | 99.71          | 36.77            |
| PBEsol  | 5.1575 | 5.2436 | 5.3276 | 99.64          | 35.51            |
| HSE     | 5.1829 | 5.2576 | 5.3429 | 99.49          | 35.90            |
| LDA[43] | 5.1083 | 5.1696 | 5.2717 | 99.21          | 34.35            |
| GGA[44] | 5.1974 | 5.2798 | 5.3498 | 99.53          | 36.19            |

Table 4.4.: Monoclinic  $P2_1/c$  lattice parameters.

A comparison of the deviation of the calculated internal coordinates of the atoms for the monoclinic cell shows that the HSE functional gives the best approximation at an average of 0.15%, followed by the PBEsol functional with an average of 0.30%. The other

local functionals are not far off at 1.25% for the LDA and 0.26% average deviation for the PBE functional, as can be seen in table 4.5.

| Mono    | $x_{Zr}$ | $y_{Zr}$ | $z_{Zr}$ | $x_{O_1}$ | $y_{O_1}$ | $z_{O_1}$ | $x_{O_2}$ | $y_{O_2}$ | $z_{O_2}$ |
|---------|----------|----------|----------|-----------|-----------|-----------|-----------|-----------|-----------|
| Exp[42] | 0.2754   | 0.0395   | 0.2083   | 0.0700    | 0.3317    | 0.3447    | 0.4496    | 0.7569    | 0.4792    |
| LDA     | 0.2783   | 0.0425   | 0.2097   | 0.0709    | 0.3377    | 0.3404    | 0.4475    | 0.7576    | 0.4810    |
| PBE     | 0.2755   | 0.0448   | 0.2106   | 0.0662    | 0.3291    | 0.3489    | 0.4525    | 0.7572    | 0.4735    |
| PBEsol  | 0.2776   | 0.0431   | 0.2096   | 0.0706    | 0.3373    | 0.3409    | 0.4482    | 0.7577    | 0.4799    |
| HSE     | 0.2761   | 0.0418   | 0.2093   | 0.0710    | 0.3372    | 0.3418    | 0.4512    | 0.7577    | 0.4786    |

Table 4.5.: Monoclinic  $P2_1/c$  internal parameters.

## Tetragonal

The comparison of the results for the tetragonal cell shows a similar picture to the monoclinic cell. The LDA functional again results in an underestimation of the lattice parameters of 0.54% and 0.71%, and therefore a reduction of the cell volume of 1.84% compared to the experimental data by Howard et al. [42]. The PBE functional expands the cell volume by 4.93%, a result of the elongation of the lattice parameters  $a$  and  $c$  by 1.24% and 2.50% respectively. Using the HSE functional improves these results to an expansion of the volume of only 1.57% as the length of the lattice vectors are overestimated by only 0.28% and 0.93% ( $a$  and  $c$ ). Again the PBEsol functional gives the best prediction for the lattice parameters, elongating the vectors  $a$  and  $c$  by only 0.17% and 0.67% and overestimating the cell volume by 1.01%. This is an improvement of older calculations which underestimate the volume by 4.16%[43] using a LDA functional or find a 2.41%[44] larger equilibrium volume using a PBE functional. Table 4.6 shows all relevant cell parameters of the tetragonal cell.

Looking at the internal parameter  $d_z$  it is surprising that the PBE functional gives the closest prediction of the displacement of the oxygen atom rows, while all other functionals give a much lower displacement.

## Cubic

As the only difference between the cubic and the tetragonal cell is the ratio  $c/a$  which is  $\sqrt{2}$  for the cubic cell and with the internal parameter  $d_z$  being zero, the results are quite similar to the tetragonal cell. The LDA functional gives more accurate results compared to the experimental data[42]. The calculated length of the cell edge is only 0.40 off the measured length which results in a reduction of the cell volume by 1.20%. Again the PBE functional gives an expanded cell volume by 2.97%, and using the HSE functional the predicted volume is only 1.23% bigger than the experimental findings. Similar to the other  $ZrO_2$  phases the PBEsol functional gives the best prediction of the cell volume resulting in an overestimation of only 0.93%.

| Tetra   | a/Å    | c/Å    | V/Å <sup>3</sup> | $d_z$ /Å |
|---------|--------|--------|------------------|----------|
| Exp[42] | 3.6055 | 5.1797 | 33.66            | 0.057    |
| LDA     | 3.5860 | 5.1430 | 33.04            | 0.0419   |
| PBE     | 3.6502 | 5.3094 | 35.32            | 0.0555   |
| PBEsol  | 3.6115 | 5.2142 | 34.00            | 0.0482   |
| HSE     | 3.6157 | 5.2281 | 33.30            | 0.0498   |
| LDA[43] | 3.5567 | 5.1004 | 32.26            |          |
| GGA[44] | 3.6287 | 5.2070 | 34.47            |          |

Table 4.6.: Tetragonal  $P4_2/nmc$  lattice parameters.

| Cubic   | c/Å    | V/Å <sup>3</sup> |
|---------|--------|------------------|
| Exp[42] | 5.0858 | 32.89            |
| LDA     | 5.0651 | 32.50            |
| PBE     | 5.1354 | 33.87            |
| PBEsol  | 5.1011 | 33.20            |
| HSE     | 5.1063 | 34.37            |
| LDA[43] | 5.0371 | 31.95            |
| GGA[44] | 5.1280 | 33.71            |

Table 4.7.: Cubic  $Fm\bar{3}m$  lattice parameters.

### Orthorhombic-I

The calculated lattice parameters for the orthorhombic *Pbca* phase show a deviation similar to the cubic and tetragonal phases. Again the LDA functional underestimates the cell volume by 1.13%, while the PBE functional overestimates it by 4.12% compared to the experimental values published by Ohtaka et al. [37]. Using the HSE functional improves the predicted cell volume to an overestimation of 1.48%, but the best agreement is again given by the PBEsol functional with an overestimation of the cell volume of only 0.86%. As can be seen in table 4.9 the values of the internal coordinates of the atoms are very similar for all four functionals and do not deviate much from the experimental values.

| Ortho-I | a/Å     | b/Å    | c/Å    | V/Å <sup>3</sup> |
|---------|---------|--------|--------|------------------|
| Exp[37] | 10.0861 | 5.2615 | 5.0910 | 33.77            |
| LDA     | 10.0430 | 5.2488 | 5.0656 | 33.39            |
| PBE     | 10.2157 | 5.3329 | 5.1628 | 35.16            |
| PBEsol  | 10.1069 | 5.2833 | 5.1029 | 34.06            |
| HSE     | 10.1224 | 5.2953 | 5.1129 | 34.27            |
| GGA[45] | 10.1500 | 5.2900 | 5.1200 | 34.40            |

Table 4.8.: Orthorhombic *Pbca* (Ortho-I) lattice parameters.

| Ortho-I | x <sub>Zr</sub> | y <sub>Zr</sub> | z <sub>Zr</sub> | x <sub>O<sub>1</sub></sub> | y <sub>O<sub>1</sub></sub> | z <sub>O<sub>1</sub></sub> | x <sub>O<sub>2</sub></sub> | y <sub>O<sub>2</sub></sub> | z <sub>O<sub>2</sub></sub> |
|---------|-----------------|-----------------|-----------------|----------------------------|----------------------------|----------------------------|----------------------------|----------------------------|----------------------------|
| Exp[37] | 0.8843          | 0.0332          | 0.2558          | 0.7911                     | 0.3713                     | 0.1310                     | 0.9779                     | 0.7477                     | 0.4948                     |
| LDA     | 0.8849          | 0.0348          | 0.2528          | 0.7910                     | 0.3764                     | 0.1287                     | 0.9770                     | 0.7390                     | 0.4976                     |
| PBE     | 0.8844          | 0.0348          | 0.2517          | 0.7891                     | 0.3733                     | 0.1242                     | 0.9779                     | 0.7388                     | 0.4973                     |
| PBEsol  | 0.8847          | 0.0350          | 0.2526          | 0.7906                     | 0.3758                     | 0.1283                     | 0.9772                     | 0.7388                     | 0.4975                     |
| HSE     | 0.8844          | 0.0343          | 0.2535          | 0.7897                     | 0.3739                     | 0.1266                     | 0.9782                     | 0.7388                     | 0.4981                     |

Table 4.9.: Orthorhombic *Pbca* (Ortho-I) internal parameters.

### Orthorhombic-II

Due to the difficulties of measuring the exact lattice parameters for the orthorhombic *Pmna* phase described in section 4.1.4 the accuracy of the calculations cannot be assessed as well as for the other ZrO<sub>2</sub> phases. Compared to the measurements of Haines et al. [46] done in 1997, the relative deviation of the predicted cell volumes is similar to that of the monoclinic phase. The LDA functional again over binds which results in a calculated cell volume 1.55% smaller than measured. The PBE functional overestimates the volume

by 5.02%, and using hybrid functionals this overestimation gets reduced to 1.97%. As with the other phases the PBEsol functional results in the best prediction of the cell volume with a deviation of 1.16%. Another difference in the predicted lattice parameters is that both the LDA and the PBE functional distort the cell with the LDA calculations elongating the cell in the x direction while compressing it in y and z direction. The PBE functional on the other hand shows a greater expansion of the cell in the x direction than in the y and z direction. The other two functionals show a more uniform expansion in all directions.

| Ortho-II | a/Å    | b/Å    | c/Å    | V/Å <sup>3</sup> |
|----------|--------|--------|--------|------------------|
| Exp[47]  | 5.7410 | 3.2460 | 6.3410 | 29.54            |
| Exp[46]  | 5.5587 | 3.3298 | 6.4847 | 30.16            |
| LDA      | 5.5774 | 3.2869 | 6.4455 | 29.54            |
| PBE      | 5.6825 | 3.3778 | 6.5671 | 31.51            |
| PBEsol   | 5.5938 | 3.3331 | 6.5127 | 30.36            |
| HSE      | 5.5921 | 3.3538 | 6.5258 | 30.60            |
| LDA[39]  | 5.5980 | 3.3400 | 6.5530 | 30.63            |
| GGA[44]  | 5.6140 | 3.3474 | 6.5658 | 30.86            |

Table 4.10.: Orthorhombic *Pnma* (Ortho-II) lattice parameters.

The internal coordinates do not vary much when comparing the different functionals. Due to the aforementioned difficulty of doing measurements on orthorhombic *Pnma* zirconium the comparison to the experimental values should be taken with a grain of salt, see table 4.11. The average difference to the experimental values is 1.6%, 2.4%, 0.4% and 1.6% for the LDA, PBE, PBEsol and HSE functional. Again the PBEsol results in the best prediction of the internal coordinates of the atoms.

| Ortho-II | u <sub>Zr</sub> | v <sub>Zr</sub> | u <sub>O<sub>1</sub></sub> | v <sub>O<sub>1</sub></sub> | u <sub>O<sub>2</sub></sub> | v <sub>O<sub>2</sub></sub> |
|----------|-----------------|-----------------|----------------------------|----------------------------|----------------------------|----------------------------|
| Exp[47]  | 0.2510          | 0.1090          | 0.3640                     | 0.4220                     | 0.0210                     | 0.3280                     |
| Exp[46]  | 0.2459          | 0.1108          | 0.3599                     | 0.4248                     | 0.0250                     | 0.3388                     |
| LDA      | 0.2451          | 0.1147          | 0.3596                     | 0.4272                     | 0.0264                     | 0.3374                     |
| PBE      | 0.2452          | 0.1152          | 0.3591                     | 0.4277                     | 0.0274                     | 0.3361                     |
| PBEsol   | 0.2463          | 0.1123          | 0.3598                     | 0.4260                     | 0.0252                     | 0.3383                     |
| HSE      | 0.2481          | 0.1088          | 0.3606                     | 0.4241                     | 0.0229                     | 0.3400                     |

Table 4.11.: Orthorhombic *Pnma* (Ortho-II) internal parameters.

### 4.3.3. Bulk Moduli and Transition Pressures

The bulk modulus of a substance characterizes its resistance to uniform compression. It is defined as the ratio of an infinitesimal pressure applied to a substance to the relative change of its volume and its base unit is Pascal (Pa). Typical bulk moduli of Zirconia determined by experiments are between 150 GPa and 332 GPa, as can be seen in table 4.12. To determine the bulk modulus of a specific structure the fit to the Birch-Murnaghan equation is used as it is the variable  $B_0$  of said equation.

For both the monoclinic and the orthorhombic *Pnma* phase the calculated values of all functionals are 10% – 37% less than the experimental values, while for the tetragonal and the cubic phases the calculated bulk moduli are close to experimental values. The calculated values for the orthorhombic *Pbca* phase only comes close to the lowest value determined by experiments when using the HSE functional. As there are multiple methods to measure the bulk modulus and as the preparation of the sample can influence the measurements the spread in the experimental data is quite large. It should also be stated that the high bulk modulus measured by some groups for the orthorhombic phase (444 GPa by Desgreniers and Lagarec [48]) could not be confirmed.

| Bulk Modulus/GPa | Mono    | Tetra               | Cubic               | Ortho-I             | Ortho-II            |
|------------------|---------|---------------------|---------------------|---------------------|---------------------|
| LDA              | 151     | 201                 | 267                 | 201                 | 251                 |
| PBE              | 149     | 155                 | 232                 | 187                 | 176                 |
| PBEsol           | 162     | 181                 | 250                 | 208                 | 229                 |
| HSE              | 166     | 177                 | 258                 | 219                 | 240                 |
| Exp              | 187[49] | 149[50]<br>-183[49] | 194[51]<br>-254[51] | 210[32]<br>-281[48] | 278[52]<br>-332[47] |

Table 4.12.: Calculated bulk moduli for all functionals and structures.

To determine the transition pressure between the phases a common tangent construction was used where the transition pressure corresponds to the gradient of the tangent. The tangents displayed in figs. 4.6 and 4.7 show the pressure induced transitions from the monoclinic to the orthorhombic *Pbca* phase and from the orthorhombic *Pbca* to the orthorhombic *Pnma* phase is predicted correctly with all four functionals. A comparison of the calculated values for the transition pressure to the experimental data mentioned in section 4.1.4 shows that the PBE functional predicts the experimentally observed values the closest, while especially the PBEsol and the LDA functionals underestimate them severely. It should nevertheless be noted that the results compare well to other calculations, for example Terki et al. [45] calculated a transition pressure of 8 GPa and 12 GPa for the monoclinic – orthorhombic *Pbca* and the orthorhombic *Pbca* – orthorhombic *Pnma* phase transition respectively using PBE with WIEN2k[53].



| Transition pressure/GPa | m-t | t-c | c-o <sub>2</sub> | m-o <sub>1</sub> | o <sub>1</sub> -o <sub>2</sub> |
|-------------------------|-----|-----|------------------|------------------|--------------------------------|
| LDA                     | 6   | 29  | 1                | 3                | 3                              |
| PBE                     | 17  | 29  | 7                | 7                | 12                             |
| PBEsol                  | 10  | 29  | 2                | 5                | 6                              |
| HSE                     | 32  | 11  | 8                | 5                | 11                             |

Table 4.13.: Transition pressures - m: Monoclinic, t: Tetragonal, c: Cubic, o<sub>1</sub>: Orthorhombic-I, o<sub>2</sub>: Orthorhombic-II.

#### 4.3.4. Electronic structures

The densities of states for all five phases were also calculated using the four different functionals. The total DOS is composed of two valence bands and one conduction band. As can be seen in fig. 4.8, the DOS for the different phases are very similar. The lower valence band lies at about  $-17$  eV and has O- $2s$  character, while the upper valence band with O- $2p$  character lies between  $\approx -5$  eV and  $0$  eV. After a band gap a conduction band of Zr- $4d$  type forms. It is noticeable that the LDA, PBE and PBEsol functional give quite similar values for the position of the bands and the width of the band gap, while HSE functional results in a much larger band gap. The values for the band gap given in table 4.14 show that using hybrid functionals gives much better results for band structure calculations compared to experimental values. The disadvantage of using hybrid functionals is the much higher computational cost. Currently these calculations cannot be parallelized in an efficient manner, so calculating the exact Hartree-Fock exchange energies takes up to 520 times longer compared to a PBE calculation.

| Band Gap/eV    | Mono | Tetra | Cubic | Ortho-I | Ortho-II |
|----------------|------|-------|-------|---------|----------|
| LDA            | 3.45 | 3.84  | 3.12  | 3.65    | 2.70     |
| PBE            | 3.50 | 3.90  | 3.15  | 3.59    | 2.79     |
| PBEsol         | 3.45 | 3.85  | 3.15  | 3.62    | 2.73     |
| HSE            | 5.13 | 5.52  | 4.80  | 5.37    | 4.38     |
| Exp (EELS)[54] | 4.20 | 4.20  | 4.60  | n.a.    | n.a.     |
| Exp (VUV)[55]  | 5.83 | 5.78  | 6.10  | n.a.    | n.a.     |

Table 4.14.: Calculated and measured band gaps.

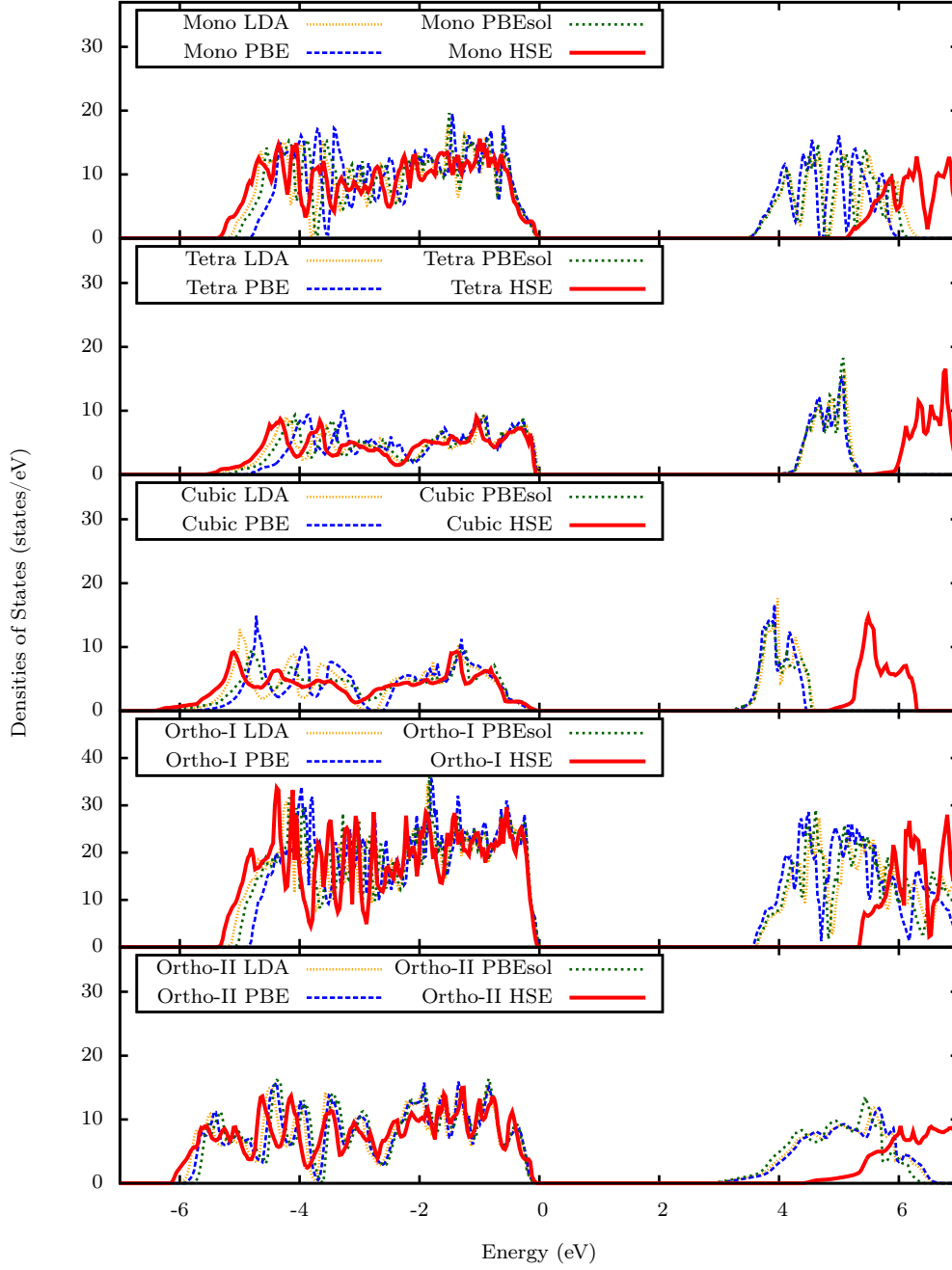


Figure 4.8.:  $\text{ZrO}_2$  densities of states. The DOS calculated with the HSE functional is shown in red, highlighting the larger band gap.

## 4.4. Conclusion

A comparison of the four different functionals has revealed that they all predict the order of stability correctly with the two PBE functionals being more accurate. Both the tendency of the LDA functional to over-bind and the overestimation of the lattice parameters of the PBE functional could be confirmed by the calculations. The PBEsol functional did produce the best results for the crystal lattice parameters due to it being tailored for solids. While the non-local HSE functional has produced slightly better results than the PBE functional the high computational cost makes them less useful when the accuracy of the electronic structure is not that important. The values for the bulk moduli and transition pressures tend to get underestimated with all four functionals with LDA giving the least accurate results, while the electronic structure is best represented by the hybrid functionals.

## 5. The $\text{Pt}_3\text{Zr-ZrO}_2$ Interface

### 5.1. Introduction

In this chapter a first-principles study of both the  $\text{Pt}_3\text{Zr}$  bulk and the  $\text{Pt}_3\text{Zr-ZrO}_2$  interface is presented. First, the results of an investigation of the bulk and surface structure of  $\text{Pt}_3\text{Zr}$  are presented, followed by an in-depth analysis of the interface between a monolayer of  $\text{ZrO}_2$  and the  $\text{Pt}_3\text{Zr}$  bulk.

### 5.2. Experiment

The high melting point of zirconium (ca. 2130 K) makes it very difficult to obtain thin  $\text{ZrO}_2$  films from evaporation from a heated crucible. Another approach would be to evaporate a rod of  $\text{ZrO}_2$  in an ultrahigh vacuum electron beam evaporator, but the low vapor pressure at the melting point makes this a very lengthy process. A more useful approach to create the  $\text{ZrO}_2$  film is oxidation of a suitable metallic alloy. It has been shown that either an alloy with a low concentration of the reactive metal (e.g. Copper with 9 atom-percent of Aluminum[56]) or a so-called super alloy which show strong chemical ordering and high stability can be used. This is an important precondition for the formation of well-ordered oxide films. Well known examples for this approach are  $\text{NiAl}(110)$ [57, 58] and  $\text{Ni}_3\text{Al}(111)$ [59]. In the experiments which accompanied this theoretical work a  $\text{Pt}_3\text{Zr}$  (0001) substrate has been used to grow the ultra-thin  $\text{ZrO}_2$  films.

The exact steps taken are documented in the soon to be published paper by Antlanger et al. [4].

### 5.3. The $\text{Pt}_3\text{Zr}$ Substrate

#### 5.3.1. Bulk Structure

$\text{Pt}_3\text{Zr}$  has a high melting point of 2427 K which is significantly higher than that of pure Platinum or Zirconium at 2042 K and 2128 K respectively[60]. According to Predel [60] its structure shows a hexagonal lattice similar to the  $\text{Ni}_3\text{Ti}$  crystal (Strukturbericht designation:  $\text{D0}_{24}$ ). It consists of layers of Zr atoms surrounded by Pt neighbors which are arranged in an ABAC stacking. As can be seen in fig. 5.1, the crystal can be described as a hybrid of a hexagonally close-packed and a face-centered cubic structure.

To determine whether the DFT calculations would give good results for the  $\text{Pt}_3\text{Zr}$  surface the optimal lattice parameters were calculated of the bulk crystal using both GGA

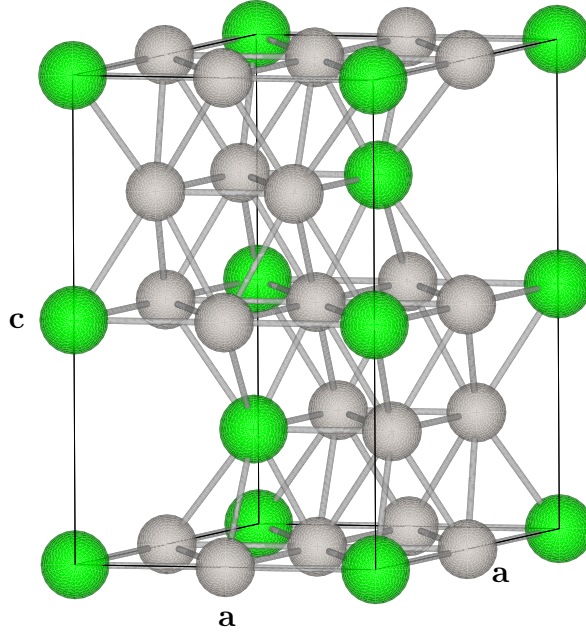


Figure 5.1.:  $\text{Pt}_3\text{Zr}$  crystal structure. Zr atoms are colored green, Pt atoms grey. The values for the lattice parameters are given in table 5.1.

(PBE) and vdW-DF (optB88) functionals using an approach similar to the calculations done on the  $\text{ZrO}_2$  bulk phases described in section 4.2. VdW-DF was used to account for weak interacting forces in the crystal. The PAW potentials used are described in table C.9. For the calculations a  $12 \times 12 \times 12$   $\Gamma$ -centered  $k$ -point grid which corresponds to 301 irreducible  $k$ -points was used. As a first step the total energy was calculated for different static crystal volumes while simultaneously relaxing both the lattice parameters and all internal degrees of freedom<sup>1</sup> for the GGA (PBE) functional. Similar to the procedure described for the  $\text{ZrO}_2$  bulk calculations the results were then fit to a Birch-Murnaghan equation of state (see section 2.4) to determine the equilibrium volume. Due to constraints in the implementation of the vdW-DF algorithm in VASP it was not possible at the time of this research to optimize the unit cell directly when using vdW-DF functionals, so the GGA lattice parameters were used and the cell shape was fixed<sup>2</sup> to determine the equilibrium volume when using vdW-DF. The comparison between the calculated values shown in table 5.1 and the measurements taken by Predel [60] (also see fig. 5.1) shows that both GGA and vdW-DF overestimate the lattice parameters by about 1.7% and 1.9% respectively, while the volume is overestimated by about 5.5% for the PBE functional and 6.1% for the optB88 functional. The calculated interlayer distance is 234.1 pm for the PBE and 234.5 pm for the optB88 functional. The deviation of these

<sup>1</sup>VASP parameter: ISIF = 4

<sup>2</sup>VASP parameter: ISIF = 2

results from the experimental data is in accordance with the  $\text{ZrO}_2$  bulk calculations done in section 4.3.2.

|                  | PBE   | optB88 | Exp.[60] |
|------------------|-------|--------|----------|
| a/Å              | 5.729 | 5.742  | 5.624    |
| c/Å              | 9.364 | 9.380  | 9.213    |
| V/Å <sup>3</sup> | 266.3 | 267.8  | 252.4    |

Table 5.1.: Lattice parameters and equilibrium volume for bulk  $\text{Pt}_3\text{Zr}$ .

### 5.3.2. Surface Termination

The experimental data mentioned in section 5.2 show that the surface of a well prepared  $\text{Pt}_3\text{Zr}(0001)$  sample exhibits large terraces with a step height of 4.5 Å or an integer multiple thereof. This value is about double the measured layer distance which means that the surface of the substrate is terminated by either an A or a B/C layer. As a prerequisite to building a model to simulate the interface between the substrate and the  $\text{ZrO}_2$  film it was therefore important to first examine the termination of the substrate crystal. To achieve this calculations have been done of both pure and Platinum terminated  $\text{Pt}_3\text{Zr}$  slabs to determine the various crystal parameters, and by determining the total or surface energy of both configurations of  $\text{Pt}_3\text{Zr}$  it was possible to resolve which layer should be the terminating layer. For all the calculations used in the following sections only the PBE functional was used unless otherwise noted.

#### ABA vs CAB

As a first step this approach was tested on small slabs consisting only of 3 layers in an ABA and a CAB configuration (see fig. 5.2). The lattice parameters for these slabs were taken from the results shown in table 5.1 with the addition of  $\sim 14.7$  Å vacuum in the z coordinate. To calculate the total energy a  $8 \times 8 \times 1$   $\Gamma$ -centered  $k$ -point grid (21 irreducible  $k$ -points) and an energy cutoff of 400 eV was used. The cell shape and volume was held in place while the internal coordinates were able to relax during the calculations<sup>3</sup>. As can be seen in table 5.2 the total energy for the ABA type slab is 439 meV lower than for the CAB slab and the surface energy per atom is 54 meV lower for the ABA type as well. These values gave a first hint that the terminating layer of the  $\text{Pt}_3\text{Zr}$  slab should be of the A type.

---

<sup>3</sup>VASP parameter: ISIF = 2

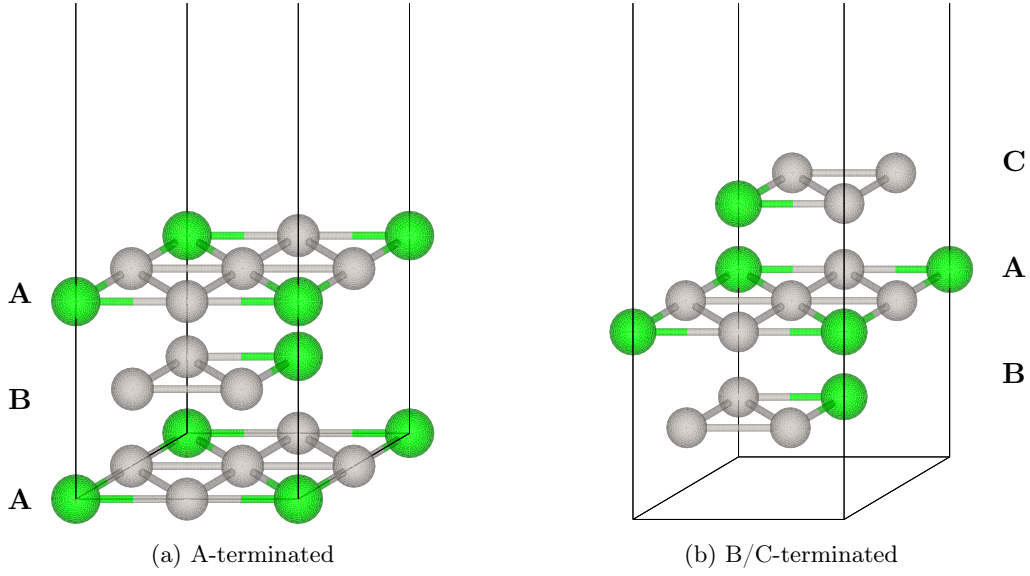


Figure 5.2.: Slabs consisting of 3 layers of  $\text{Pt}_3\text{Zr}$ , both in ABA and CAB configuration.

### 5- and 7-layered Slabs

As the 3-layer model is fairly inadequate when compared to the real substrate crystal (e.g. contraction of the interlayer distance<sup>4</sup> by 1.8%) further calculations with thicker slabs consisting of 5 and 7 layers were done. Again a  $12 \times 12 \times 1$   $\Gamma$ -centered  $k$ -point grid (ABACA: 43, BACAB, ABACABA, CABACAB: 74 irreducible  $k$ -points) and a cutoff energy of 400 eV were used. The results showed that the outer layers of all four configurations move inwards by about 2% to an interlayer distance of about 230 pm compared to the bulk interlayer distance. The distance between the second and third layer on the other hand increases by about 0.8% to  $\approx 236$  pm. The calculated surface energy per surface atom for the A-terminated 5-layered slab (ACABA stacking, see fig. 5.3a) is 0.73 eV, which is 66 meV lower than for the C-terminated (CABAC stacking, see fig. 5.3b) slab of the same size. As shown in table 5.2 the similar results for the 7-layer slab confirm the hypothesis that the surface is terminated by an A-type layer.

A close look at the atomic coordinates of the fully relaxed 7-layered slab reveals that the Zirconium atoms on the surface sit 15 pm lower than the surrounding Platinum atoms so that the surface shows a small amount of buckling. In the second monolayer the Zirconium atoms buckle up towards the surface by the same amount. Compared to the interlayer distance obtained from the bulk calculations of 234.1 pm the distance between the first and the second monolayer is only 229.5 pm, and the distance between the second and third monolayer 236.1 pm. This means a contraction of the distance between the first two layers of 1.96% and an expansion of 0.86% by the second two layers.

<sup>4</sup>The interlayer distance is the difference between the average height of the atoms in each layer.

| layer | termination | Energy/eV |
|-------|-------------|-----------|
| 3     | A           | -86.781   |
|       | B/C         | -86.359   |
| 5     | A           | -148.737  |
|       | B/C         | -148.224  |
| 7     | A           | -210.627  |
|       | B/C         | -210.264  |

Table 5.2.: Calculated total and surface energies for the  $\text{Pt}_3\text{Zr}$  slab configurations.

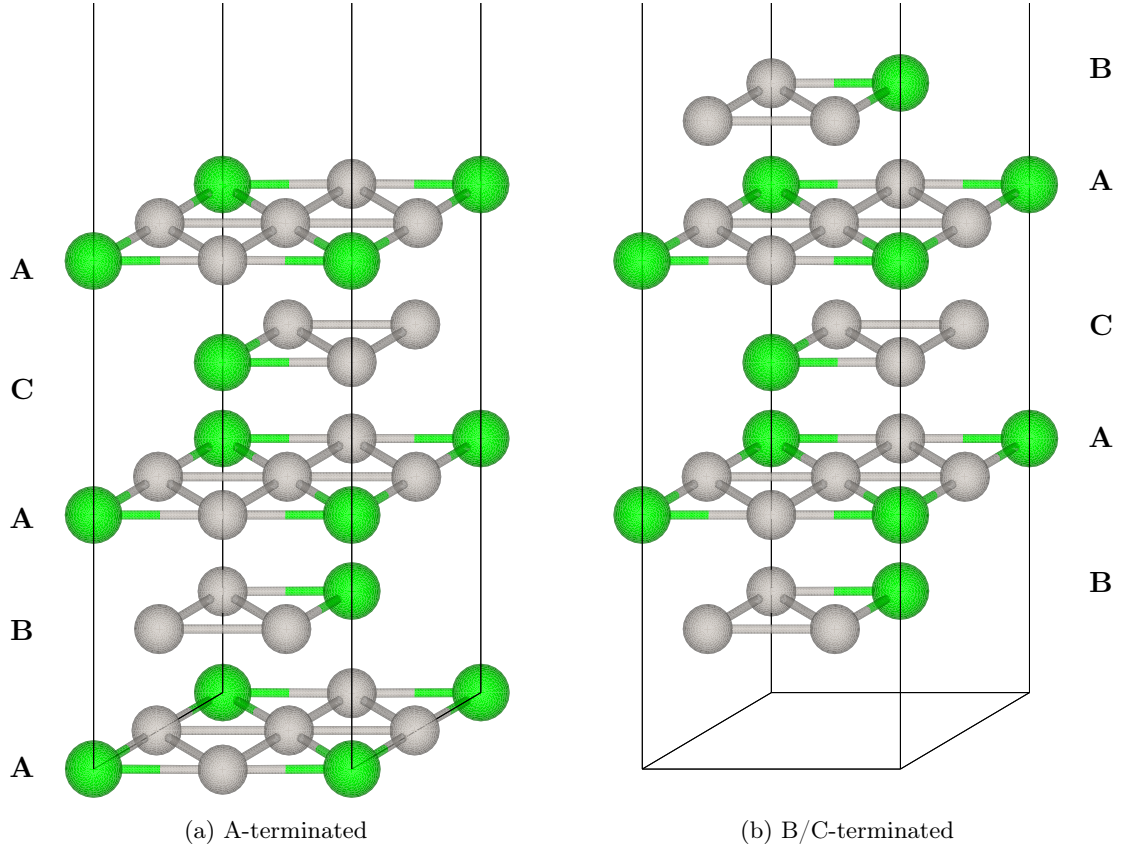


Figure 5.3.: Slabs consisting of 5 layers of  $\text{Pt}_3\text{Zr}$ , both in ABACA and BACAB configuration.



### Pt-terminated Slab

To further refine the model for the substrate more simulations were done using a slab terminated by a full Platinum layer. As described in section 5.2 the  $\text{ZrO}_2$  film is created by oxidation of the  $\text{Pt}_3\text{Zr}$  surface which means liberating Zr atoms from the alloy and results in a Platinum-rich surface. To construct the Pt-terminated slabs the surface Zr atoms were simply replaced by Pt atoms, and again 5- and 7-layered A- and B/C-terminated slabs were compared. It is not trivial to calculate the surface energy for each slab because there are not the same numbers of atoms for each termination, so only the total energies were compared. As can be seen in table 5.3 the total energy is lower for all A-terminated configurations, especially for the 5-layered slab with the Pt termination on one side where the total energy is 297 meV lower than for the B/C-terminated configuration.

Compared to the pure  $\text{Pt}_3\text{Zr}$  surface there also exists slight buckling of the surface by 8 pm because the Platinum atom which has a Zirconium atom below it in the third monolayer moves down, while the Zirconium atom in the second monolayer moves towards the surface by 16 pm. Similar to the pure  $\text{Pt}_3\text{Zr}$  surface the distance between the first and second monolayer decreases by 2%, and also the distance between second and third monolayer decreases by 0.9%. Compared to the pure slab this means a compression of the two outer layers from 465.6 pm to 461.5 pm (a difference of 4.1 pm or 0.9%).

| layer | termination | Energy/eV |
|-------|-------------|-----------|
| 5     | A           | -142.669  |
|       | B/C         | -142.372  |
| 7     | A           | -204.543  |
|       | B/C         | -202.891  |

Table 5.3.: Calculated total energies of the Pt-terminated  $\text{Pt}_3\text{Zr}$  slab configurations.

### 5.4. The $\text{ZrO}_2$ film

The STM images mentioned in [4] show that the  $\text{ZrO}_2$  film consists of a hexagonal lattice, and additional Auger measurements confirmed the existence of only one such  $\text{ZrO}_2$  layer on top of the Pt-terminated substrate. The exhibited lattice suggests the existence of a  $\text{ZrO}_2(111)$  layer which has also been observed after oxidation and deposition of Zr on  $\text{Pt}(111)$  crystals[1–3]. The lattice constant of this layer was determined to be 350(2) pm. A Fourier transform of the STM images show that the superstructure cell is commensurate because both the Fourier spots of the substrate cell (280 pm lattice constant) and the oxide are on lattice points of the superstructure reciprocal lattice. The measurements have shown that the reciprocal lattice of the oxide has a side length of  $2\sqrt{3}$  while the side length of the metal substrate is  $\sqrt{19}$ . This means that the superstructure is a  $(\sqrt{19} \times \sqrt{19})\text{R}23^\circ$  cell with respect to the lattice of the substrate. The lattice constant

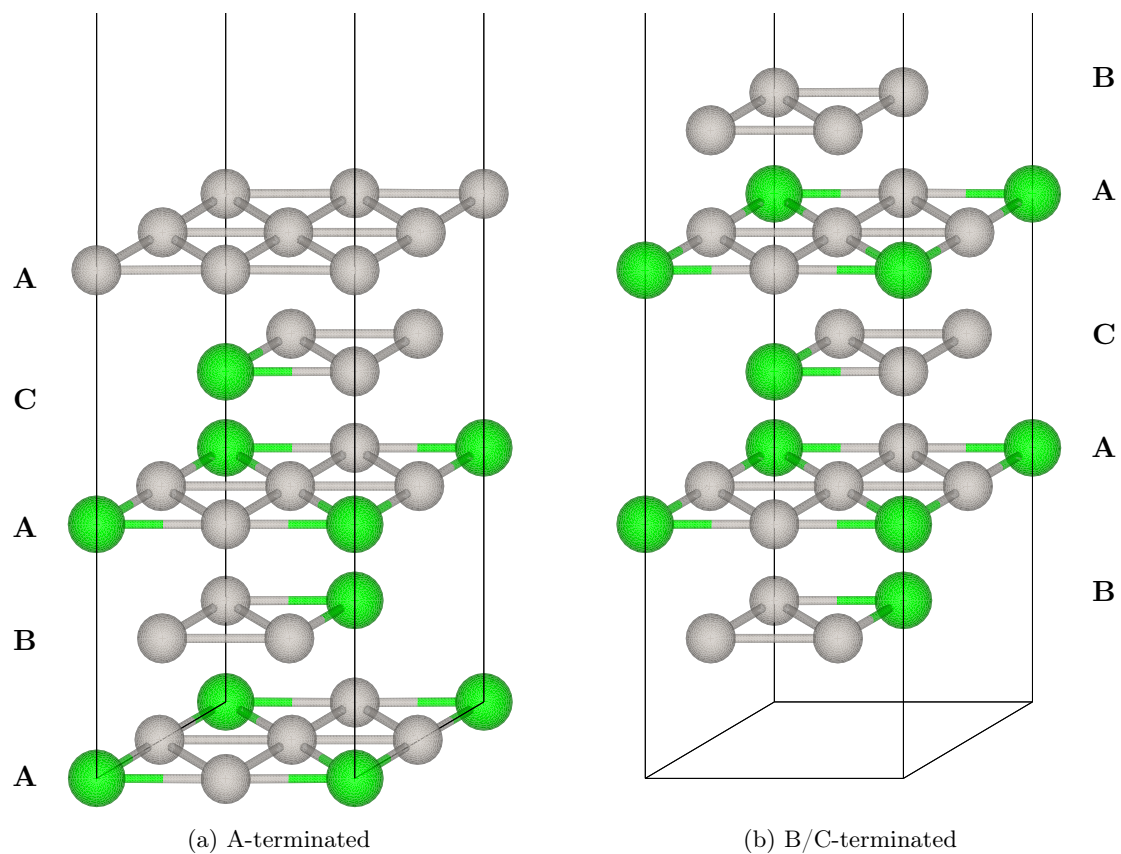
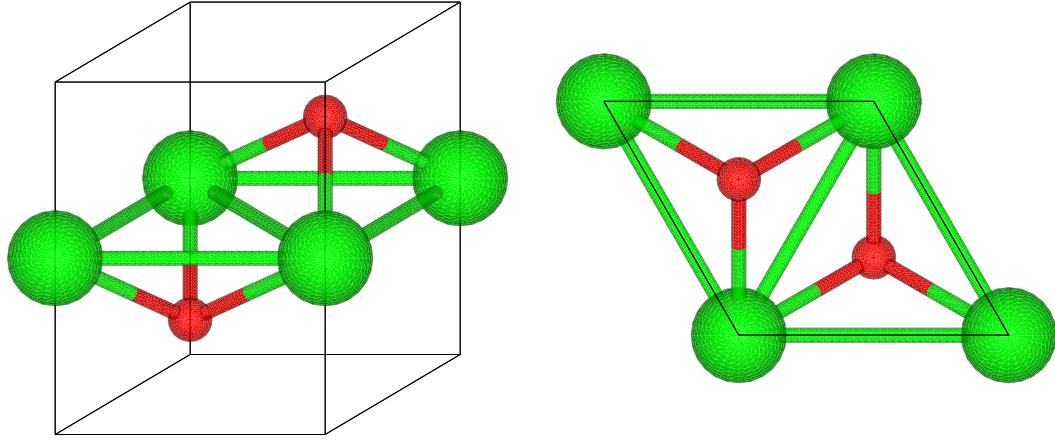


Figure 5.4.: Slabs consisting of 4 layers of  $\text{Pt}_3\text{Zr}$  and a terminating Pt layer, both in ABACA and BACAB configuration.

of the oxide film can therefore be determined by multiplying the lattice constant of the metal by the quotient of the side length of the substrate and the oxide:  $\sqrt{19}/(2\sqrt{3}) = 1.258 \times 280 = 352.24 \text{ pm}$ . The rotation angle between substrate and oxide lattice is  $30 - 23.4 = 6.6^\circ$ .

As a starting point for the construction of the  $\text{ZrO}_2$  trilayer the results from the  $\text{ZrO}_2$  bulk calculations (section 4.1.3) were used. The first step was to use a small hexagonal cell with an unsupported  $\text{ZrO}_2$  trilayer to find the optimal lattice parameters as illustrated in fig. 5.5. Similar to earlier calculations the total energy was calculated for various cell volumes while letting the internal coordinates relax. Good convergence of the energies was reached with a  $8 \times 8 \times 1$   $k$ -point grid (150 irreducible  $k$ -points) using an energy cutoff of 400 eV.

The fully relaxed unsupported film shows an equilibrium lattice constant of 330.3 pm with the Oxygen layers at a distance of 97.4 pm from the Zirconium layer. This corresponds to a contraction of 9% of the in-plane distances and an expansion perpendicular to the plane of 31% compared to cubic  $\text{ZrO}_2$  (DFT values, PBE functional in section 4.1.3: lattice parameter 363.2 pm, interlayer distances: 74.1 pm). The diagonal distance between Zr atoms was measured to be 572.0 pm which compared to the lattice constant of 572.9 pm of the  $\text{Pt}_3\text{Zr}$  slab suggested that the  $\text{ZrO}_2$  trilayer should fit on top of the substrate after a rotation by  $90^\circ$  without heavily distorting the trilayer.



(a)  $\text{ZrO}_2$  trilayer viewed from the side

(b)  $\text{ZrO}_2$  trilayer viewed from top

Figure 5.5.:  $\text{ZrO}_2$  trilayer, constructed by slicing a cubic  $\text{ZrO}_2$  cell in (111) direction.

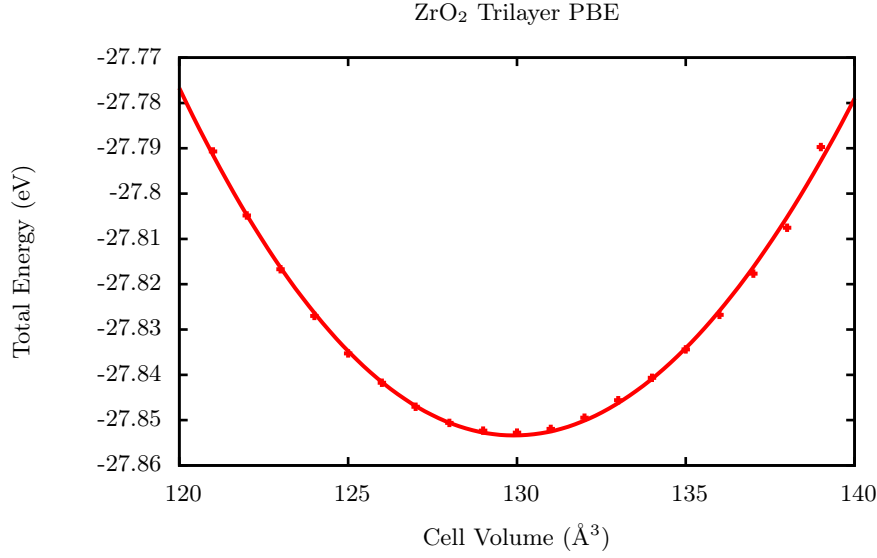


Figure 5.6.: Calculated total energies of the  $\text{ZrO}_2$  trilayer shown in fig. 5.5.

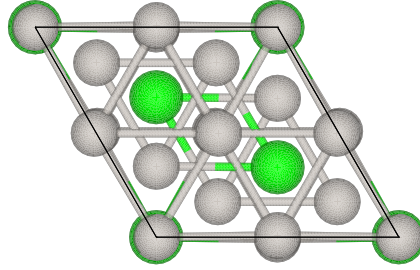
## 5.5. $\text{Pt}_3\text{Zr-ZrO}_2$ -Interface

### 5.5.1. The Model

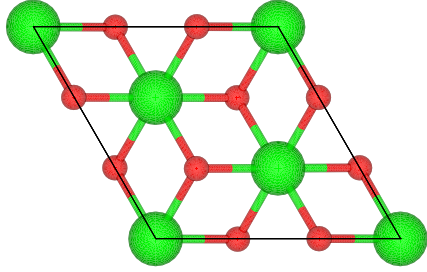
With the values for the lattice parameters gained from the calculations of the substrate and the oxide film and after a comparison with the results from the experiments mentioned above it was decided to build a simpler model to simulate the  $\text{Pt}_3\text{Zr-ZrO}_2$ -interface. Modeling the whole  $(\sqrt{19} \times \sqrt{19})\text{R}23^\circ$  superstructure would take too much computing power to do ionic relaxations due to the large number of atoms needed, so two versions of a smaller cell were constructed. Both variants consist of a single cell of Pt-terminated, 5 layers thick substrate and a 3-formula unit-sized film of oxide. Figure 5.7 shows the substrate and the two different oxide trilayer structures. The two versions of the model only differ in the horizontal position of the oxide film: in variant 1, which is called Zr/Pt, the Zirconium atom at position  $(0,0,z)$ <sup>5</sup> with respect to the lattice of the big trilayer structure is positioned on top of the Platinum atom at position  $(0,0,z)$  of the substrate lattice, while in the second version called  $\text{O}_1/\text{Pt}$  the Oxygen atom at  $(x,y,z)$  is positioned on top of the Platinum atom at position  $(0.5,0.5,z)$  of the substrate lattice. In the  $z$ -direction about  $18.9 \text{ \AA}$  vacuum was added to minimize the influence of the lower surface of substrate on the oxide film. Figure 5.8 illustrates the construction of both variants.

Even though the two variants only represent an approximation for the real structure, a comparison of the results of the calculations done with the two variants should produce a good simulation of the real crystal.

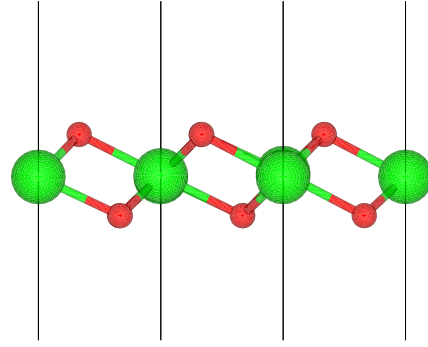
<sup>5</sup>Values are given in direct coordinates.



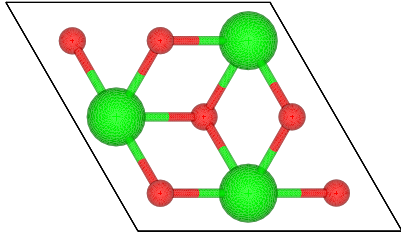
(a) Pt-terminated substrate, top view



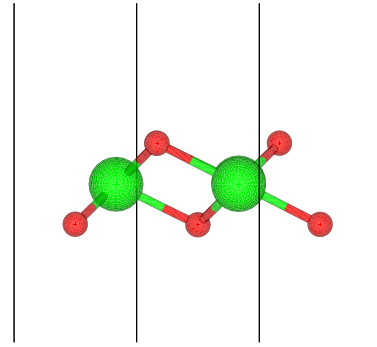
(b)  $\text{ZrO}_2$  trilayer Zr model, top view



(c)  $\text{ZrO}_2$  trilayer Zr model, side view



(d)  $\text{ZrO}_2$  trilayer  $\text{O}_1$  model, top view



(e)  $\text{ZrO}_2$  trilayer  $\text{O}_1$  model, side view

Figure 5.7.: Top and side views of the two variants of  $\text{ZrO}_2$  films. In the  $\text{O}_1$  model the  $\text{ZrO}_2$  film is shifted by  $(1/3, 1/3, 0)$  with respect to the Zr model.

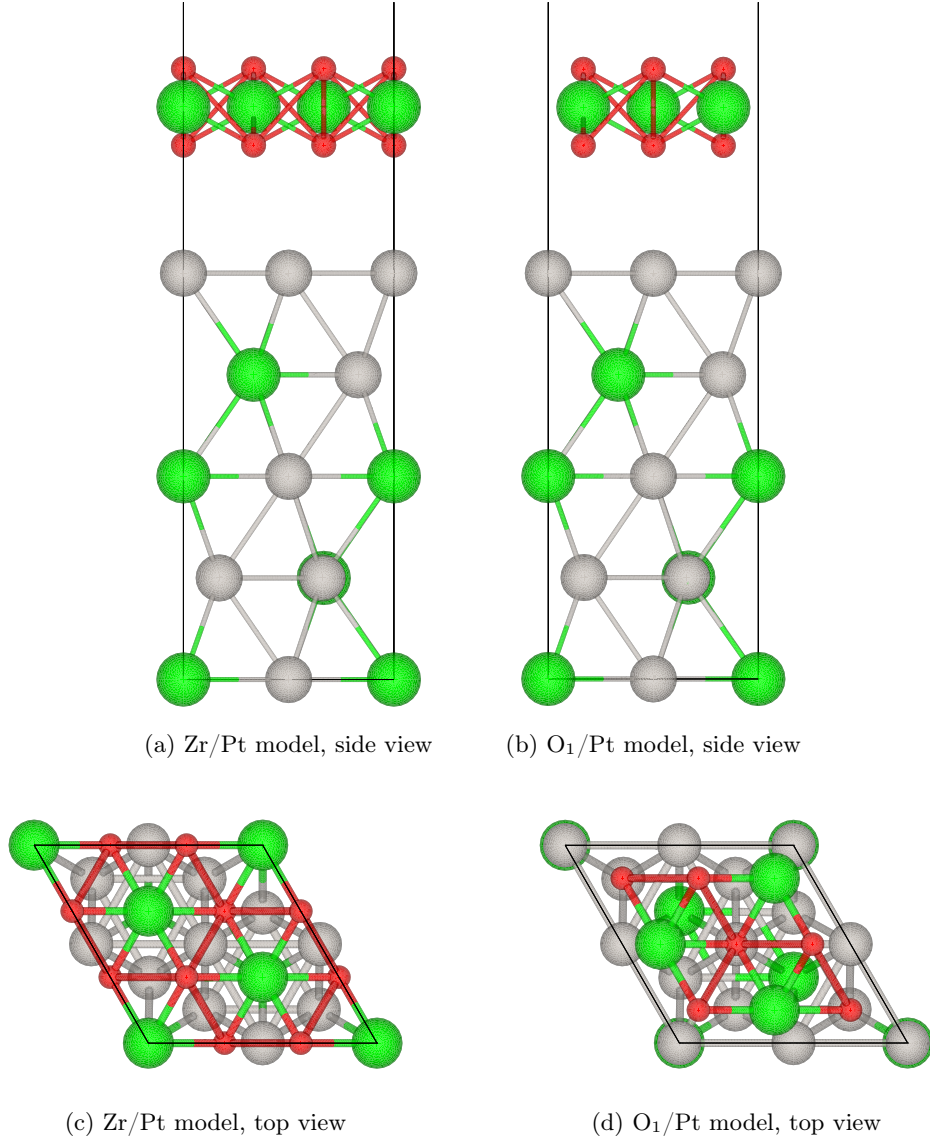


Figure 5.8.: Illustrations showing the difference of the Pt<sub>3</sub>Zr-ZrO<sub>2</sub>-interface models. In the Zr/Pt model Zr atoms of the ZrO<sub>2</sub> film sit on top of Pt atoms of the substrate, in the O<sub>1</sub>/Pt model the ZrO<sub>2</sub> film is shifted so that an O atom of the ZrO<sub>2</sub> film sits on top of a Pt atom of the substrate.

### 5.5.2. Calculations

As a first step test calculations were done to determine at which number of  $k$ -points the precision was high enough, starting with a  $4 \times 4 \times 1$   $\Gamma$ -centered grid. Good energy convergence was reached at a  $12 \times 12 \times 1$   $k$ -points grid. The energy cutoff was set to 400 eV. For the ionic relaxation calculations the cell shape was held fixed and only the ionic coordinates were allowed to relax<sup>6</sup>. As the real substrate is much thicker than the 5 layers used in the model not letting the cell shape change was used to simulate the stability and thickness of the real substrate. The next step implemented was an investigation on the optimal distance between the substrate and the oxide film by using varying starting parameters for the distance and using low precision, followed by more accurate calculations to gain a better understanding of the exact positions of the oxide atoms. Finally, properties like the densities of state and the charge distribution were investigated.

#### Distance Substrate–Oxide

To get an overview of the distance between oxide film and substrate calculations were done using a coarse-grained  $4 \times 4 \times 1$   $\Gamma$ -centered  $k$ -point grid. The energy cutoff was again set to 400 eV and only the PBE functional was used. The oxide film was moved to different distances and the ionic relaxation process was started. By comparing the equilibrium distances of these different calculations a rough estimate for the optimal distance when using the PBE functional could be obtained. For the vdW-DF these tests were only done for the Zr/Pt configuration with less test cases as the PBE results showed that the two models gave similar results for the equilibrium distance.

| start/direct coordinates | start/pm | equilibrium/pm | Energy/eV |
|--------------------------|----------|----------------|-----------|
| 5                        | 152      | 421            | −227.120  |
| 6                        | 182      | 417            | −227.117  |
| 7                        | 212      | 412            | −227.110  |
| 8                        | 242      | 422            | −227.122  |
| 9                        | 272      | 403            | −227.098  |
| 10                       | 302      | 397            | −227.086  |
| 12                       | 362      | 417            | −227.117  |
| 13                       | 392      | 431            | −227.128  |
| 14                       | 422      | 440            | −227.129  |
| 18                       | 542      | 559            | −227.120  |

Table 5.4.: Distances of the terminating platinum layer of the substrate to the lower oxygen layer of the  $\text{ZrO}_2$  film. The equilibrium values were calculated with a coarse  $4 \times 4 \times 1$   $k$ -point grid.

<sup>6</sup>VASP parameter: ISIF = 2

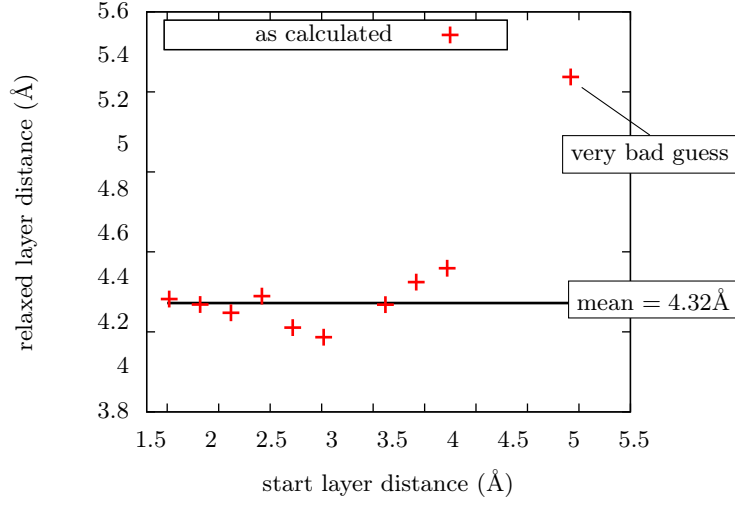


Figure 5.9.: Calculated distances of the terminating platinum layer of the substrate to the lower oxygen layer of the  $\text{ZrO}_2$  film dependent on the starting distance.

The plot shown in fig. 5.9 shows the distance between the surface Pt layer of the substrate and the lower Oxygen layer of the oxide film after relaxations from various starting values, with the lowest value at roughly 4 Å. Due to the low precision used for the calculations and the small binding energy (see table 5.6) the spread in the calculated distances is rather large. While the scatter of the obtained values does not permit an accurate prediction of the optimal distance, the results at least allowed a preliminary prediction of the distance.

Due to the low accuracy this approach was not used for the vdW-DF, there one relaxation starting from an arbitrary distance resulted in enough information to modify the model to minimize the computational cost. The initial values used for more accurate calculations can be found in table 5.5.

| Functional                      | PBE                |       | vdW-DF             |       |
|---------------------------------|--------------------|-------|--------------------|-------|
| Configuration                   | O <sub>1</sub> /Pt | Zr/Pt | O <sub>1</sub> /Pt | Zr/Pt |
| $d_{\text{O}_2-\text{Zr}}$ (pm) | 30                 | 30    | 30                 | 30    |
| $d_{\text{Zr}-\text{O}_1}$ (pm) | 30                 | 30    | 30                 | 30    |
| $d_{\text{O}_1-\text{Pt}}$ (pm) | 362                | 362   | 272                | 272   |

Table 5.5.: The initial distances used for the accurate calculations. The upper oxygen layer is named O<sub>2</sub>, the lower oxygen layer O<sub>1</sub>.



## High Precision Calculations

To determine the positions of the atoms in the slab with higher precision further calculations were done using the initial values from table 5.5. Some VASP parameters were changed: a fine  $12 \times 12 \times 1$   $k$ -points grid was used, and the electronic smearing parameter was set to a Methfessel-Paxton method of order 1<sup>7</sup>. The forces between the atoms were relaxed to a value of  $0.01 \text{ eV}/\text{\AA}$ <sup>8</sup> and the relaxation of the electronic degrees of freedom was done until a value of  $10^{-5} \text{ eV}$  was reached<sup>9</sup>. After doing one relaxation process starting from the values from table 5.5 the results were used for another round of relaxations with the precision set to “accurate”<sup>10</sup>. More information on the computing parameters can be found in appendix A.

Using the PBE functional the results show a smooth oxide film at a distance of 337 pm for the Zr/Pt and 349 pm for the O<sub>1</sub>/Pt configuration. The distance between the Oxygen layers and the Zirconium layer was measured to be 95 pm for both configurations. In the surface layer of the substrate the situation is similar to the results in chapter 5.3.2: a slight contraction of the interlayer distance of the first and second layer of 2% to 229 pm can be observed compared to the bulk interlayer distance, and slight buckling happens of 8 pm due to the lowering of the Pt atom sitting on top of a Zr atom in the third layer. Compared to typical bond lengths of about 286 pm the distance between oxide film and substrate is quite high which suggests that the adsorption of the oxide film is rather weak. This is further confirmed by the calculated adhesion energy which at  $-300 \text{ meV}$  for the Zr/Pt and  $-299 \text{ meV}$  for the O<sub>1</sub>/Pt configuration per  $\text{ZrO}_2$  formula unit (table 5.6) is rather small. The adhesion energy is calculated by subtracting the total energy of both the relaxed substrate and the oxide film from the total energy of the relaxed model. Illustrations of the different versions are shown in fig. 5.10.

Further calculations were done using the van der Waals-DFT (vdW-DF) to examine whether non-local contributions play a role in the adsorption of  $\text{ZrO}_2$  on  $\text{Pt}_3\text{Zr}$ , and to get an improved description of the physisorption. Indeed, the vdW-DF results show a much lower distance between oxide and substrate at around 250 pm which is closer to typical bond lengths of the  $\text{Pt}_3\text{Zr}$  bulk (286 pm) and a higher adhesion energy of 385 meV and 380 meV per  $\text{ZrO}_2$  formula unit for the Zr/Pt and the O<sub>1</sub>/Pt model, respectively. When letting all atoms of the O<sub>1</sub>/Pt configuration relax the oxide film moves horizontally: while the substrate atoms move for 30 pm along a vector in  $(1, 1, 0)$  direction with respect to the lattice coordinates, the oxide film moves along a  $(-1, -1, 0)$  vector until the position is similar to the Zr/Pt model. To counter this movement the O<sub>1</sub>/Pt model was modified so that both the Platinum atom in the middle of the surface layer (coordinates in direct coordinates:  $(0.5, 0.5, z)$ ) and the Oxygen atom directly above it are held in position in the  $x$  and  $y$  coordinates using VASPs selective dynamics capability. This modification resulted in a much lower adhesion energy of 338 meV per  $\text{ZrO}_2$  formula unit and a higher distance of 266 pm between oxide film and substrate.

---

<sup>7</sup>VASP parameter: ISMEAR = 1

<sup>8</sup>VASP parameter: EDIFFG = -0.01

<sup>9</sup>VASP parameter: EDIFF = 1E-5

<sup>10</sup>VASP parameter: PREC = Accurate

Compared to the results gained from the PBE calculations, strong buckling of the Zirconium layer of the oxide film of 56 pm and 71 pm for the O<sub>1</sub>/Pt and the Zr/Pt configuration can be observed. In the Zr/Pt geometry, the Zr atom directly above a Pt atom in the substrate moves down by 47 pm with respect to the middle of the upper and lower oxygen layers. The buckling leads to a distance of 293 pm of the lower Zr atom and the Pt atom directly below it, which is close to the Pt-Zr distance in the alloy (286 pm with vdW-DF, see table 5.1), while the other Zr atoms move up by 22 pm.

In the O<sub>1</sub>/Pt configuration on the other hand there is one Zr atom at a distance of 328 pm to a Pt atom of the surface, and the O atom held in place on top of a Pt atom of the surface is found at a distance of 258 pm, confirming the existence of an attractive interaction between Pt and O while still being far longer than typical Pt-O bond lengths[61]. The buckling of the Zr layer leads to a movement of one Zr atom towards the surface by 36 pm, and a movement of the upper Zr atoms away from the surface by 17 pm on average. While the oxygen layers do not show significant buckling in both configurations, oxygen atoms from the lower oxide layer move horizontally by 14 pm away from the lowered Zr atoms, and a similar movement can be observed in the upper oxygen layer. This increases the O-O distance from 331 pm to 357 pm in the triangle below the Zr atom which moves downward, and reduces the O-O distance to 312 pm in the triangle above this Zr atom. A comparison of the binding energies and the bond lengths of two models show that the oxide binds more strongly via the Zr atoms than the O atoms. In fig. 5.11 the different models calculated with vdW-DF are shown, and exact values for layer distances can be found in table 5.6.

| Functional                      | PBE                |       | vdW-DF             |       |
|---------------------------------|--------------------|-------|--------------------|-------|
| Configuration                   | O <sub>1</sub> /Pt | Zr/Pt | O <sub>1</sub> /Pt | Zr/Pt |
| $d_{\text{O}_2-\text{Zr}}$ (pm) | 95                 | 95    | 96                 | 96    |
| $d_{\text{Zr}-\text{O}_1}$ (pm) | 95                 | 95    | 95                 | 94    |
| $d_{\text{O}_1-\text{Pt}}$ (pm) | 349                | 337   | 266                | 244   |
| $b_{\text{Zr}}$ (pm)            | 2                  | 9     | 56                 | 71    |
| $b_{\text{O}_1}$ (pm)           | 0                  | 0     | 5                  | 0     |
| $b_{\text{Pt}}$ (pm)            | 8                  | 7     | 7                  | 1     |
| $E_{\text{ads}}$ (meV)          | -299               | -300  | -338               | -385  |

Table 5.6.: Interlayer distances, buckling and adsorption energies of the different models.

The distances between the atom layers is the difference between the average height of the atoms of the respective layer. The buckling is the distance between the highest and the lowest atom of each layer. The upper oxygen layer is named O<sub>2</sub>, the lower oxygen layer O<sub>1</sub>.

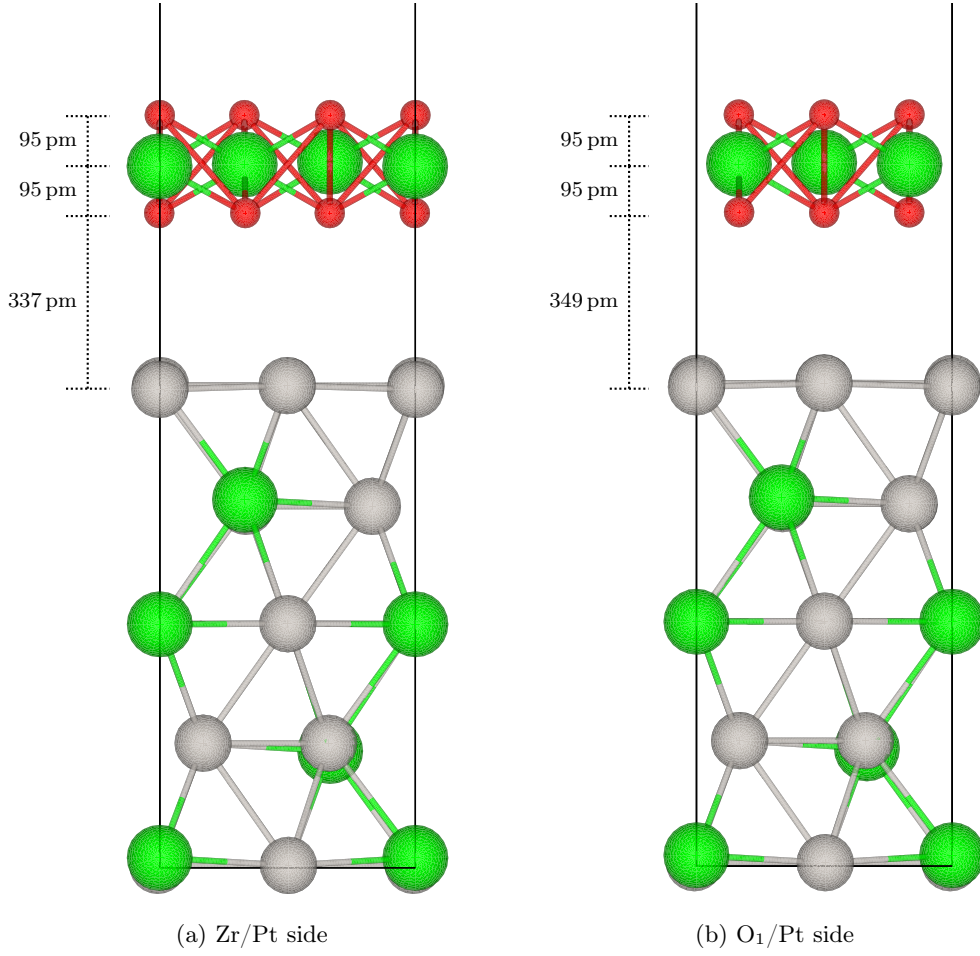


Figure 5.10.: Fully relaxed  $\text{Pt}_3\text{Zr-ZrO}_2$  structure calculated with the PBE functional.

### Work Function $\Phi$

As the average height of the Zr atoms of the oxide film does not differ from the center of the two O layers, the overall dipole moment is negligible and does not affect the work function. Nevertheless, the work function does get reduced by the adsorption of the oxide film by from 5.41 eV for the clean Pt/ $\text{Pt}_3\text{Zr}$  surface to 5.15 eV ( $\Delta\Phi = -0.26$  eV) for the PBE configuration. A similar result is given by the vdW-DF with a  $\Delta\Phi$  of  $-0.56$  eV to 4.85 eV when averaging over both configurations. An explanation for this decrease of  $\Phi$  is the compression of the wave functions above the surface of the substrate as observed by Goniakowski and Noguera [62].

To determine the work function  $\Phi$  with VASP the total local potential<sup>11</sup> in vacuum has to be calculated and the fermi energy  $E_F$  subtracted from this value. To minimize

<sup>11</sup>VASP parameters: LVTOT = .TRUE. and LVHAR = .TRUE.

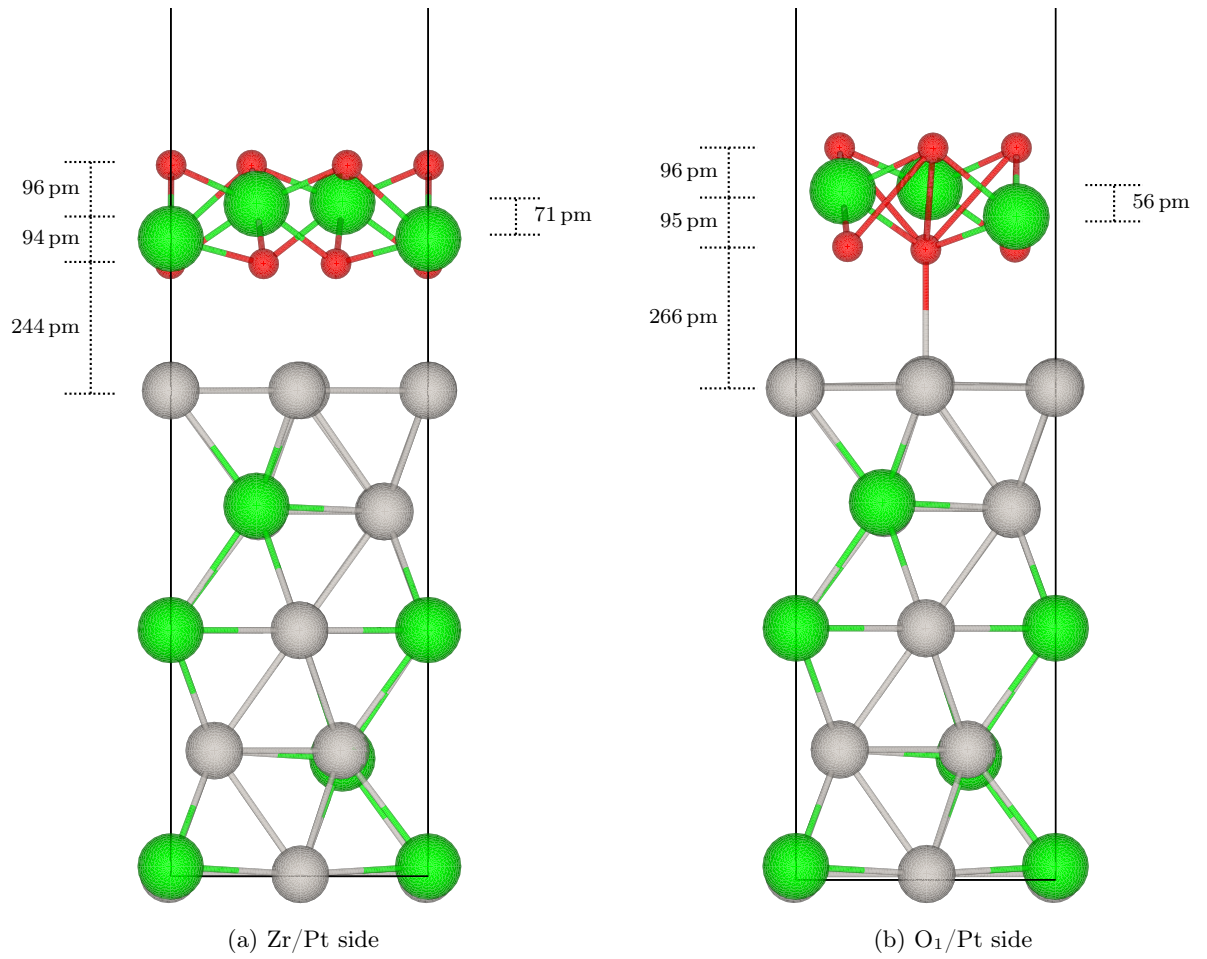


Figure 5.11.: Fully relaxed  $\text{Pt}_3\text{Zr-ZrO}_2$  structure calculated with vdW-DF. The bond between the middle lower oxygen atom and the platinum atom of the substrate in fig. 5.11b signifies that both the platinum atom and the oxygen atom are fixed in x- and y-direction during the relaxation to prevent it from relaxing into the Zr/Pt configuration.

the influence of the lower surface a slab which is symmetric to the  $z = 0$  plane was used for these calculations.

### Charge Distribution

The evaluation of the charge distribution is useful to gain knowledge of the electronic interaction between substrate and oxide film. VASP writes the total charge density after each ionic relaxation process into the CHGCAR file, which makes it easy to evaluate the charge distribution. In fig. 5.12 a comparison of the total charge density of both

| Functional | Model              | $\Phi$ /eV |
|------------|--------------------|------------|
| PBE        | O <sub>1</sub> /Pt | 5.15       |
|            | Zr/Pt              | 5.15       |
| vdW-DF     | O <sub>1</sub> /Pt | 4.84       |
|            | Zr/Pt              | 4.84       |

Table 5.7.: Work function  $\Phi$  for the two configurations O<sub>1</sub>/Pt and Zr/Pt.

structures (PBE: Zr/Pt and vdW-DF: O<sub>1</sub>/Pt) is shown. The charge densities of the substrate, the oxide film and the complete slab were calculated separately and summed in the x-y plane. The horizontal axis in fig. 5.12 corresponds to the z-coordinate of the crystal lattice, its scale indicating the z-coordinate of the fine FFT grid, and the vertical axis corresponds to the sum of the charge density in the x-y plane.

To calculate whether there is a charge transfer between the substrate and the oxide film the separately calculated total charges were summed up and compared to the total charge of the complete slab. The results indicate that the charge transfer is essentially zero, and this can also be seen in the graphs of fig. 5.12: although there is some overlap in the middle of the distance between substrate and oxide film, the charge density of the complete slab (indicated by the filled line) is not distorted compared to the sum of substrate and oxide film.

## Densities of States

It is interesting to see how the adsorption on a metal substrate influences the electronic states of the oxide compared to bulk ZrO<sub>2</sub>. For the calculation of the densities of states VASP offers the parameter LORBIT, which can be used to write the spd- and site projected wave functions to the PROCAR file. To get accurate results for the electronic structure a higher energy cutoff of 600 eV was used, and the VASP parameter NEDOS which determines the number of grid points for the densities of states was set to 1001. Additionally, the gaussian smearing method<sup>12</sup> was used to make the graphs less spiky and the precision parameter PREC was set to “Accurate”. As a first step, a static self-consistent run using these values was done, followed by a non-self-consistent run with the parameter ICHARG set to 11 using the charge densities calculated by the self-consistent run. With ICHARG = 11 the charge density is kept constant during the whole electronic minimization, because otherwise the supplied  $k$ -points would form an irregular grid and therefore would not give sensible results for the band structure. The densities of states for both models and for both the PBE and vdW-DF structure were calculated using only the PBE functional to improve comparability and to reduce possible errors induced by the vdW-DF.

As the two models (Zr/Pt and O<sub>1</sub>/Pt) are only approximations of the large ( $\sqrt{19} \times$

<sup>12</sup>VASP parameter: ISMEAR = 0

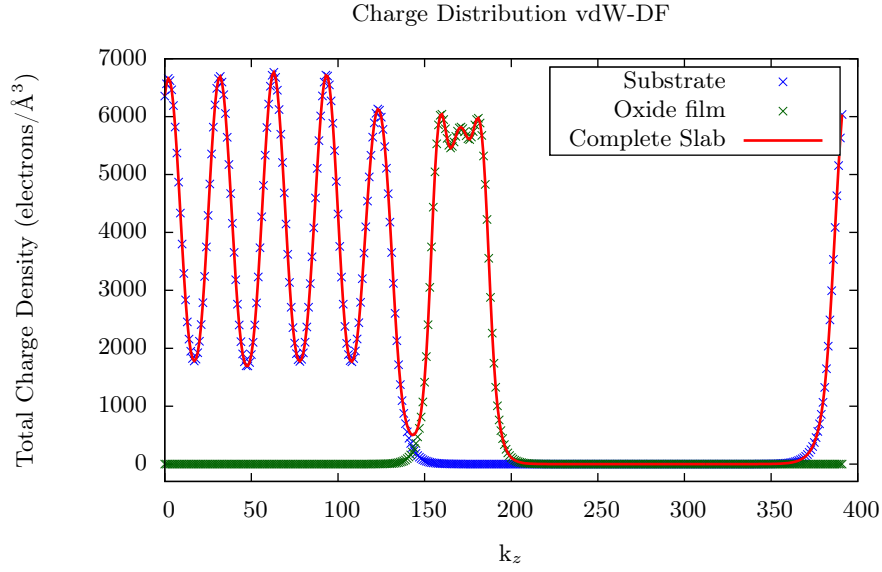
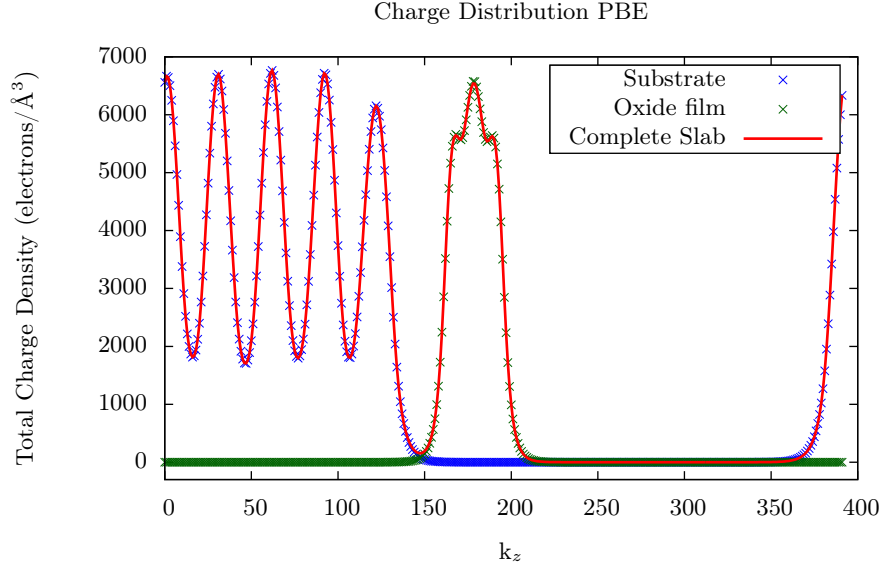


Figure 5.12.: Charge distribution of the Zr/Pt PBE calculated model compared to the O<sub>1</sub>/Pt vdW-DF calculated model.  $k_z$  corresponds to the z-coordinate of the fine FFT grid ( $\Delta_{grid} = 7.6531$  pm). The O<sub>1</sub>/Pt PBE and the Zr/Pt vdW-DF model are not shown as they do not show significant difference to the Zr/Pt PBE and the O<sub>1</sub>/Pt vdW-DF model respectively.

$\sqrt{19}$ )R23° cell the values of both models are averaged for each functional. In both configurations a band gap of about 4 eV can be observed, and while there is almost no DOS in the gap in the PBE structure slightly higher DOS can be observed for the vdW-DF configuration. It is also notable that while for the PBE configuration the upper Oxygen and lower Oxygen DOS is similar, for the vdW-DF configuration the lower and upper Oxygen density distribution differs. Here the lower oxygen densities are higher at lower energies (approx.  $-5.6$  eV) while being lower near the maximum of the upper Oxygen densities (approx.  $-3.6$  eV). Integrating over the energy range from  $-7$  eV to the fermi level at 0 eV<sup>13</sup> however shows that for both the PBE and the vdW-DF configuration the total charge of the two oxygen layers is the same. In the band gap the lower Oxygen atoms have a higher DOS than the upper ones, indicating hybridization with the metal substrate. Nevertheless, at the fermi level  $E_F$  the oxide density of states is zero. A conduction band is predicted to begin at  $\approx 1.5$  eV, which compares reasonably well with the experimental observations when taking the underestimation of band gaps when using the PBE functional into account.

## STM Simulations

By plotting the local density of states it is possible to create simulated STM images which can then be compared to experimental STM results and can help determining which atoms show as bright or dark spots. Bright spots correspond to a high local density of states (LDOS), while dark patches indicate low LDOS. The data used to create STM simulations can be gained by calculating the partial (band decomposed) charge density<sup>14</sup> in a specific energy range<sup>15</sup>.

A comparison of multiple simulated STM images at different energy ranges shows that the best results can be achieved when plotting the LDOS between the fermi level  $E_F$  and  $E_F + 0.5$  eV. The simulations for the PBE structure show bright spots at the position of the upper Oxygen atoms, while for the vdW-DF structure bright spots are shown at the position of Zirconium atoms (see figs. 5.14a and 5.14b). This result is expected, as the projected DOS (PDOS) analysis shows higher PDOS for the upper oxygen atoms in the PBE geometry, but higher PDOS for the zirconium atoms in the vdW-DF structure between  $E_F$  and  $E_F + 0.5$  eV as can be seen in fig. 5.15.

---

<sup>13</sup>VASP sets the fermi level to the highest occupied state.

<sup>14</sup>VASP parameter LPARD = .TRUE.

<sup>15</sup>VASP parameter EINT

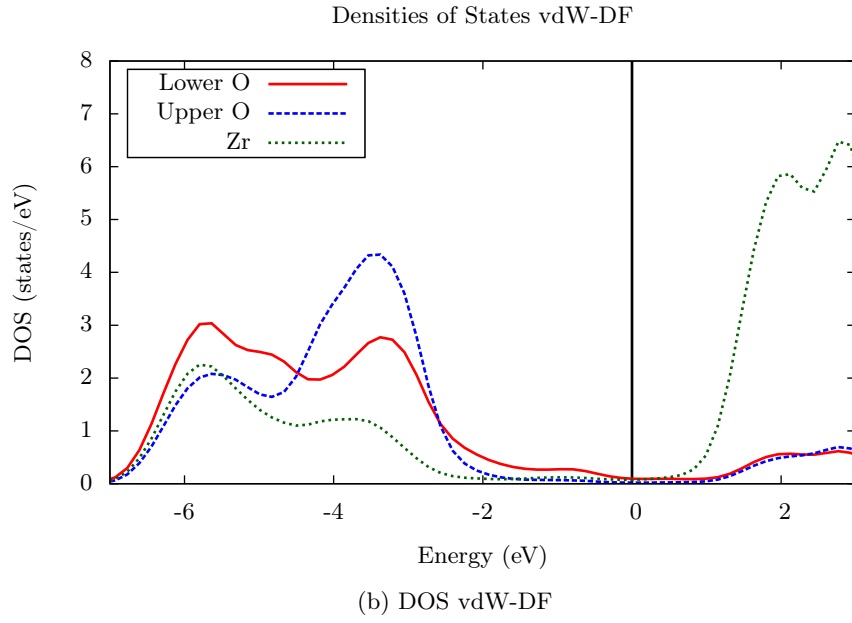
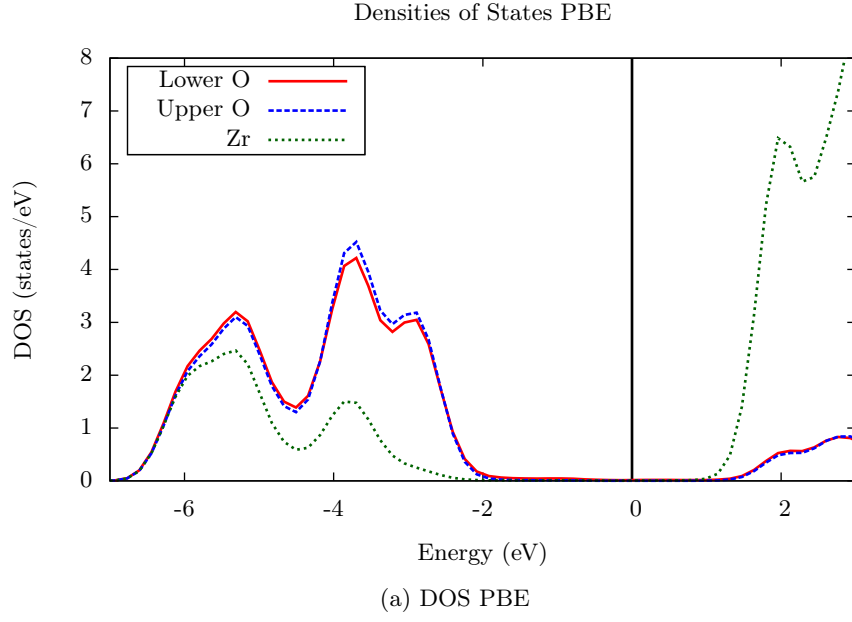
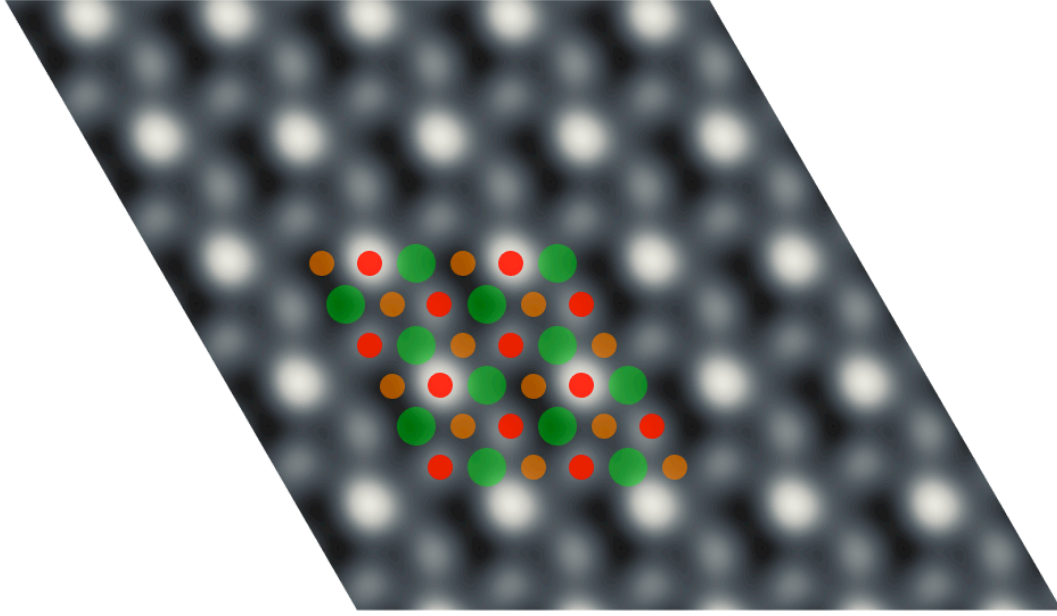
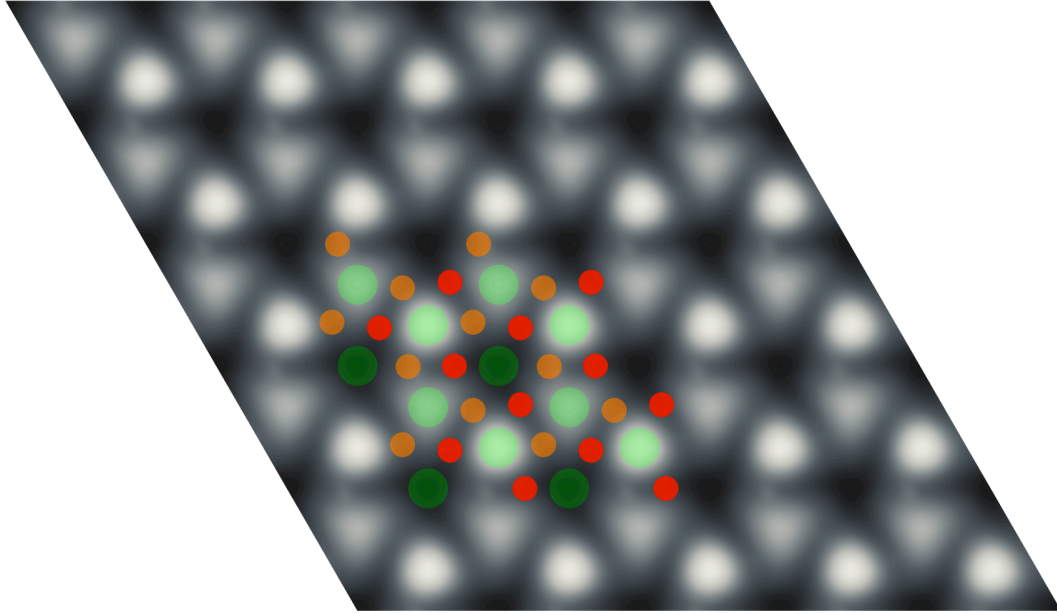


Figure 5.13.: Averaged densities of states of the PBE and the vdW-DF structure.





(a) O<sub>1</sub>/Pt PBE STM simulation



(b) Zr/Pt vdW-DF STM simulation

Figure 5.14.: STM simulations of the O<sub>1</sub>/Pt PBE model and the Zr/Pt vdW-DF model. Green circles denote zirconium atoms, red and orange circles correspond to the upper and lower oxygen atoms (also see figs. 5.10b and 5.11a). Bright spots are visible at the positions of the upper oxygen atoms in the PBE model, and at the positions of zirconium atoms for the vdW-DF model. The states between  $E_F$  and  $E_F + 0.5$  eV have been considered.

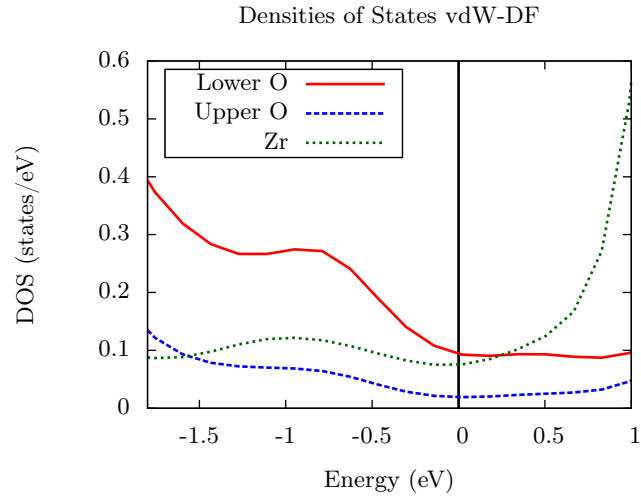
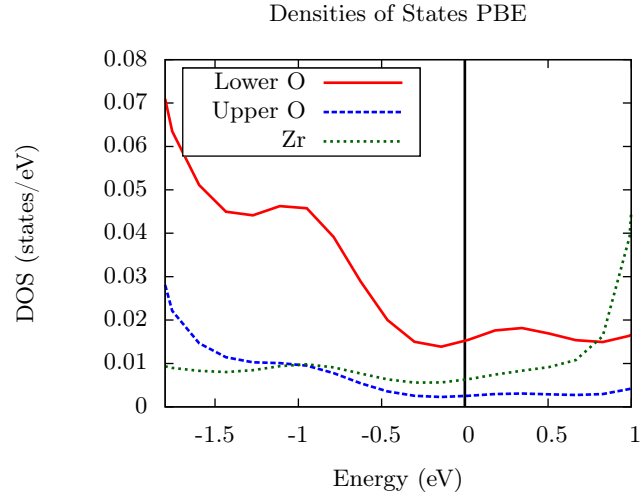


Figure 5.15.: Averaged PDOS plot, showing a small energy range around the fermi level.

## 5.6. Conclusion

First principles calculations have shown that DFT is a powerful tool which can be employed alongside experiments to gain better insight into the properties of materials. By calculating surface energies of  $\text{Pt}_3\text{Zr}$ , which is used as a substrate for ultra-thin  $\text{ZrO}_2$  films, a preferred surface termination could be established in agreement with experiments.

Calculations for the ultra-thin  $\text{ZrO}_2$  films have shown that using the PBE functional leads to quite small adsorption energies and fails to reproduce the rumpling of the surface seen in the experimental STM images. Compared to the PBE results calculations including approximations to the non-local van der Waals correlation energies lead to a much improved description of the binding of the  $\text{ZrO}_2$  film to the platinum terminated  $\text{Pt}_3\text{Zr}$  surface has been obtained. Using vdW-DF, the adsorption energies are larger and the distance between  $\text{ZrO}_2$  film and the substrate is now closer to the typical bond lengths found in the respective bulk systems. By comparing two different adsorption models of the  $\text{ZrO}_2$ - $\text{Pt}_3\text{Zr}$  interface a bonding of the  $\text{ZrO}_2$  film via the zirconium atoms could be established. Looking at the charge distribution no charge transfer happens between substrate and oxide film and furthermore the  $\text{ZrO}_2$  film does not develop a dipole moment. Finally, the simulated STM images show bright spots at the position of the Zr atoms of the oxide film.

## 5.7. Outlook

As described in section 5.5.1 the structures used for the calculations are not exact models of the real configuration, so further research needs to be done whether this abstraction plays a role in the results presented in this work. Answering this question would require the construction of the much larger  $(\sqrt{19} \times \sqrt{19})\text{R}23^\circ$  cell. Another issue which was not looked into is whether the distortion of the  $\text{ZrO}_2$  film is really caused by the addition of the van der Waals exchange energies, so the results should be compared to calculations using the LDA functional to clarify this issue.

The creation of the thin  $\text{ZrO}_2$  films by oxidation of a suitable material can work with other crystals too, for example  $\text{Pd}_3\text{Zr}$  which is easier to produce and has similar lattice parameters as  $\text{Pt}_3\text{Zr}$ . By using DFT various materials could be investigated to check the feasibility to grow zirconia films in experiments. It would also be interesting to investigate the properties of thicker oxide films in agreement with the experimental assignments.

## 6. Acknowledgements

I would like to thank my supervisors Prof. Josef Redinger and Dr. Florian Mittendorfer for giving me the chance to work on this interesting topic. They have always supported me and had time for me when I had questions. I would also like to thank my colleagues for their support, especially Dipl.Ing. Jörg Doppler, Dipl.Ing. Andreas Garhofer and Dr. Robert Hammerling, who has given me lots to read and think about covering all kind of physical problems. I also want to thank Prof. Michael Schmid and his group who have done the experiments and have given me insight into the experimental side of this field of research.

My thanks also goes to the Austrian Science Foundation FWF and the FOXSI special research program (F4511-N16) whose grant has greatly facilitated my work. This project has also enabled the use of the Vienna Scientific Cluster VSC-2 for which I am also grateful.

Finally I want to express my gratitude to my family and my friends, who have always supported me morally and of course financially, without their support I would not have been able to finish my studies.

## A. The INCAR File

The INCAR file is the central input file which controls almost all of VASP's actions. In this section a more thorough description of the VASP parameters used in this thesis will be given. The complete list of all officially supported settings can be found in the VASP Manual[63]. An example INCAR file is also given in listing A.1.

- **SYSTEM:** This parameter contains a string corresponding to the name of the system. It can be chosen freely and is useful to identify a system as it is also written into the central output file OUTCAR.
- **ENCUT:** Sets the cutoff energy of the plane wave basis set in eV, so all plane waves with a kinetic energy lower than this value are included in the basis set. The default value is the highest ENMAX value found in the POTCAR file.
- **ENAUG:** Sets the kinetic cutoff energy for the augmentation charges. It is used to calculate the number of the fine FFT grid points where the localized augmentation charges are represented. Similar to the ENCUT parameter the default value is the highest value of the parameter EAUG in the POTCAR file.
- **ISMEAR:** This parameter determines the setting of the partial occupancies for each orbital. For DOS calculations and accurate total energy calculations of metals a value of  $-5$  is recommended, which corresponds to a tetrahedron method with Blöchl corrections. Setting this parameter to 0 compels VASP to apply Gaussian smearing which leads to reasonable results in most cases. For metallic systems though it is recommended to use the method of Methfessel-Paxton[64] of order 1 ( $ISMEAR = 1$ ).
- **IBRION:** This parameter determines how the ions are moved during ionic relaxations into a local energy minimum. By setting this value to 2 VASP uses a conjugate-gradient algorithm[65] to relax the ions into their ground state. This setting is recommended for difficult relaxation problems as this algorithm has good backup routines. A quasi-Newton algorithm (RMM-DIIS[66]) which is very fast and efficient is activated by setting IBRION to 1, but it does need good initial positions for the ions.
- **ISIF:** This tag controls the calculation of the stress tensor and which degrees of freedom can be varied during the ionic relaxation process. Setting this parameter to 2 allows the relaxation of ions in the cell while keeping the cell volume and shape fixated. A value of 4 allows relaxation of ions and simultaneous change of the cell shape. Other combinations of changing cell shape, volume and ions can also be calculated.
- **NSW:** Controls the maximum number of ionic relaxation steps.
- **EDIFFG:** This parameter defines the break condition for the ionic relaxation loop.

If the value is positive the relaxation will be stopped if the total energy between two steps is smaller than this value. By setting EDIFFG to a negative value the relaxation will stop if all forces between ions is smaller than  $|\text{EDIFFG}|$ .

- EDIFF: Specifies the break condition for the electronic self-consistent loop. As soon as the total energy change and the band structure energy change are both smaller than this value.
- LREAL: For big systems with more than 20 atoms it is recommended to evaluate the projection operators in real space, which can be achieved by setting this parameter to “Auto” or “On”.
- NPAR: On massively parallel systems it is useful to distribute the electronic bands efficiently over the different computing nodes. Per default all cores work on the calculation on all bands by distributing the plane wave coefficients over all cores. The parameter NPAR can now be used to determine how many cores work on one orbital; it is recommended to set it to  $\text{NPAR} \approx \sqrt{\text{number of cores}}$ .
- PREC: This parameter controls the default value for different parameters like ENCUT, the FFT grid size and the number of grid points when LREAL = Auto. A value “high” for example increases the default energy cutoff to  $\text{MAX}(\text{ENCUT}) \cdot 1.3$ .
- LORBIT: This parameter controls whether the spd- or site-projected densities of states are written to the DOSCAR file.
- LVTOT: Enabling this setting enables VASP to write the total local potential to the LOCPOT file. The default setting is to write the entire local potential including the exchange correlation potential. If the additional parameter LVHAR is set only the ionic and the Hartree potential are output to the LOCPOT file.

```

1  SYSTEM = Pt3Zr Slab, ZrO2 Trilayer
2
3  ENCUT  = 400.00 eV
4  ENAUG  = 350.00 eV
5
6  ISMEAR = -5
7
8  IBRION = 2
9  ISIF   = 2
10 NSW   = 200
11
12 EDIFFG = -0.01
13 EDIFF  = 1E-5
14
15 LREAL  = Auto
16 NPAR   = 8

```

Listing A.1: Sample INCAR file.

## B. CONTCARS

In this section the fully relaxed structure files are documented. The format of these files follows the standard VASP POSCAR/CONTCAR regime. The value in the second line is a multiplication factor. The coordinates of the cell which are written in lines 3–5 are multiplied with this factor. Lines 6 and 7 define the atom types and the number of atoms of each kind. The value line 8 defines how the coordinates of the atoms can be entered, it can be either “direct” or “cartesian”<sup>1</sup>. To enable selective dynamics the value “selective” needs to be entered in line 8, with all following lines shifted down. By enabling this feature one can fixate the coordinates of each atom during the ionic relaxation process. An example is given in listing B.4. Starting at the 8th line (or 9th if selective dynamics is enabled) the coordinates of each atom has to be entered with the elements following the number and type given in lines 6 and 7. If selective dynamics is enabled a “T” or “F” (True or False) for each coordinate follows the atomic coordinate to signify which coordinate is fixated (“F”) and which is not (“T”).

### B.1. Pt<sub>3</sub>Zr-ZrO<sub>2</sub>-Interface

```
1  ZrO2 on Pt3Zr Zr/Pt config, PBE
2  1.0000000000000000
3  5.7288565945186711 0.0000739554729630 0.0000000000000000
4  -2.8643642498900639 4.9613723232590345 0.0000000000000000
5  0.0000000000000000 0.0000000000000000 30.0000000000000000
6  Zr Pt O
7  7 16 6
8  Direct
9  0.0008475603290505 0.9998370080927663 0.0065189717324486
10 0.3339896796937819 0.6665866010089313 0.0756118635182501
11 0.0001921361849796 0.0000153289341786 0.1575867484183123
12 0.6662708707630585 0.3332891578323915 0.2381673968178486
13 0.3319526075543217 0.6656903826405887 0.4568350292730933
14 0.6653175045850667 0.3323541009720226 0.4550771409196915
15 0.9986216692999431 0.9990142111471977 0.4539152206917992
16 0.9989655086204701 0.9999025173864416 0.3095134311199402
17 0.4970359776418256 0.5036693769813819 0.0016433174710637
18 0.4969516087958878 0.9921023293400447 0.0016363209684917
19 0.0085454096888295 0.5036327924598943 0.0016390747459185
20 0.8312939086087550 0.6611382271039813 0.0806135393742806
21 0.8312213908003779 0.1692847912839432 0.0806138186112875
22 0.3395123532620342 0.1693904696497252 0.0806167889492373
23 0.4994145230090556 0.5009837876158344 0.1579492205100337
```

<sup>1</sup>Only the first character is read by VASP, so entering “d” or “c” is sufficient.

|    |                    |                    |                    |
|----|--------------------|--------------------|--------------------|
| 24 | 0.4991674322887422 | 0.9982493575118931 | 0.1579565568201797 |
| 25 | 0.0018728407263041 | 0.5007236290712418 | 0.1579628108856364 |
| 26 | 0.1683230087040206 | 0.3365854279616235 | 0.2339029508182041 |
| 27 | 0.6631888332570819 | 0.8319999667973959 | 0.2338907045595409 |
| 28 | 0.1677023290349890 | 0.8313736313908608 | 0.2339011864447047 |
| 29 | 0.5015163697781383 | 0.4991889791686339 | 0.3119972437350055 |
| 30 | 0.4998628489420880 | 0.0030274265804785 | 0.3119787950221321 |
| 31 | 0.9961668145406537 | 0.4976275799243349 | 0.3119773242967898 |
| 32 | 0.3328574049935040 | 0.9978089484563061 | 0.4236941290744776 |
| 33 | 0.6670201326244682 | 0.0000172378776780 | 0.4870008876607356 |
| 34 | 0.9998407223788897 | 0.3344414057210533 | 0.4236852385512854 |
| 35 | 0.9977158301876636 | 0.6664121784462974 | 0.4869998641888114 |
| 36 | 0.6633267975986916 | 0.6649115462330673 | 0.4236872804080130 |
| 37 | 0.3313060461073323 | 0.3307420204097991 | 0.4869834804127774 |

Listing B.1: Zr/Pt PBE

|    |                                 |                     |                     |
|----|---------------------------------|---------------------|---------------------|
| 1  | ZrO2 on Pt3Zr 01/Pt config, PBE |                     |                     |
| 2  | 1.0000000000000000              |                     |                     |
| 3  | 5.7288565945186711              | 0.0000739554729630  | 0.0000000000000000  |
| 4  | -2.8643642498900639             | 4.9613723232590345  | 0.0000000000000000  |
| 5  | 0.0000000000000000              | 0.0000000000000000  | 30.0000000000000000 |
| 6  | Zr                              | Pt                  | O                   |
| 7  | 7                               | 16                  | 6                   |
| 8  | Direct                          |                     |                     |
| 9  | 0.9994844489681843              | 0.0003763223523976  | 0.0052954040387640  |
| 10 | 0.3322651304795320              | 0.6665982164717775  | 0.0744795738895700  |
| 11 | -0.0011682267835733             | -0.0004912641833119 | 0.1563227760078588  |
| 12 | 0.6652690925224860              | 0.3325068030383952  | 0.2369213573440752  |
| 13 | 0.1677890775513590              | 0.4996359126916705  | 0.4584846614635132  |
| 14 | 0.5012040571766680              | 0.1663471780555903  | 0.4577925427965153  |
| 15 | 0.8345520379418865              | 0.8330870933105133  | 0.4576808292363347  |
| 16 | 0.9992659924352567              | 0.9993525659474838  | 0.3083257172269268  |
| 17 | 0.4953416205931568              | 0.5041417350093598  | 0.0004899725204377  |
| 18 | 0.4952622328075906              | 0.9924231538121311  | 0.0005042333514609  |
| 19 | 0.0067901335589852              | 0.5039910761438552  | 0.0004945198231726  |
| 20 | 0.8296490722403489              | 0.6611717780370722  | 0.0793994647872984  |
| 21 | 0.8296226451158027              | 0.1692656187465280  | 0.0793961137924742  |
| 22 | 0.3379248100620264              | 0.1694025202272132  | 0.0794058912407170  |
| 23 | 0.4979021963384868              | 0.5003488337693355  | 0.1567287587762203  |
| 24 | 0.4979012027985616              | 0.9976240398730359  | 0.1567387241456813  |
| 25 | 0.0003754190811473              | 0.5001328368645402  | 0.1567478097307872  |
| 26 | 0.1673017940373109              | 0.3358625939758171  | 0.2326912642316906  |
| 27 | 0.6624804278962747              | 0.8309193150773272  | 0.2326858647300507  |
| 28 | 0.1668762700092982              | 0.8311779802528194  | 0.2326036053645377  |
| 29 | 0.5006245954292006              | 0.4978096698218133  | 0.3108728237169745  |
| 30 | 0.5005144776232087              | 0.0023227427846746  | 0.3106536401965862  |
| 31 | 0.9957698555022010              | 0.4978560472203108  | 0.3106243072649040  |
| 32 | 0.1680179838447095              | 0.8323657674383588  | 0.4263872084246255  |
| 33 | 0.5015436866686217              | 0.8332680779554694  | 0.4897212951569423  |
| 34 | 0.8348850196503931              | 0.1667447298425691  | 0.4264778212882714  |
| 35 | 0.8338292592940231              | 0.4997339376951636  | 0.4896966565536702  |
| 36 | 0.5005868462082019              | 0.4999572605170373  | 0.4262367245137032  |
| 37 | 0.1681388709486693              | 0.1660674872510786  | 0.4896967743862405  |



Listing B.2: O<sub>1</sub>/Pt PBE

```

1  ZrO2 on Pt3Zr Zr/Pt config, vdW-DF
2  1.0000000000000000
3      5.7288565945186711      0.0000739554729630      0.0000000000000000
4      -2.8643642498900639      4.9613723232590345      0.0000000000000000
5      0.0000000000000000      0.0000000000000000      30.0000000000000000
6      Zr      Pt      O
7      7      16      6
8  Direct
9      0.9991411673593150      0.9995605644879251      0.0062640903195769
10     0.3325879800260963      0.6661813508852441      0.0756413335128794
11     0.9993546088402320      0.9994252221637573      0.1581373702482466
12     0.6662769483525759      0.3327595307815683      0.2379781645035095
13     0.3335277350732618      0.6667390885943566      0.4331430159152979
14     0.6668576233321428      0.3334040552687632      0.4319033399897588
15     0.0001946925684715      0.0000577405217049      0.4095154757182253
16     0.9998218492410792      0.9994928765059078      0.3118538870309471
17     0.4954169487933796      0.5030528177552844      0.0012896000263155
18     0.4956056972370234      0.9923448104211225      0.0012975701584574
19     0.0062654601687291      0.5032394273728933      0.0013055853991077
20     0.8299892754264395      0.6608723737167386      0.0806591123123856
21     0.8298467447123686      0.1687470809184131      0.0806553597630143
22     0.3378480752554624      0.1688992076475921      0.0806526959993825
23     0.4996077937084073      0.5008546750416268      0.1579174795266028
24     0.4978918486294778      0.9981546094220265      0.1579040286206535
25     0.0006081106358378      0.4991890239800415      0.1579128175232426
26     0.1728062565090196      0.3401897239568533      0.2342810062865611
27     0.6587289392132718      0.8318919929093486      0.2342785529727308
28     0.1670841207545654      0.8261973715831276      0.2342744816987956
29     0.5086988184858166      0.5073358232741432      0.3120833245767586
30     0.4919775522580315      0.0004637270279134      0.3120850718147603
31     0.9987932573480897      0.4906205745271101      0.3120863270404018
32     0.3585080450418204      0.9977708832945584      0.3934106393968041
33     0.6862921784985958      0.0013306120522132      0.4567342317910386
34     0.0024346814018959      0.3606449783098664      0.3934079886847396
35     0.9989270044656485      0.6849170197532847      0.4567339233978850
36     0.6396077034464861      0.6417496786643818      0.3934232062917062
37     0.3152990032164850      0.3139135771622341      0.4567266554802019

```

Listing B.3: Zr/Pt vdW-DF

```

1  ZrO2 on Pt3Zr O1/Pt config, vdW-DF
2  1.0000000000000000
3      5.7288565945186711      0.0000739554729630      0.0000000000000000
4      -2.8643642498900639      4.9613723232590345      0.0000000000000000
5      0.0000000000000000      0.0000000000000000      30.0000000000000000
6      Zr      Pt      O
7      7      16      6
8  Selective dynamics
9  Direct
10     -0.0012614421552791 -0.0008163172277703      0.0086272803623828      T      T      T

```

|    |                     |                     |                    |   |   |   |
|----|---------------------|---------------------|--------------------|---|---|---|
| 11 | 0.3321564856396957  | 0.6657512063558595  | 0.0780691847592036 | T | T | T |
| 12 | -0.0009667261969941 | -0.0002152186748188 | 0.1603701785436534 | T | T | T |
| 13 | 0.6658285802363249  | 0.3317395855775101  | 0.2406110222499074 | T | T | T |
| 14 | 0.1854924066372216  | 0.5142462267679900  | 0.4415464524976996 | T | T | T |
| 15 | 0.5196927222004852  | 0.1798959499693791  | 0.4389947086345888 | T | T | T |
| 16 | 0.8540325968875938  | 0.8483968025710987  | 0.4227469119114667 | T | T | T |
| 17 | -0.0073147418696367 | -0.0052908714432958 | 0.3134068649105496 | T | T | T |
| 18 | 0.4950094712759728  | 0.5027777668260905  | 0.0036957055573614 | T | T | T |
| 19 | 0.4951905119361487  | -0.0078706381800591 | 0.0037409087712957 | T | T | T |
| 20 | 0.0057725084751030  | 0.5028278872327959  | 0.0037482376140663 | T | T | T |
| 21 | 0.8295236129478298  | 0.6606434828568525  | 0.0830527562269842 | T | T | T |
| 22 | 0.8292680741473143  | 0.1686541070813134  | 0.0830112253153984 | T | T | T |
| 23 | 0.3373605816945349  | 0.1682662581493573  | 0.0830627193988333 | T | T | T |
| 24 | 0.4982583122250460  | 0.5000543611018388  | 0.1602934073371573 | T | T | T |
| 25 | 0.4986603904811781  | -0.0025326251506061 | 0.1604774682986911 | T | T | T |
| 26 | 0.0008485308556861  | 0.4996840129950113  | 0.1604010756176169 | T | T | T |
| 27 | 0.1719966816038481  | 0.3400676026309202  | 0.2369343545935335 | T | T | T |
| 28 | 0.6607985925824453  | 0.8290451964327300  | 0.2367581859645116 | T | T | T |
| 29 | 0.1668182975965455  | 0.8311860292066742  | 0.2362733102959583 | T | T | T |
| 30 | 0.5000000000000000  | 0.5000000000000000  | 0.3157702851390790 | F | F | T |
| 31 | 0.4927433359668728  | -0.0002045256199232 | 0.3142829533591343 | T | T | T |
| 32 | -0.0055051291068217 | 0.4945426975264323  | 0.3141191696303202 | T | T | T |
| 33 | 0.2012596769530004  | 0.8440259158290415  | 0.4033003740881627 | T | T | T |
| 34 | 0.5345173034153631  | 0.8488356057738260  | 0.4666070325327869 | T | T | T |
| 35 | 0.8562694240133001  | 0.1985224472848969  | 0.4035952567297061 | T | T | T |
| 36 | 0.8494880841606971  | 0.5276114218971010  | 0.4664659194252846 | T | T | T |
| 37 | 0.5000000000000000  | 0.5000000000000000  | 0.4017984182425112 | F | F | T |
| 38 | 0.1757529030199748  | 0.1678191651504196  | 0.4666285277692497 | T | T | T |

Listing B.4: O<sub>1</sub>/Pt vdW-DF

## C. Additional Tables

| Volume<br>per f.u./Å <sup>3</sup> | Energy per f.u./eV<br>Mono | LDA functional |         |         |          |
|-----------------------------------|----------------------------|----------------|---------|---------|----------|
|                                   |                            | Tetra          | Cubic   | Ortho-I | Ortho-II |
| 25                                | −29.320                    | −28.754        | −28.754 | −29.400 | −30.133  |
| 26                                | −29.755                    | −29.431        | −29.432 | −29.831 | −30.507  |
| 27                                | −30.073                    | −29.953        | −29.957 |         | −30.764  |
| 28                                | −30.343                    | −30.348        | −30.348 | −30.413 | −30.925  |
| 29                                | −30.580                    | −30.637        | −30.638 | −30.647 | −31.002  |
| 30                                | −30.761                    | −30.836        | −30.837 | −30.830 | −31.014  |
| 30.5                              |                            |                |         | −30.905 |          |
| 31                                | −30.900                    | −30.967        | −30.959 | −30.967 | −30.974  |
| 31.5                              |                            |                |         | −31.016 |          |
| 32                                | −31.002                    | −31.037        | −31.012 | −31.053 | −30.890  |
| 32.5                              |                            |                |         | −31.078 |          |
| 33                                | −31.069                    | −31.062        | −31.014 | −31.092 | −30.777  |
| 34                                | −31.101                    | −31.047        | −30.967 | −31.087 | −30.647  |
| 35                                | −31.113                    | −31.000        | −30.880 | −31.043 | −30.520  |
| 36                                | −31.090                    | −30.926        | −30.760 | −30.964 | −30.397  |
| 37                                | −31.035                    | −30.830        | −30.609 |         | −30.281  |
| 37.5                              |                            |                |         | −30.794 |          |
| 38                                | −30.953                    | −30.716        | −30.436 |         | −30.175  |
| 38.5                              |                            |                |         | −30.667 |          |
| 39                                | −30.856                    | −30.588        | −30.234 |         | −30.095  |
| 39.5                              |                            |                |         | −30.540 |          |
| 40                                | −30.794                    | −30.454        | −30.020 |         | −29.826  |
| 41                                | −30.757                    | −30.314        | −29.790 |         | −29.744  |
| 42                                | −30.721                    | −30.171        | −29.549 |         | −29.674  |
| 43                                | −30.683                    | −30.027        | −29.298 |         | −29.593  |
| 44                                | −30.638                    | −29.881        | −29.038 |         | −29.501  |
| 45                                | −30.578                    | −29.736        | −28.771 |         | −29.413  |

Table C.1.: Calculated energies, LDA.

| Volume<br>per f.u./Å <sup>3</sup> | Energy per f.u./eV<br>Mono | PBE functional |         |         |          |
|-----------------------------------|----------------------------|----------------|---------|---------|----------|
|                                   |                            | Tetra          | Cubic   | Ortho-I | Ortho-II |
| 25                                | -25.560                    | -25.250        | -25.251 |         | -30.133  |
| 26                                | -26.489                    | -26.049        | -26.050 |         | -30.507  |
| 27                                | -26.916                    | -26.684        | -26.689 |         | -30.764  |
| 28                                | -27.255                    | -27.185        | -27.186 |         | -30.925  |
| 29                                | -27.583                    | -27.576        | -27.578 |         | -31.002  |
| 30                                | -27.844                    | -27.872        | -27.873 | -27.913 | -31.014  |
| 31                                | -28.053                    | -28.093        | -28.087 | -28.127 | -30.974  |
| 32                                | -28.219                    | -28.248        | -28.225 | -28.289 | -30.890  |
| 32.5                              |                            |                |         | -28.347 |          |
| 33                                | -28.347                    | -28.353        | -28.310 | -28.397 | -30.777  |
| 33.5                              |                            |                |         | -28.436 |          |
| 34                                | -28.442                    | -28.345        | -28.342 | -28.464 | -30.647  |
| 34.5                              |                            |                |         | -28.482 |          |
| 35                                | -28.502                    | -28.440        | -28.330 | -28.490 | -30.520  |
| 35.5                              |                            |                |         | -28.488 |          |
| 36                                | -28.541                    | -28.435        | -28.282 | -28.478 | -30.397  |
| 36.5                              |                            |                |         | -28.459 |          |
| 37                                | -28.549                    | -28.404        | -28.200 | -28.433 | -30.281  |
| 37.5                              |                            |                |         | -28.400 |          |
| 38                                | -28.528                    | -28.350        | -28.092 | -28.362 | -30.175  |
| 39                                | -28.483                    | -28.280        | -27.952 | -28.272 | -30.095  |
| 40                                | -28.426                    | -28.199        | -27.798 | -28.195 | -29.826  |
| 41                                | -28.405                    | -28.109        | -27.626 | -28.041 | -29.744  |
| 42                                | -28.390                    | -28.011        | -27.440 |         | -29.674  |
| 43                                | -28.372                    | -27.910        | -27.242 |         | -29.593  |
| 44                                | -28.354                    | -27.805        | -27.033 |         | -29.501  |
| 45                                | -28.330                    | -27.699        | -26.817 |         | -29.413  |

Table C.2.: Calculated energies, PBE.

| Volume<br>per f.u./Å <sup>3</sup> | Energy per f.u./eV<br>Mono | PBEsol functional |         |         |          |
|-----------------------------------|----------------------------|-------------------|---------|---------|----------|
|                                   |                            | Tetra             | Cubic   | Ortho-I | Ortho-II |
| 25                                |                            |                   |         | -28.710 | -29.443  |
| 26                                |                            |                   |         | -29.183 | -29.861  |
| 27                                |                            |                   |         |         | -30.159  |
| 28                                |                            |                   | -29.720 | -29.823 | -30.359  |
| 29                                |                            |                   | -30.049 | -30.090 | -30.473  |
| 30                                |                            | -30.283           | -30.282 | -30.301 | -30.521  |
| 31                                |                            | -30.443           | -30.441 | -30.467 | -30.514  |
| 32                                | -30.524                    | -30.551           | -30.526 | -30.582 | -30.463  |
| 33                                | -30.613                    | -30.607           | -30.559 | -30.646 | -30.380  |
| 34                                | -30.671                    | -30.625           | -30.546 | -30.669 | -30.275  |
| 35                                | -30.700                    | -30.608           | -30.489 | -30.652 | -30.169  |
| 36                                | -30.700                    | -30.561           | -30.397 | -30.600 |          |
| 37                                | -30.672                    | -30.493           | -30.276 | -30.518 |          |
| 38                                | -30.614                    | -30.411           | -30.126 | -30.412 |          |
| 39                                | -30.538                    | -30.312           |         | -30.289 |          |
| 40                                | -30.481                    | -30.197           |         | -30.099 |          |
| 41                                | -30.454                    |                   |         | -29.937 |          |
| 42                                | -30.423                    |                   |         | -29.801 |          |
| 43                                |                            |                   |         | -29.663 |          |
| 44                                |                            |                   |         | -29.384 |          |
| 45                                |                            |                   |         | -29.190 |          |

Table C.3.: Calculated energies, PBEsol.

| Volume<br>per f.u./Å <sup>3</sup> | Energy per f.u./eV<br>Mono | HSE functional |         |         |          |
|-----------------------------------|----------------------------|----------------|---------|---------|----------|
|                                   |                            | Tetra          | Cubic   | Ortho-I | Ortho-II |
| 28                                |                            |                | -36.472 |         |          |
| 29                                |                            |                | -36.823 | -36.861 | -37.195  |
| 29.5                              |                            |                |         |         | -37.233  |
| 30                                |                            | -37.077        | -37.077 | -37.090 | -37.256  |
| 30.5                              |                            |                |         |         | -37.264  |
| 31                                |                            | -37.255        | -37.249 | -37.274 | -37.260  |
| 31.5                              |                            |                |         |         | -37.241  |
| 32                                | -37.348                    | -37.369        | -37.347 | -37.406 | -37.218  |
| 32.5                              |                            |                |         | -37.452 | -37.188  |
| 33                                | -37.442                    | -37.436        | -37.390 | -37.482 |          |
| 33.5                              |                            |                |         | -37.505 |          |
| 34                                | -37.509                    | -37.462        | -37.381 | -37.516 |          |
| 34.5                              |                            |                |         | -37.516 |          |
| 35                                | -37.546                    | -37.452        | -37.328 | -37.507 |          |
| 35.5                              |                            |                |         | -37.487 |          |
| 36                                | -37.558                    | -37.414        | -37.239 | -37.459 |          |
| 36.5                              |                            |                |         | -37.422 |          |
| 37                                | -37.536                    | -37.354        | -37.116 | -37.380 |          |
| 38                                | -37.485                    | -37.278        | -36.968 | -37.276 |          |
| 39                                | -37.414                    | -37.188        |         | -37.160 |          |
| 40                                | -37.366                    | -37.090        |         |         |          |
| 41                                | -37.405                    |                |         |         |          |
| 42                                | -37.407                    |                |         |         |          |

Table C.4.: Calculated energies, HSE.

| Factors         | LDA           |                  |                    |              |
|-----------------|---------------|------------------|--------------------|--------------|
|                 | Mono $P2_1/c$ | Tetra $P4_2/nmc$ | Cubic $Fm\bar{3}m$ | Ortho $Pnma$ |
| E <sub>0</sub>  | -31.105       | -31.056          | -31.021            | -31.006      |
| V <sub>0</sub>  | 34.613        | 33.039           | 32.496             | 29.541       |
| B <sub>0</sub>  | 0.940         | 1.252            | 1.666              | 1.567        |
| B' <sub>0</sub> | 2.557         | 5.863            | 4.295              | 7.987        |
| MinVol/Å        | 34.878        | 33.039           | 32.496             | 29.541       |
| E(MinVol)/eV    | -31.113       | -31.056          | -31.021            | -31.006      |
| B0/GPa          | 150.640       | 200.650          | 266.890            | 251.080      |

Table C.5.: Parameters of the Birch-Murnaghan equations, LDA.

| Factors                      | PBE           |                  |                    |              |
|------------------------------|---------------|------------------|--------------------|--------------|
|                              | Mono $P2_1/c$ | Tetra $P4_2/nmc$ | Cubic $Fm\bar{3}m$ | Ortho $Pnma$ |
| $E_0$                        | -28.546       | -28.428          | -28.343            | -28.215      |
| $V_0$                        | 36.718        | 35.320           | 34.200             | 31.513       |
| $B_0$                        | 0.928         | 0.965            | 1.450              | 1.101        |
| $B'_0$                       | 2.468         | 5.828            | 4.230              | 8.062        |
| MinVol/Å                     | 36.767        | 35.316           | 33.868             | 31.513       |
| $E(\text{MinVol})/\text{eV}$ | -28.524       | -28.427          | -28.325            | -28.215      |
| $B0/\text{GPa}$              | 148.670       | 154.560          | 232.260            | 176.360      |

Table C.6.: Parameters of the Birch-Murnaghan equations, PBE.

| Factors                      | PBEsol        |                  |                    |              |
|------------------------------|---------------|------------------|--------------------|--------------|
|                              | Mono $P2_1/c$ | Tetra $P4_2/nmc$ | Cubic $Fm\bar{3}m$ | Ortho $Pnma$ |
| $E_0$                        | -30.703       | -30.623          | -30.561            | -30.519      |
| $V_0$                        | 35.467        | 33.962           | 33.152             | 30.380       |
| $B_0$                        | 1.008         | 1.129            | 1.559              | 1.432        |
| $B'_0$                       | 0.757         | 5.480            | 4.308              | 6.114        |
| MinVol/Å                     | 35.512        | 34.000           | 33.195             | 30.357       |
| $E(\text{MinVol})/\text{eV}$ | -30.704       | -30.625          | -30.560            | -30.525      |
| $B0/\text{GPa}$              | 161.531       | 180.952          | 249.803            | 229.365      |

Table C.7.: Parameters of the Birch-Murnaghan equations, PBEsol.

| Factors                      | HSE           |                  |                    |              |
|------------------------------|---------------|------------------|--------------------|--------------|
|                              | Mono $P2_1/c$ | Tetra $P4_2/nmc$ | Cubic $Fm\bar{3}m$ | Ortho $Pnma$ |
| $E_0$                        | -37.556       | -37.461          | -37.392            | -37.263      |
| $V_0$                        | 35.807        | 34.190           | 33.296             | 30.529       |
| $B_0$                        | 1.036         | 1.104            | 1.611              | 1.498        |
| $B'_0$                       | -0.498        | 6.044            | 4.291              | 9.839        |
| MinVol/Å                     | 35.900        | 34.190           | 33.296             | 30.597       |
| $E(\text{MinVol})/\text{eV}$ | -37.558       | -37.461          | -37.392            | -37.264      |
| $B0/\text{GPa}$              | 166.056       | 176.833          | 258.185            | 240.044      |

Table C.8.: Parameters of the Birch-Murnaghan equations, HSE.

|                        | LDA         |             |             |             |             |             |
|------------------------|-------------|-------------|-------------|-------------|-------------|-------------|
|                        | Zr LDA      |             | Zr PBE      |             | Pt LDA      |             |
|                        | Zr_sv       | O LDA       | Zr_sv       | O PBE       | Pt          | Pt PBE      |
| Name                   |             |             |             |             |             |             |
| Date                   | Feb 10 1998 | Jan 04 2005 | May 31 2000 | Apr 08 2002 | Apr 17 2000 | Jan 05 2001 |
| Max. Energy of PAW set | 357.078     | 400.000     | 461.257     | 400.000     | 230.228     | 230.283     |
| Valence configuration  | 4s4p5s4d    | s2p4        | 4s4p5s4d    | s2p4        | s1d9        | s1d9        |
| Augmentation Energy/eV | 357.078     | 605.392     | 461.257     | 605.392     | 358.966     | 358.966     |
| Core Radius/ $a_0$     | 2.500       | 1.520       | 2.500       | 1.520       | 2.500       | 2.500       |

Table C.9.: PAW potentials bundled with VASP used for all calculations.



## D. Bibliography

- [1] V. Maurice, M. Salmeron, and G.A. Somorjai. “The epitaxial growth of zirconium oxide thin films on Pt(111) single crystal surfaces”. In: *Surface Science* 237.1 - 3 (1990), pp. 116 –126. ISSN: 0039-6028. DOI: [10.1016/0039-6028\(90\)90524-C](https://doi.org/10.1016/0039-6028(90)90524-C).
- [2] Klaus Meinel, Karl-Michael Schindler, and Henning Neddermeyer. “Growth, structure and annealing behaviour of epitaxial ZrO<sub>2</sub> films on Pt(111)”. In: *Surface Science* 532 - 535 (2003), pp. 420 –424. ISSN: 0039-6028. DOI: [10.1016/S0039-6028\(03\)00187-0](https://doi.org/10.1016/S0039-6028(03)00187-0).
- [3] K Meinel et al. “STM, LEED, and DFT characterization of epitaxial ZrO<sub>2</sub> films on Pt(111)”. In: *Surface Science* 562.1-3 (2004), pp. 204 –218. ISSN: 0039-6028. DOI: [10.1016/j.susc.2004.06.035](https://doi.org/10.1016/j.susc.2004.06.035).
- [4] Moritz Antlanger et al. “Pt<sub>3</sub>Zr(0001): A substrate for growing well-ordered ultra-thin zirconia films by oxidation”. In: *Phys. Rev. B* 86 (3 July 2012), p. 035451. DOI: [10.1103/PhysRevB.86.035451](https://doi.org/10.1103/PhysRevB.86.035451).
- [5] Klaus Stierstadt. *Thermodynamik - Von der Mikrophysik zur Makrophysik*. Springer Berlin Heidelberg, 2010. ISBN: 978-3-642-05097-8. DOI: [10.1007/978-3-642-05098-5](https://doi.org/10.1007/978-3-642-05098-5).
- [6] J. M. Yeomans. *Statistical Mechanics of Phase Transitions*. Oxford Science Publications, 1992. ISBN: 0-19-851730-0.
- [7] F. D. Murnaghan. “Finite Deformations of an Elastic Solid”. English. In: *American Journal of Mathematics* 59.2 (1937), pp. 235–260. ISSN: 00029327.
- [8] F. Birch. “Finite Elastic Strain of Cubic Crystals”. In: *Physical Review* 71 (June 1947), pp. 809–824. DOI: [10.1103/PhysRev.71.809](https://doi.org/10.1103/PhysRev.71.809).
- [9] P. Hohenberg and W. Kohn. “Inhomogeneous Electron Gas”. In: *Phys. Rev.* 136 (3B Nov. 1964), B864–B871. DOI: [10.1103/PhysRev.136.B864](https://doi.org/10.1103/PhysRev.136.B864).
- [10] W. Kohn and L. J. Sham. “Self-Consistent Equations Including Exchange and Correlation Effects”. In: *Phys. Rev.* 140 (4A Nov. 1965), A1133–A1138. DOI: [10.1103/PhysRev.140.A1133](https://doi.org/10.1103/PhysRev.140.A1133).
- [11] Reiner M Dreizler and Eberhard Engel. *Density Functional Theory - An Advanced Course*. Springer Berlin Heidelberg, 2011. ISBN: 978-3-642-14089-1. DOI: [10.1007/978-3-642-14090-7](https://doi.org/10.1007/978-3-642-14090-7).
- [12] D. M. Ceperley and B. J. Alder. “Ground State of the Electron Gas by a Stochastic Method”. In: *Phys. Rev. Lett.* 45 (7 Aug. 1980), pp. 566–569. DOI: [10.1103/PhysRevLett.45.566](https://doi.org/10.1103/PhysRevLett.45.566).

- [13] John P. Perdew et al. “Atoms, molecules, solids, and surfaces: Applications of the generalized gradient approximation for exchange and correlation”. In: *Phys. Rev. B* 46 (11 Sept. 1992), pp. 6671–6687. DOI: [10.1103/PhysRevB.46.6671](https://doi.org/10.1103/PhysRevB.46.6671).
- [14] John P. Perdew, Kieron Burke, and Matthias Ernzerhof. “Generalized Gradient Approximation Made Simple”. In: *Phys. Rev. Lett.* 77 (18 Oct. 1996), pp. 3865–3868. DOI: [10.1103/PhysRevLett.77.3865](https://doi.org/10.1103/PhysRevLett.77.3865).
- [15] A. D. Becke. “Density-functional exchange-energy approximation with correct asymptotic behavior”. In: *Phys. Rev. A* 38 (6 Sept. 1988), pp. 3098–3100. DOI: [10.1103/PhysRevA.38.3098](https://doi.org/10.1103/PhysRevA.38.3098).
- [16] John P. Perdew. *Electronic Structure of Solids 1991*. Ed. by P. Ziesche and H. Eschrig. Akademie Verlag, Berlin, 1991, p. 11.
- [17] John P. Perdew et al. “Restoring the Density-Gradient Expansion for Exchange in Solids and Surfaces”. In: *Phys. Rev. Lett.* 100 (13 Apr. 2008), p. 136406. DOI: [10.1103/PhysRevLett.100.136406](https://doi.org/10.1103/PhysRevLett.100.136406).
- [18] J Heyd, GE Scuseria, and M Ernzerhof. “Hybrid functionals based on a screened Coulomb potential”. English. In: *J. Chem. Phys.* 118.18 (May 2003), 8207–8215. ISSN: 0021-9606. DOI: [10.1063/1.1564060](https://doi.org/10.1063/1.1564060).
- [19] M. Dion et al. “Van der Waals Density Functional for General Geometries”. In: *Phys. Rev. Lett.* 92 (24 June 2004), p. 246401. DOI: [10.1103/PhysRevLett.92.246401](https://doi.org/10.1103/PhysRevLett.92.246401).
- [20] Jiří Klimeš, David R Bowler, and Angelos Michaelides. “Chemical accuracy for the van der Waals density functional”. In: *Journal of Physics: Condensed Matter* 22 (2010), p. 022201. DOI: [10.1088/0953-8984/22/2/022201](https://doi.org/10.1088/0953-8984/22/2/022201).
- [21] Jiří Klimeš, David R. Bowler, and Angelos Michaelides. “Van der Waals density functionals applied to solids”. In: *Phys. Rev. B* 83 (19 May 2011), p. 195131. DOI: [10.1103/PhysRevB.83.195131](https://doi.org/10.1103/PhysRevB.83.195131).
- [22] G. Kresse and J. Furthmüller. “Efficiency of ab-initio total energy calculations for metals and semiconductors using a plane-wave basis set”. In: *Computational Materials Science* 6.1 (1996), pp. 15–50. ISSN: 0927-0256. DOI: [10.1016/0927-0256\(96\)00008-0](https://doi.org/10.1016/0927-0256(96)00008-0).
- [23] G. Kresse and J. Hafner. “*Ab initio* molecular dynamics for liquid metals”. In: *Phys. Rev. B* 47 (1 Jan. 1993), pp. 558–561. DOI: [10.1103/PhysRevB.47.558](https://doi.org/10.1103/PhysRevB.47.558).
- [24] G. Kresse and J. Hafner. “*Ab initio* molecular-dynamics simulation of the liquid-metal–amorphous-semiconductor transition in germanium”. In: *Phys. Rev. B* 49 (20 May 1994), pp. 14251–14269. DOI: [10.1103/PhysRevB.49.14251](https://doi.org/10.1103/PhysRevB.49.14251).
- [25] G. Kresse and J. Furthmüller. “Efficient iterative schemes for *ab initio* total-energy calculations using a plane-wave basis set”. In: *Phys. Rev. B* 54 (16 Oct. 1996), pp. 11169–11186. DOI: [10.1103/PhysRevB.54.11169](https://doi.org/10.1103/PhysRevB.54.11169).
- [26] P. E. Blöchl. “Projector augmented-wave method”. In: *Phys. Rev. B* 50 (24 Dec. 1994), pp. 17953–17979. DOI: [10.1103/PhysRevB.50.17953](https://doi.org/10.1103/PhysRevB.50.17953).

- [27] G. Kresse and D. Joubert. “From ultrasoft pseudopotentials to the projector augmented-wave method”. In: *Phys. Rev. B* 59 (3 Jan. 1999), pp. 1758–1775. DOI: [10.1103/PhysRevB.59.1758](https://doi.org/10.1103/PhysRevB.59.1758).
- [28] Hendrik J. Monkhorst and James D. Pack. “Special points for Brillouin-zone integrations”. In: *Phys. Rev. B* 13 (12 June 1976), pp. 5188–5192. DOI: [10.1103/PhysRevB.13.5188](https://doi.org/10.1103/PhysRevB.13.5188).
- [29] J. D. McCullough and K. N. Trueblood. “The crystal structure of baddeleyite (monoclinic  $\text{ZrO}_2$ )”. In: *Acta Crystallographica* 12.7 (July 1959), pp. 507–511. DOI: [10.1107/S0365110X59001530](https://doi.org/10.1107/S0365110X59001530).
- [30] R. W. G. Wyckoff. *Crystal Structures*. 2nd ed. Vol. 2. Wiley, New York, 1963.
- [31] G. Teufer. “The crystal structure of tetragonal  $\text{ZrO}_2$ ”. In: *Acta Crystallographica* 15.11 (Nov. 1962), p. 1187. DOI: [10.1107/S0365110X62003114](https://doi.org/10.1107/S0365110X62003114).
- [32] J. M. Leger et al. “Pressure-induced structural phase transitions in zirconia under high pressure”. In: *Phys. Rev. B* 47 (21 June 1993), pp. 14075–14083. DOI: [10.1103/PhysRevB.47.14075](https://doi.org/10.1103/PhysRevB.47.14075).
- [33] Yahya Al-Khatatbeh, Kanani K. M. Lee, and Boris Kiefer. “Phase relations and hardness trends of  $\text{ZrO}_2$  phases at high pressure”. In: *Phys. Rev. B* 81 (21 June 2010), p. 214102. DOI: [10.1103/PhysRevB.81.214102](https://doi.org/10.1103/PhysRevB.81.214102).
- [34] Y. Kudoh, H. Takeda, and H. Arashi. “In situ determination of crystal structure for high pressure phase of  $\text{ZrO}_2$  using a diamond anvil and single crystal X-ray diffraction method”. In: *Physics and Chemistry of Minerals* 13 (4 1986). 10.1007/BF00308274, pp. 233–237. ISSN: 0342-1791.
- [35] A. H. Heuer et al. “On the orthorhombic phase in  $\text{ZrO}_2$ -based alloys”. In: *Journal of Materials Science* 24 (1 1989). 10.1007/BF00660943, pp. 124–132. ISSN: 0022-2461.
- [36] Christopher J. Howard, Erich H. Kisi, and Osamu Ohtaka. “Crystal Structures of Two Orthorhombic Zirconias”. In: *Journal of the American Ceramic Society* 74.9 (1991), pp. 2321–2323. ISSN: 1551-2916. DOI: [10.1111/j.1151-2916.1991.tb08307.x](https://doi.org/10.1111/j.1151-2916.1991.tb08307.x).
- [37] Osamu Ohtaka et al. “Structural Analysis of Orthorhombic  $\text{ZrO}_2$  by High Resolution Neutron Powder Diffraction”. In: *Proceedings of the Japan Academy, Series B* 66.10 (1990), pp. 193–196. DOI: [10.2183/pjab.66.193](https://doi.org/10.2183/pjab.66.193).
- [38] Peter E. Blöchl, O. Jepsen, and O. K. Andersen. “Improved tetrahedron method for Brillouin-zone integrations”. In: *Phys. Rev. B* 49 (23 June 1994), pp. 16223–16233. DOI: [10.1103/PhysRevB.49.16223](https://doi.org/10.1103/PhysRevB.49.16223).
- [39] J. K. Dewhurst and J. E. Lowther. “Relative stability, structure, and elastic properties of several phases of pure zirconia”. In: *Phys. Rev. B* 57 (2 Jan. 1998), pp. 741–747. DOI: [10.1103/PhysRevB.57.741](https://doi.org/10.1103/PhysRevB.57.741).
- [40] A. Christensen and Emily A. Carter. “First-principles study of the surfaces of zirconia”. In: *Phys. Rev. B* 58 (12 Sept. 1998), pp. 8050–8064. DOI: [10.1103/PhysRevB.58.8050](https://doi.org/10.1103/PhysRevB.58.8050).

- [41] N. Troullier and José Luriaas Martins. “Efficient pseudopotentials for plane-wave calculations”. In: *Phys. Rev. B* 43 (3 Jan. 1991), pp. 1993–2006. DOI: [10.1103/PhysRevB.43.1993](#).
- [42] C. J. Howard, R. J. Hill, and B. E. Reichert. “Structures of  $\text{ZrO}_2$  polymorphs at room temperature by high-resolution neutron powder diffraction”. In: *Acta Crystallographica Section B* 44.2 (Apr. 1988), pp. 116–120. DOI: [10.1107/S0108768187010279](#).
- [43] Xinyuan Zhao and David Vanderbilt. “Phonons and lattice dielectric properties of zirconia”. In: *Phys. Rev. B* 65 (7 Jan. 2002), p. 075105. DOI: [10.1103/PhysRevB.65.075105](#).
- [44] John E. Jaffe, Rafał A. Bachorz, and Maciej Gutowski. “Low-temperature polymorphs of  $\text{ZrO}_2$  and  $\text{HfO}_2$ : A density-functional theory study”. In: *Phys. Rev. B* 72 (14 Oct. 2005), p. 144107. DOI: [10.1103/PhysRevB.72.144107](#).
- [45] R. Terki et al. “Structural and electronic properties of zirconia phases: A FP-LAPW investigations”. In: *Materials Science In Semiconductor Processing* 9.6 (Dec. 2006), pp. 1006–1013. DOI: [DOI10.1016/j.mssp.2006.10.033](#).
- [46] Julian Haines et al. “Characterization of the Cotunnite-Type Phases of Zirconia and Hafnia by Neutron Diffraction and Raman Spectroscopy”. In: *Journal of the American Ceramic Society* 80.7 (1997), pp. 1910–1914. ISSN: 1551-2916. DOI: [10.1111/j.1151-2916.1997.tb03073.x](#).
- [47] Julian Haines, Jean Michel Léger, and Abdeltif Atouf. “Crystal Structure and Equation of State of Cotunnite-Type Zirconia”. In: *Journal of the American Ceramic Society* 78.2 (1995), pp. 445–448. ISSN: 1551-2916. DOI: [10.1111/j.1151-2916.1995.tb08822.x](#).
- [48] Serge Desgreniers and Ken Lagarec. “High-density  $\text{ZrO}_2$  and  $\text{HfO}_2$  : Crystalline structures and equations of state”. In: *Phys. Rev. B* 59 (13 Apr. 1999), pp. 8467–8472. DOI: [10.1103/PhysRevB.59.8467](#).
- [49] Sai-Kit Chan et al. “Temperature Dependence of the Elastic Moduli of Monoclinic Zirconia”. In: *Journal of the American Ceramic Society* 74.7 (1991), pp. 1742–1744. ISSN: 1551-2916. DOI: [10.1111/j.1151-2916.1991.tb07177.x](#).
- [50] Erich H. Kisi and Christopher J. Howard. “Elastic Constants of Tetragonal Zirconia Measured by a New Powder Diffraction Technique”. In: *Journal of the American Ceramic Society* 81.6 (1998), pp. 1682–1684. ISSN: 1551-2916. DOI: [10.1111/j.1151-2916.1998.tb02533.x](#).
- [51] H. M. Kandil, J. D. Greiner, and J. F. Smith. “Single-Crystal Elastic Constants of Yttria-Stabilized Zirconia in the Range 20°C to 700°C”. In: *Journal of the American Ceramic Society* 67.5 (1984), pp. 341–346. ISSN: 1551-2916. DOI: [10.1111/j.1151-2916.1984.tb19534.x](#).
- [52] Osamu Ohtaka et al. “Phase relations and equation of state of  $\text{ZrO}_2$  to 100GPa”. In: *Journal of Applied Crystallography* 38.5 (Oct. 2005), pp. 727–733. DOI: [10.1107/S0021889805018145](#).

- [53] Peter Blaha and Karlheinz Schwarz. *WIEN2k*. Vienna University of Technology. 2002.
- [54] David W. McComb. “Bonding and electronic structure in zirconia pseudopolymorphs investigated by electron energy-loss spectroscopy”. In: *Phys. Rev. B* 54 (10 Sept. 1996), pp. 7094–7102. DOI: [10.1103/PhysRevB.54.7094](https://doi.org/10.1103/PhysRevB.54.7094).
- [55] R. H. French et al. “Experimental and theoretical determination of the electronic structure and optical properties of three phases of  $\text{ZrO}_2$ ”. In: *Phys. Rev. B* 49 (8 Feb. 1994), pp. 5133–5142. DOI: [10.1103/PhysRevB.49.5133](https://doi.org/10.1103/PhysRevB.49.5133).
- [56] E. Napetschnig, M. Schmid, and P. Varga. “Ultrathin alumina film on Cu-9at%-Al(111)”. In: *Surface Science* 602.10 (2008), pp. 1750–1756. ISSN: 0039-6028. DOI: [10.1016/j.susc.2008.02.040](https://doi.org/10.1016/j.susc.2008.02.040).
- [57] Georg Kresse et al. “Structure of the ultrathin aluminum oxide film on NiAl(110)”. In: *Science* 308.5727 (June 2005), pp. 1440–2. DOI: [10.1126/science.1107783](https://doi.org/10.1126/science.1107783).
- [58] J. Libuda et al. “Structure and defects of an ordered alumina film on NiAl(110)”. In: *Surface Science* 318.1-2 (1994), pp. 61–73. ISSN: 0039-6028. DOI: [10.1016/0039-6028\(94\)90341-7](https://doi.org/10.1016/0039-6028(94)90341-7).
- [59] M. Schmid et al. “Nanotemplate with Holes: Ultrathin Alumina on  $\text{Ni}_3\text{Al}(111)$ ”. In: *Phys. Rev. Lett.* 99 (19 Nov. 2007), p. 196104. DOI: [10.1103/PhysRevLett.99.196104](https://doi.org/10.1103/PhysRevLett.99.196104).
- [60] B. Predel. “Pt-Zr (Platinum-Zirconium)”. In: *Landolt-Börnstein - Group IV Physical Chemistry*. Ed. by O. Madelung. Vol. 5I. SpringerMaterials - The Landolt-Börnstein Database (<http://www.springermaterials.com>).
- [61] J. R. McBride et al. “Growth and characterization of reactively sputtered thin-film platinum oxides”. In: *Journal of Applied Physics* 69.3 (1991), pp. 1596–1604. DOI: [10.1063/1.347255](https://doi.org/10.1063/1.347255).
- [62] Jacek Goniakowski and Claudine Noguera. “Polarization and rumpling in oxide monolayers deposited on metallic substrates”. In: *Phys. Rev. B* 79 (15 Apr. 2009), p. 155433. DOI: [10.1103/PhysRevB.79.155433](https://doi.org/10.1103/PhysRevB.79.155433).
- [63] Georg Kresse, Martijn Marsman, and Jürgen Furthmüller. *VASP the GUIDE*.
- [64] M. Methfessel and A. T. Paxton. “High-precision sampling for Brillouin-zone integration in metals”. In: *Phys. Rev. B* 40 (6 Aug. 1989), pp. 3616–3621. DOI: [10.1103/PhysRevB.40.3616](https://doi.org/10.1103/PhysRevB.40.3616).
- [65] William H. Press et al. *Numerical Recipes 3rd Edition*. Cambridge University Press, 2007. ISBN: 9780521880688.
- [66] P. Pulay. “Convergence acceleration of iterative sequences. the case of scf iteration”. In: *Chemical Physics Letters* 73.2 (1980), pp. 393–398. ISSN: 0009-2614. DOI: [10.1016/0009-2614\(80\)80396-4](https://doi.org/10.1016/0009-2614(80)80396-4).